NORTHWESTERN UNIVERSITY

Structure-Property Relationships in Amorphous Transparent Conducting Oxides

A DISSERTATION

SUBMITTED TO THE GRADUATE SCHOOL
IN PARTIAL FULFILLMENT OF THE REQUIREMENTS

for the degree

DOCTOR OF PHILOSOPHY

Field of Materials Science and Engineering

By

Stephanie Lucille Moffitt

EVANSTON, ILLINOIS

September 2017

© Copyright by Stephanie Lucille Moffitt 2017
All Rights Reserved

ABSTRACT

Structure-Property Relationships in Amorphous Transparent Conducting Oxides

Stephanie Lucille Moffitt

Over the last 20 years a new field of amorphous transparent conducting oxides (a-TCOs) has developed.[1] The amorphous nature of these films makes them well suited for large area applications.[2-3] In addition, a-TCOs can be made at low temperatures and through solution processing methods.[4-6] These assets provide promising opportunities to improve applications such as solar cells and backlit displays where traditional crystalline TCOs are used. In addition, it opens the door for new technological applications including the possibility for transparent, flexible electronics.[4] Despite the recent growth in this field, fundamental understanding of the true nature of conductivity and the amorphous structure in this materials system is still progressing.

To develop a greater understanding of a-TCOs, structure-property relationships were developed in the a-IGO and a-IZO systems. From the combination of element-specific local structure studies and liquid quench molecular dynamics simulations it is clear that a degree of structure remains in a-TCOs. By understanding this structure, the effect of gallium on thermal

stability, carrier concentration and carrier mobility is understood. The source of charge carriers in a-IZO is identified as oxygen vacancies through the application of *in situ* Brouwer analysis. The continued development of the Brouwer analysis technique for use in amorphous oxides adds to the available methods for studying defects in amorphous systems. Finally, the foundational knowledge gained from the in-depth study of a-IGO was extended to understand the role of combustion processing and pulsed laser deposition as growth methods for transistors based on a-IGO.

Acknowledgements

Northwestern has been a wonderful place to conduct my PhD. I have many people to thank for making this journey such a wonderful experience. I'd like to thank Prof. Thomas Mason, whose passion for teaching helped bring me to Northwestern. The Mason group helped build my foundation as an independent researcher and a strong science communicator. Thank you to Prof. Michael Bedzyk and Prof. Tobin Marks, who welcomed me into their groups and allowed me to continue my journey. I have learned so much from both of them. Mike's door is always open and Tobin's enthusiasm for science and technology is truly contagious. I want to thank my committee members Prof. Julia Medvedeva and Prof. Robert P. H. Chang, your insight and support has been invaluable. I would also like to acknowledge my undergraduate adviser Prof. Ram Seshadri who first introduced me to research and has continued to provide mentorship throughout my PhD.

I want to recognize the National Science Foundation who has supported my work through the Graduate Research Fellowship Program and the Materials Research in Science and Engineering center (Program No. DMR 1121262). The flexibility and generosity of both programs have been invaluable in the success of my PhD.

I am grateful to all the members of the Mason, Bedzyk, and Marks groups. I have been lucky to have such friendly and supportive groups throughout my PhD. In particular, I would like to thank Alexander Adler, whose mentorship helped me make a strong start at Northwestern. I want to acknowledge the members of the MRSEC IRG2, whose brownbag lunches provided powerful insight and greatly improved my own work. Having IRG2 as a group throughout my PhD journey has been a great support. Thank you to Allison my undergraduate student, you have been a joy to work with. I also want to recognize my many collaborators especially Dr. Qing Ma, Jerry Carsello, and Dr. Bruce Buchholz. Your expertise has been instrumental in my work.

Outside of my research I have enjoyed a large and beautiful support network. I want to thank all my friends who have supported me and inspired me throughout my PhD including: my first-year study buddies, Lindsay, Madeleine, Erika, Ashwin, and Justin and my friends at lunchtime and beyond, Arpun, Patrick, Alex, Karen, Sam, Shawn, Gavin and Ha-Kyung. The wonderfully connected and supportive department gave me the opportunity to learn from students outside my year like Emily, Lauren, Hypo, and Ricardo. I am grateful for my roommate Jamie. Your friendship has helped make our apartment a home. A big thank you to my family. I am so fortunate to have such a supportive family. I am very thankful for my mom Jeanette and my dad John. They have set me up to succeed; they taught me to believe in myself and have

always supported me. Finally, I am grateful for Josh whose support and friendship has made life at Northwestern a more joyful adventure.

List of abbreviations

a-	Amorphous
A-GIWAXS	Anomalous grazing incidence wide-angle X-ray scattering
DFT	Density functional theory
d-PDF	Difference-pair distribution function
EXAFS	Extended X-ray absorption fine structure
GI	Grazing incidence geometry
IO	Indium-oxide
IGO	Indium-gallium-oxide
IGZO	Indium-gallium-zinc-oxide
IZO	Indium-zinc-oxide
MD	Molecular dynamics
M-O	Metal-oxygen
PLD	Pulsed laser deposition
PVD	Physical vapor deposition
SAXS	Small-angle X-ray scattering
Spin-CS	Spin coating combustion synthesis
Spray-CS	Spray coating combustion synthesis
STP	Standard temperature and pressure
TFT	Thin film transistor
XANES	X-ray absorption near edge spectroscopy
XAS	X-ray absorption spectroscopy

XPS	X-ray photoelectron spectroscopy
XRD	X-ray diffraction
XRF	X-ray fluorescence
XRR	X-ray reflectivity

TABLE OF CONTENTS

ABSTRACT 3

Acknowledgements 5

List of abbreviations 8

List of figures 15

List of tables 27

CHAPTER 1: **Introduction** 28

1.1 Motivation 28

1.2 Outline 29

CHAPTER 2: **Background** 31

2.1 Local Structure Studies 31

2.2 Defects and Charge Carriers 32

2.3 Thermal Stability of Amorphous Oxides 36

CHAPTER 3: **Synthesis and Characterization Techniques** 38

3.1 Film Growth 38

3.1.1 Physical vapor deposition 38

3.1.2 Solution processing 41

3.2 Structural Characterization and X-ray Techniques 42

3.2.1 Ellipsometry 42

3.2.2 X-ray characterization techniques 43

3.2.3 Grazing incidence geometry 45

3.2.4 X-ray diffraction 46

3.2.5 X-ray absorption spectroscopy 48

3.2.6 X-ray fluorescence 54

3.2.7 X-ray reflectivity 55

3.3 Electrical Characterization 57

3.3.1 Hall probe 57

CHAPTER 4: **The Role of Ga in the Local Structure and Thermal Stability of a-IGO** 59

4.1 Introduction 60

4.2 Methods 62

4.2.1 Film growth 62

4.2.2 Crystallization study 64

4.2.3 Short and medium-range structural characterization 65

4.3.4 Data reduction 68

4.3 Results and Discussion 71

4.3.1 Experimental structure 73

4.3.2 MD-simulated structure 79

4.4 Conclusion 88

CHAPTER 5: **The Role of Ga in the Electrical Properties of a-IGO** 89

5.1 Introduction 90

5.2 Methods 92

5.3 Results and Discussion 93

5.3.1 Carrier generation: experimental 95

5.3.2 Carrier generation: MD simulations and DFT calculations 97

5.3.3 Carrier mobility experimental 102

5.3.4 Carrier mobility: DFT computation 104

5.4 Conclusion 107

CHAPTER 6: **Confirmation of the Dominant Point Defect Mechanism in a-IZO through the Application of *In Situ* Brouwer Analysis** 109

6.1 Introduction 110

6.2 Experimental Procedure 113

6.2.1 Deposition 113

6.2.2 *In situ* electrical characterization 114

6.3 Results and Discussion 119

6.3.1 Regime 3: background decay 119

6.3.2 Regime 1: surface response 122

6.3.3 Regime 2: bulk defect modulation 122

6.4 Conclusion 125

CHAPTER 7: **A Fundamental Comparison of Combustion Synthesis and Pulsed Laser Deposition: Film Growth Processes in the a-IGO System** 127

7.1 Introduction 128

7.2 Results and Discussion 133

7.2.1 Transistor characterization 133

7.2.1 Thermal stability 143

7.3 Conclusion 148

7.4 Methods 149

7.4.1 Film and TFT synthesis 149

7.4.2 Pulsed laser deposition (PLD) 149

7.4.3 Combustion synthesis 150

7.4.4 Spray combustion synthesis (Spray-CS)... 151

7.4.5 Spin combustion synthesis (Spin-CS)... 151

7.4.6 Transistor fabrication and testing.. 152

7.4.7 Film composition 152

7.4.8 Crystallization study 153

7.4.9 Structural characterization 154

7.4.10 X-ray absorption spectroscopy (XAS).. 154

CHAPTER 8: **Conclusions and Future Work** 156

8.1 Future Work: Amorphous Oxides for Wearable Thermoelectrics............................... 158

APPENDIX.. 165

Appendix A: Thin Film X-ray Fluorescence Manual.. 165

A.1 Introduction.. 165

A.2 Data Acquisition 166

A.3 XRF Peak Fitting 168

List of figures

Figure 2.1 Comparison of carrier concentration (n) as a function of substitution fraction (at%) of secondary cations in the amorphous indium oxide and amorphous tin oxide systems. Measurements and film synthesis performed by Dr. D. Bruce Buchholz……………………….34

Figure 2.2 Comparison of crystallization temperature as a function of substitution fraction (at%) of secondary and tertiary cations in the amorphous indium oxide and amorphous tin oxide systems. [14, 34, 37-39]……………………………………………………………………………...36

Figure 3.1 In DC magnetron sputtering a conductive target A) acts as a cathode and is connected to the negative terminal of a DC power supply B). Opposite the target is the substrate C) on top of the anode D). The chamber is evacuated with a vacuum E) and back filled with the working gas, typically argon F). Once a glow discharge is maintained, current flows between the cathode and the anode. Positive gas ions in the discharge strike the cathode and eject atoms (green arrows) that deposits onto the substrate. Magnetic field lines (orange arcs) are created over the target to stabilize the discharge...……………………………………………………………………..………...38

Figure 3.2 Pulsed laser deposition features a 248nm KrF eximer-laser A) which ablates a ceramic target B). Doped samples are created by rotating C) to choose from different targets F). Each ceramic target is additionally rotated to ensure efficient ablation of the target. A plasma

plume of material D) is created by the laser and deposits onto the substrate E). The deposition temperature can be modified by heating or cooling the substrate holder. Figure adapted from Alex U. Adler's thesis……………………………………………………………….………...41

Figure 3.3 Combustion solution processing begins with an aqueous solution of dissolved metal nitrates and acetylacetone. This solution is spin coated onto a substrate and then placed directly onto a hot plate. The metal nitrate solution can also be sprayed through an ultrasonic nozzle directly onto a substrate sitting on a hot plate…………………………………………………...43

Figure 3.4 A) For X-rays, the index of refraction (n) for materials is less than 1. This results in the refracted angle (α') of X-rays being smaller than the incident angle (α). B) When the incident X-ray angle (α) is less than the critical angle (α_c), total external reflection occurs. At this condition, an evanescent wave penetrates into the material with a rapidly diminishing intensity characterized by an effective attenuation length of 1 to 10 nm. Figures adapted from Elements of Modern X-ray Physics. ……………………………………………..………………………...44

Figure 3.5 Above the critical angle (α_c), X-ray penetration depth rises quickly and approaches $\sin\alpha/\mu$. A suitable grazing angle can be determined based on the thickness of the film………...46

Figure 3.6 A) In GIXRD geometry the incident X-ray angle (α) is held just above the critical angle to limit the penetration depth in the material. The point detector is scanned through a range

of 2θ angles to collect X-ray diffraction from the crystalline portion of the sample. B) In a partially crystalline film the X-ray diffraction pattern is a superposition of the broad scattering hump originating from the amorphous portion of the sample and the strong diffraction peaks originating from the crystalline portion of the sample. …………………..……………………...47

Figure 3.7 A) Each element has a unique absorption edge that depends on the energy of its core-level electrons, if an atom is ionized the edge position will shift. B) At the K-edge energy, X-ray absorption increases because a core-level photoelectron is ejected. The ability of light to eject electrons is known as the photoelectric effect. C) In a bare atom, or monatomic gas, the photoelectron leaves the atom and decays. It has no effect on the absorption spectrum. D) When the excited atom has a neighboring atom, the photoelectron has a probability of scattering back and causing interference in the absorption. E) EXAFS data are converted from energy space to inverse space (k-space) before fitting is performed. F) Fourier transforms of k-space EXAFS data reveal pseudo-radial distribution functions that are useful for visualizing data…………………49

Figure 3.8 Normalized absorption as a function of incident photon energy is shown in dark blue. The absorption of a bare atom is shown in red. XAS is typically broken up in to two techniques. Analysis of data near the absorption edge reveals the “X-ray absorption near-edge structure”

(XANES) and the data farther out in energy reveals the "extended X-ray absorption fine-structure" EXAFS. ……………………………………………..………………………...51

Figure 3.9 Once a photoelectron is ejected by an incident X-ray (blue) from the core (K) level or outer levels (L), an electron from a higher level (L or M) drops down and the atom is relaxed. A fluorescence X-ray (green) is released upon this relaxation event. The energy of the ejected photon depends on the energy difference between the two levels………………………………54

Figure 3.10 XRR measurements can provide the thickness, density, and roughness of thin films through the analysis of Kiessig fringes. ……………………………………………..………..57

Figure 3.11 Hall-probe set up: Films are contacted in van der Pauw configuration by four gold probes. Current is applied diagonally (i.e. from contact 2 to 3) and the resulting voltage is measured perpendicular (i.e. from contact 1 to 4). IV curves are run before each measurement to ensure ohmic behavior. ……………………………………………..………………………...58

Figure 4.1 GIXRD data at 8.04 keV of a representative a-IGO thin film (8 at% Ga) as deposited (green, middle) and after air annealing has caused crystallization (red, top). For reference, the cubic $Ia\bar{3}$ In_2O_3 bixbyite powder[1] XRD pattern is shown in black (bottom). The small shift in the peak position is due to the lattice contraction induced by Ga substitution………………………62

Figure 4.2 A) Crystallization temperature as a function of at% Ga substitution determined through 1 hour anneal/quench/GIXRD cycles spaced 25°C apart. Error bars represent the 25°C window of uncertainty between pre- and post- crystallization runs. B) GIXRD determined lattice constant of the bixbyite unit cell for fully crystallized IGO samples as a function of Ga substitution. The solid line is a linear least-squares fit to the four data points. Error bars are smaller than the data points..72

Figure 4.3 A) PDF of a-IGO with 17 at% Ga (red). Difference PDF of the structure around Ga in a-IGO17 (green). Calculated PDF for β-Ga_2O_3 is shown for reference (black dotted line). B) Measured pair distribution function (PDF) for a-IGO with 8 at% Ga (blue) and 17 at% Ga (red). Calculated PDF for bixbyite In_2O_3 is shown for reference (black dotted). The first and second peaks are produced by M-O and M··M distances, respectively. The first peak is weaker because O is a weak scatterer...73

Figure 4.4 A) β-gallia Ga_2O_3 crystal structure.[10] Ga atoms are green and O atoms are red. B) Bixbyite In_2O_3 crystal structure.[1] In atoms are purple and O atoms are red. Figures were drawn with the Vesta software package. 75

Figure 4.5 Distribution of calculated ECN values in a-IO and three a-IGO compositions as obtained from room termperature MD simulations for In-O, A) and Ga-O, B). Spread of

polyhedra edge-shared (solid line), corner-shared (dotted line), and lack of sharing (dashed line), C) M··M distances and D) Ga··M distances shown for I) a-IGO11 (orange), II) a-IGO19 (blue), and III) a-IGO41 (green). Black lines show the sharing distributions for a-IO in C) and for β-Ga_2O_3 in D). ……………………………………………………………………………81

Figure 4.6 Distribution of calculated ECN in a-IGO41 with variable oxygen content as obtained at room temperature MD simulations for A) In-O and B) Ga-O………………………………85

Figure 5.1 A) Hall effect data for a series of a-IGO thin films as a function of at% Ga. Error bars represent the standard deviation between three samples of the same composition, grown under the same conditions. The error bars are the size of the data points for conductivity and mobility. Dashed lines represent exponential fits of the data and are provided as visual guides for the observed trends. B) Room temperature Hall effect data on IGO51 (blue), as a function of annealing temperature. As-deposited results are plotted at -25°C. The sample was cycled through air annealing (at increasing temperatures), quench, and room temperature Hall measurements. Error bars are calculated as the standard deviation of 10 consecutive measurements and are smaller than the data points in most cases………………………………94

Figure 5.2 A) The In K-edge XANES data for the crystalline (c-) In_2O_3 reference (bixbyite), amorphous (a-) IO, and the three a-IGO films. B) The Ga K-edge spectra for the c-Ga_2O_3 (beta gallia) reference and the 3 a-IGO samples. ..…………………………..……………………...96

Figure 5.3 A,B,C,D) Calculated charge density distribution in the conduction band of a-IGO. Independent of Ga presence or content, the shallow defect state is associated with the charge accumulation between under-shared, low-coordinated, In-In pairs in: A) a-IO, B) IGO11, C) IGO19, D) IGO41. In all cases, the charge avoids octahedrally-coordinated In-O polyhedra (purple) as well as Ga-O polyhedra (green). For the under-shared, low-coordinated In atoms (no polyhedra), the In-O bonds are shown (red-purple). E,F,G,H) 2D simplification of the structures for E) a-IO, F) IGO11, G) IGO19, H) IGO41. In-O octahedral, represented as purple squares, form chains (I), which organize under-coordinated In-O polyhedra, represented as purple circles. This organization produces the yellow conduction manifold of high electron density. The conduction manifold begins to break up in the presence of Ga-O tetrahedra (II), represented as green triangles. Traps (III) form when Ga-O tetrahedra surround low-coordinated In atoms. At high Ga content, chains of Ga-O tetrahedra begin to form (IV), negating Ga's disruptive effect on the conduction manifold. ..…………………………………………..…………………99

Figure 5.4 The calculated inverse participation ratio for a-IO and a-IGO. The valence band tail states are more localized in IGO than in IO owing to the presence of under-coordinated oxygen atoms. The conduction states below the Fermi level (at 0eV) are delocalized suggesting the formation of a shallow defect even at high Ga content. Localization of the empty conduction states above the Fermi level associated with non-uniform charge distribution, explain the observed mobility drop in a-IGO as compared to a-IO. Above the Fermi level, the charge density is localized at low-coordinate In atom surrounded by fully-coordinate Ga atoms as in B) a-IGO19. ..…………………………………………...…………..…………………..101

Figure 5.5 Plot of the Hall mobility of a-IGO films versus the corresponding carrier concentration. Mobility increases with increasing carrier content. If ionized impurity scattering were limiting mobility, the mobility should drop in response to rising carrier concentration. The dashed line serves as a guide for the eye……………………………………………………..…103

Figure 6.1 Experimental set up used to measure in situ conductivity as a function of O_2 partial pressure. A) Gas tanks of pre-mixed O_2/Ar, B) 4-way switch, C) Desiccator, D) Furnace held at 300°C, E) Sealed quartz tube, F) Van der Pauw contacts, G) pO_2 meter………………………115

Figure 6.2 Conductivity transients of a-IZO as a function of time in response to varying oxygen environments. Dashed lines represent temporary interruptions in data acquisition……………116

Figure 6.3 Conductivity response of a-IZO thin film at 200°C during an oxidative transient measured in situ as a function of time. $PO_{2initial}$: 1000 ppm PO_{2final}: 1.0%................................117

Figure 6.4 In situ DOS-mobility product (ln(σ)-Q_{red}) for a-IZO films at 300°C as a function of time illustrating that mobility remains constant in response to changes in O_2 environment over the experimental campaign. The last 10 hours of exposure to each pO_2 are represented as black dots and error bars are represented as grey lines. Disruptions in the dashed line represent temporary interruptions in data acquisition, as seen in the conductivity results (Fig. 6.2)…….118

Figure 6.5 Conductivity response of a-IZO thin film during a) oxidation and b) reduction measured in situ as a function of time. From left-to-right: regime 1 (blue), regime 2 (white), and regime 3 (red) correspond to the dominant mechanism during the indicated time periods (surface response, bulk defect modulation, and background structural relaxation)……………………..120

Figure 6.6 GIXRD scans of the a-IZO thin film before (top) and after (middle) the experimental campaign, in comparison with the glass substrate (bottom). The major peaks of crystalline InZnO are indicated by the vertical dashes above the x-axis.[7] GIXRD scans were performed with a Rigaku Smartlab diffractometer. ..…………………………………………..……………..121

Figure 6.7 β values (which correspond to the slope in a Brouwer plot) as a function of equilibrium O_2 partial pressure (pO_2). ..…………………………………………………..………125

Figure 7.1 A schematic demonstrating the A) PLD deposition method, B) Spray-CS method, and C) Spin-CS method. All three methods were used in creating the channel layer of transistors with the architecture shown in D). ..………………………………………..……………..130

Figure 7.2 X-ray characterization data for IGO TFT films grown by PLD (red), Spin-CS (green), and Spray-CS (blue). A) GIXRD patterns of as-deposited IGO films before the deposition of Al contacts. Note, that at low Ga content, Spray-CS films are partially crystalline and display peaks at Q values of ~2.2 and 2.5. The 400 peak from the Si substrate can be seen at Q ~3.6. B) XRR plots of as-deposited IGO films. Fits are shown as black lines. C) Electron density of each TFT channel layer. Films with multiple layers are presented as the average density of all layers. D) Scattering length density (SLD) as a function of distance from the surface of the film………..135

Figure 7.3 Saturation mobility A) and on voltage B) of TFT devices made with a-IGO channel layers deposited by PLD (red squares), Spin-CS (green circles), and Spray-CS (blue triangles). Each point represents a separate film deposition. Greater than 10 devices were measured on each film; error bars represent the standard deviation between devices. Dashed lines represent linear best fits of PLD (red) and Spin-CS (green) data and are provided to highlight Ga-dependent trends. Purple triangle represents partially crystalline Spray IGO26 film……………………...137

Figure 7.4 Coordination number comparisons from In K-edge and Ga K-edge EXAFS data for PLD films grown at 7.5 mTorr, Spray-CS films grown at 250°, and Spin-CS films. A) Comparison of M-O coordination. B) Comparison of M-O bond length……………………139

Figure 7.5 Comparison of forward-to-reverse voltage sweep hysteresis observed after 10 voltage sweeps of devices with a-IGO channel layer deposited via A) PLD, B) Spin-CS, and C) Spray-CS...……………………………………………..……………..…………...………140

Figure 7.6 PLD output plots for A) 9.3 at% Ga, B) 18.0 at% Ga, C) 28.0 at% Ga, and D) 35.0 at% Ga....……………………………………………..……………..……………………..142

Figure 7.7 A) GIXRD patterns are taken continuously during air annealing. Films are heated inside a graphite dome at a rate of 2 °C per minute. 2θ scans each lasted 5.5 minutes. B) Percent crystalline fraction of Spin-CS IGO17 sample is plotted as a function of median scan temperature. ...…………………………… ……………..……………..…………………144

Figure 7.8 A) Crystallization temperature and B) temperature at the onset of crystallization, of spin combustion (green), spray combustion (blue), and PLD (red) a-IGO films as a function of at% Ga. Data points indicated by × in figure A represent those which required extrapolation due to sample deterioration or instrumental temperature limitations……………………………….145

Figure 7.9 Scattering length density showing the increase in density and decrease in thickness from before crystallization (dark line) to after crystallization (bright line) for a representative Spin-CS (green, A), Spray-CS (blue, B), and PLD (red, C) film………………………………146

Figure A.1 Diagram of XSW instrument showing the positions of the slit motors (S1, S2, S3, S4), θ/α motor (th), 2θ motor (tth), and z motor (xsamp). The X-ray path is indicated by the grey dashed line…………………………………………………...………………………………165

Figure A.2 Calculation of X-ray transmission through a 25 μm Be window (T_{Be}) as a function of X-ray energy. Calculation performed by CXRO website………………………………………172

List of tables

Table 4.1 First shell (metal-oxygen) EXAFS fitting results of experimental samples compared with room temperature MD simulations……………………………………………………………76

Table 4.2 Comparison of first-shell (metal-oxygen) EXAFS fitting results of as-deposited (amorphous) versus annealed (crystallized) films, showing changes in coordination numbers and bond lengths. ………………………….…………………………………………………………78

Table 4.3 A-IGO second shell EXAFS fitting results of In K-edge (metal-metal)……………...83

Table 7.1 Performance metrics from TFT devices made with 10-15 nm a-IGO channel layer films deposited on SiO_2/Si with Al contacts fabricated via PLD, Spin-CS, and Spray-CS……134

Table A.1 Basics of SPEC for Mo 18-kW rotating anode 2-circle (XSW) instrument…..……166

Table A.2 Parameter settings for using the setxswdxp SPEC macro to perform XRF..….……168

Table A.3 Sugomat Matlab-script commands …………………………………………………169

CHAPTER 1: **Introduction**

1.1 Motivation

Transparent amorphous (a-) oxides, for example SiO_2, are historically classified as electronically insulating. However, recent advances in the field of transparent conducting oxides (TCOs) have shown that heavy post-transition metal oxides (In-O, In-Zn-O system, In-Ga-Zn-O system etc.) can maintain high carrier content (>10^{20} cm^{-3}) and more impressively high mobility (>60cm^2/Vs in In-O) in the amorphous state.[8-10] This new class of *amorphous*, transparent conducting oxide materials (a-TCOs) holds promise for a wide range of technological applications. Amorphous materials have an advantage over polycrystalline TCOs because they can be deposited at low temperatures to create highly uniform, smooth films that lack grain boundaries. These qualities make them ideal for large area applications such as flat panel displays, solar cells, and smart windows.[11] In addition, their characteristic low deposition temperatures (even room temperature) present the possibility for low cost deposition on lightweight delicate substrates, like plastic, opening the door for fully transparent, flexible electronics.[10]

Some amorphous oxides have already seen commercial success, most notably a-IGZO (amorphous indium gallium zinc oxide), which is replacing amorphous silicon as the channel layer in the thin film transistors of mobile displays.[12] Despite obtaining commercial success,

issues of stability persist. In order to fine-tune processing and inform the next generation of materials, amorphous conducting oxides must be fully understood on a fundamental level. Many of the benefits these materials gain from their amorphous state also present significant challenges to fundamental studies. The pursuit of fundamental understanding has proven to be challenging. The characterization and modeling tools used to understand crystalline TCOs often cannot be used or must undergo significant modifications before being applied to a-oxides. This work seeks to expand the field of amorphous oxides by furthering the development of tools and methodologies used for characterizing amorphous oxides in the uniting goal of understanding the structure property relationships in these materials. A strong fundamental knowledge of structure-property relationships in amorphous oxides will inform their optimization and expand the range of potential application

1.2 Outline

This dissertation is organized into 8 chapters. Background information on the current literature exploring defects in a-TCOs and the structure and thermal stability of TCOs is provided in **chapter 2. Chapter 3** provides an introduction to the synthesis and film characterization techniques employed in this work. **Chapters 4 and 5** both explore the structure-property

relationships in a-IGO. Chapter 4 looks at the effect of Ga on the thermal stability of a-IGO while chapter 5 investigates the role of Ga in the thermal properties of a-IGO. The dominant point-defect mechanism and the source of charge carriers in a-IZO is identified in **chapter 6**. Chapter 6 also discusses the application of Brouwer analysis to amorphous oxide films. **Chapter 7** expands the work of chapters 4 and 5 to explore the effect of processing method on the structure, properties and TFT performance of a-IGO films. Both combustion synthesis (a solution processing method) and pulsed laser deposition are studied in this chapter. **Chapter 8** concludes the dissertation and provides recommendations for future work.

CHAPTER 2: **Background**

2.1 Local Structure Studies

The study of oxide materials draws great strength from the understanding of structure property relationships. Knowledge of lattice parameters, space group, symmetry, and atomic coordination, have informed the understanding and exploration of almost all classes of oxide materials. In amorphous materials which lack crystalline order, and thus produce no diffraction pattern, knowledge of atomic positions is much harder to obtain and consequently even harder to model and predict. However, despite the absence of long-range order, amorphous oxides are not completely without structure. Both experimental methods and computational modeling have been successful in probing the local structure that persists in these materials.[13-16] X-ray absorption spectroscopy (XAS) has been the most widely successfully experimental technique.[14-16]

Thus far, most local structure studies have been done on materials which have seen commercial success, a-IGZO and a-ZITO (Zn and Sn doped In_2O_3).[14, 16] However, in these multiple-cation oxides the contributions from each are difficult to elucidate. More recently, in depth studies by the Chang group have looked at the un-doped parent oxide, a-indium oxide (a-IO), to gain greater clarity with respect to the role of deposition temperature on the local

structure.[15] This study also demonstrated the power of using molecular dynamics simulations in tandem with experimental local structure studies to further expand structure property relationships. Probing the effect of dopants in binary cation systems is the next logically step in moving towards a complete picture of structure-property relationships in amorphous oxides. Gallium is often cited as being crucial to stabilizing carrier concentrations of a-TCOs at semiconducting levels. Yet gallium is most often studied only as a member of the tertiary cation compound a-IGZO, where the roles it plays in local structure is convoluted by the presence of zinc. In this work, we pair in-depth XAS with liquid quench molecular dynamics (MD) simulations to provide greater strength to the understanding of the second and third shell structure in a-IGO. In addition, element specific anomalous X-ray scattering measurements are performed by to produce element sensitive pair distributions functions that confirm XAS and MD simulation results and experimentally probe the structure of amorphous oxides out to 12Å.

2.2 Defects and Charge Carriers

The study of defects plays an important role in understanding the properties of many materials systems; transparent conducting oxides are no exception. Defects are inherently tied to the intrinsic production of charge carriers.[17] An understanding of the relationship between defects

and carrier production is important for controlling many TCO properties including conductivity, photoconductivity, carrier mobility, and optical transparency.[18-19] Control of carriers is also critical in applying AOS as the channel layer in thin film transistors. Efficient TFTs depend on the ability to easily and reliably turn the flow of charge on and off. Thus, controllable carrier concentration is inherently tied to the production of efficient and reliable TFTs.

Without the established order of a crystalline lattice, identification of defects in amorphous oxides appears insurmountable. However, many amorphous oxides, e.g. a-In-O, demonstrate intrinsic, controllable carrier concentration.[10, 18, 20-21] Therefore, defects must exist in these materials. Though quantification of the subtle structural and compositional difference between amorphous oxide films is challenging, differences in the performance of these materials confirm that all amorphous structures are not equivalently disordered.[10] First-principles calculations by Kamiya et al.[22] highlight the importance of local structure in carrier production; an oxygen "vacancy" was demonstrated as either a trap or a carrier producing defect dependent upon the local structure. Control of carrier concentration in amorphous oxides through traditional doping mechanisms also proves to be a challenge (Fig. 2.1). For instance, when Zn^{2+} is substituted for In^{3+} in a-In-Zn-O, the material remains an n-type semiconductor and sees minimal ($>>$ 1 order of magnitude) changes in the carrier concentration.[9, 23-24] A similar lack of response of amorphous

oxides to traditional extrinsic doping is seen in a-ITO. No change in the carrier concentration follows the Sn concentration in the amorphous films. It is only once the films crystallize that carrier concentration depends on Sn concentration.[25]

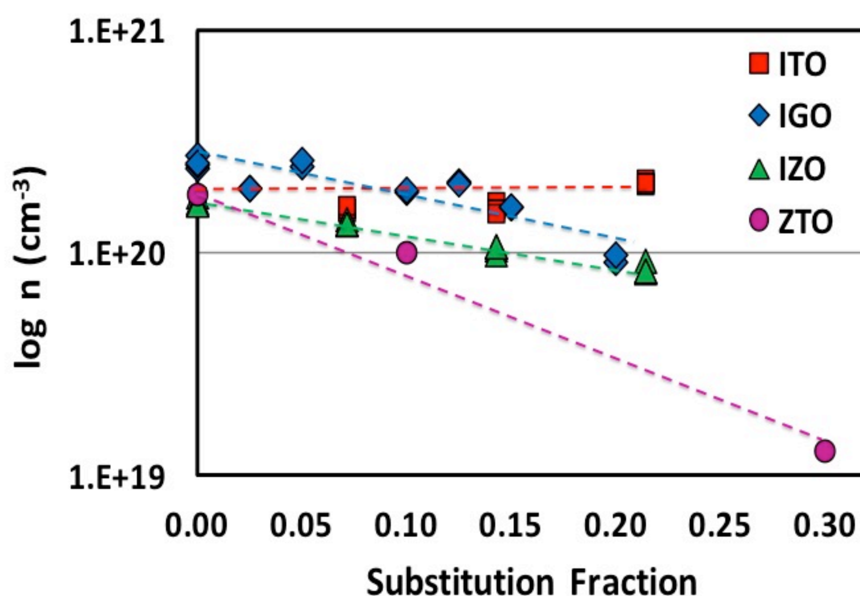

Figure 2.1 Comparison of carrier concentration (n) as a function of substitution fraction (at%) of secondary cations in the amorphous indium oxide and amorphous tin oxide systems. Measurements and film synthesis performed by Dr. D. Bruce Buchholz.

Multiple studies have explored the effect of oxygen pressure during film deposition in order to tailor the conductivity and photoconductivity response of amorphous oxide materials.[10, 20-21] These results have suggested that oxygen vacancies are the primary source of carriers in

amorphous oxide materials. However, direct experimental evidence of the dominant defect mechanism has only recently been reported. Work by Lee *et al.*[26] and Adler *et al.*[27] have provided experimental results pointing to oxygen vacancies as the dominant defect species in a-IZO (In_2O_3-ZnO) and a-IGZO, respectively. Both groups employed the method of Brouwer analysis, a well-established technique for identifying dominant defect mechanisms in polycrystalline materials. Traditional Brouwer analysis is conducted with bulk polycrystalline samples at high temperatures (above 600°C) where carrier concentration is driven to equilibrium at different oxygen partial pressures (pO_2).[28-31]A log-log plot of the resulting equilibrium conductivity vs. pO_2 yields a signature slope consistent with the underlying defect mechanism.

The amorphous nature of a-TCOs provides several challenges to traditional Brouwer analysis. Of particular importance is the limit of temperature, which must remain low to avoid both recrystallization and structural relaxation.[27, 32] Thus, careful and creative measures must be employed to extend the method of Brouwer analysis to amorphous materials. In a-oxides, Brouwer analysis has, to date, only been reported for a-IZO[26] and a-IGZO[27]. In order to further the application of Brouwer analysis to a-oxides this work seeks to corroborate the results of both Lee *et. al.* [26] and Adler *et al.*[27] by applying *in situ* methods to a-IZO.

2.3 Thermal Stability of Amorphous Oxides

The thermodynamically unstable nature of amorphous oxides has promoted multiple inquiries into the limitations of thermal stability in amorphous oxides.[4, 33-36] The additional of modifying cations has been shown to increase thermal stability.

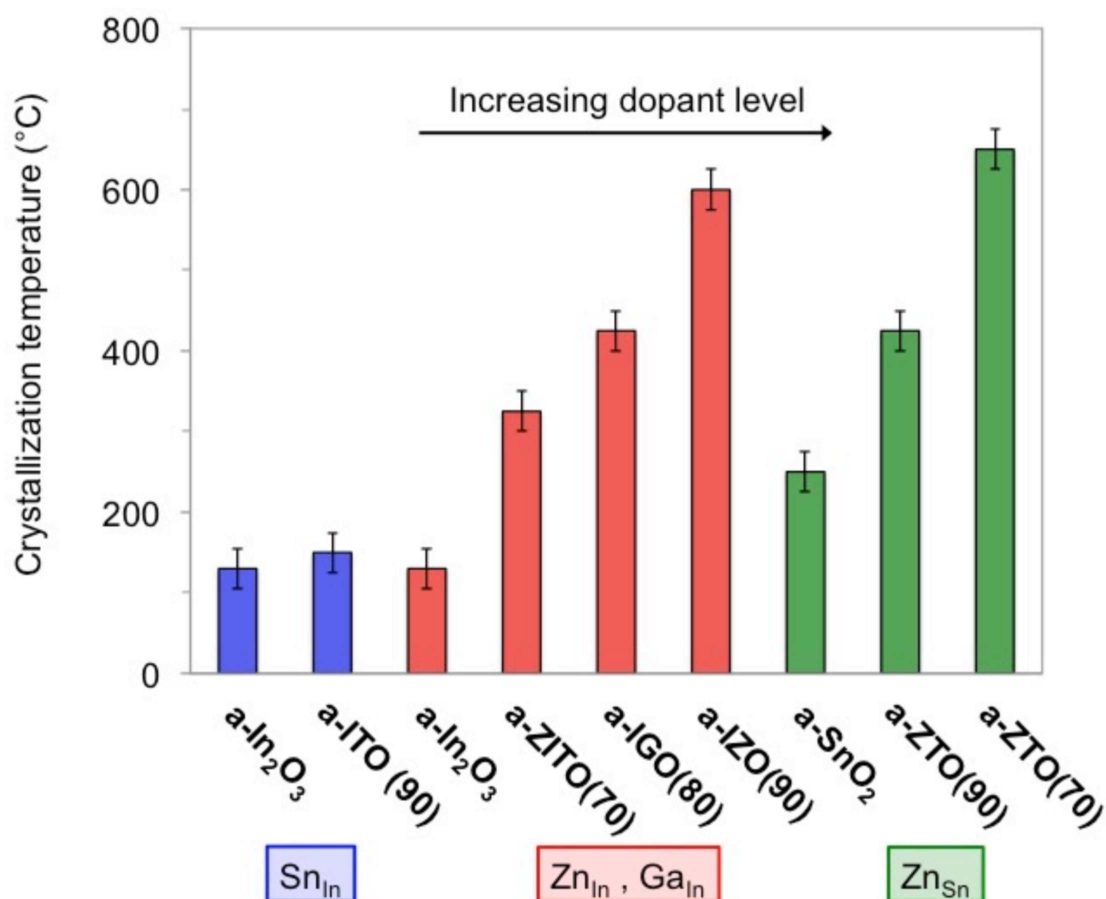

Figure 2.2 Comparison of crystallization temperature as a function of substitution fraction (at%) of secondary and tertiary cations in the amorphous indium oxide and amorphous tin oxide systems. [14, 34, 37-39]

The biggest effects are seen with substitutional cations that are significantly larger or smaller than the matrix cation (Fig. 2.2).[40] Early work by Ide demonstrated the film densification occurs at a lower temperature than film crystallization.[35] However most thermal stability studies of amorphous oxides are performed only with *ex situ* GIXRD after only 1 or 2 air-annealing steps.[14, 33, 37, 41] Recent work at Northwestern has begun to employ in situ studies of crystallization through both GIXRD and TEM.[34, 36] These studies are paired with theory to begin developing an understanding of the mechanisms that govern the crystallization of amorphous oxides.

CHAPTER 3: **Synthesis and Characterization Techniques**

3.1 Film Growth

3.1.1 Physical vapor deposition

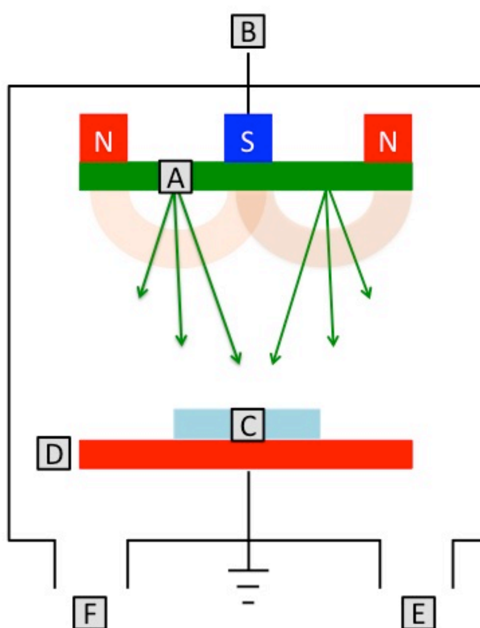

Figure 3.1. In DC magnetron sputtering a conductive target A) acts as a cathode and is connected to the negative terminal of a DC power supply B). Opposite the target is the substrate C) on top of the anode D). The chamber is evacuated with a vacuum E) and back filled with the working gas, typically argon F). Once a glow discharge is maintained, current flows between the cathode and the anode. Positive gas ions in the discharge strike the cathode and eject atoms (green arrows) that deposits onto the substrate. Magnetic field lines (orange arcs) are created over the target to stabilize the discharge. [42]

Physical vapor deposition methods (PVD) are used to grow amorphous oxide thin films in a majority of the literature. In this work, films were grown by two types of PVD methods: DC magnetron sputtering and pulsed laser deposition (PLD). When depositing amorphous oxides both methods are expected to give very similar films. The main difference between these methods is the source of energy used to ablate material from the ceramic target. In both cases a plume made of atoms and clusters of atoms is released from a target and deposits onto a substrate. During sputtering a stream of argon ions are simultaneously created and directed towards the target by applying a current across the deposition chamber (Fig. 3.1). When lower pressures and minimum target voltage are preferred, magnetic fields are created over the target and a stable discharge of target material can be maintained. When sputtering employs magnetic fields in this way it is referred to as magnetron sputtering. When sputtering from a multicomponent target, as was done for the deposition of a-In-Zn-O (chapter 6), the initial flux can deviate from target stoichiometry, due to differences in surface binding energy and atomic mass of the target atoms. Thus, targets must first be brought to steady state before reliable composition can be obtained.[42]

As the name suggests, pulsed laser deposition uses a high-powered laser to ablate atoms from the surface of a target. Each laser pulse creates a sub-monolayer distribution of atoms on the substrate surface. This allows doped films to be created by alternating ablation between

multiple targets[42] (Fig. 3.2) as was done for the deposition of a-IGO (chapters 4,5, and 7). In both PLD and sputtering the target-to-substrate distance and the ablation power must be tuned to ensure uniform coverage of the substrate. Substrates can be heated or cooled during deposition to alter the atomic order of the resulting film. PVD methods are typically performed under vacuum or in an inert atmosphere however, a reactive gas such as oxygen can be introduced into the deposition chamber to modify the deposited film.[42]

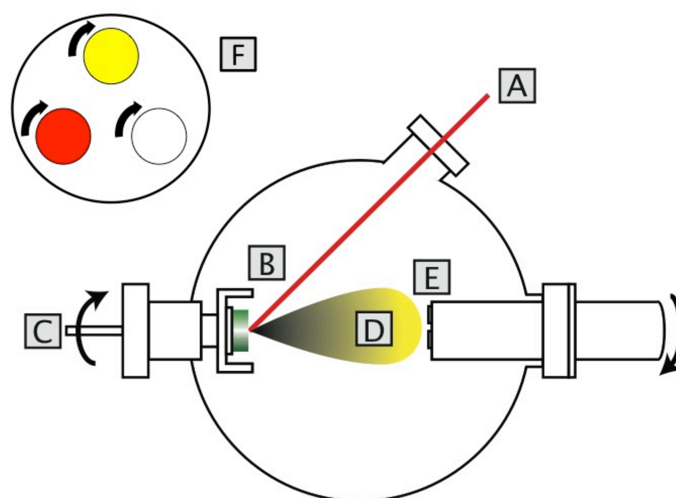

Figure 3.2. Pulsed laser deposition features a 248nm KrF excimer-laser A) which ablates a ceramic target B). Doped samples are created by rotating C) to choose from different targets F). Each ceramic target is additionally rotated to ensure efficient ablation of the target. A plasma plume of material D) is created by the laser and deposits onto the substrate E). The deposition temperature can be modified by heating or cooling the substrate holder. Figure adapted from Alex U. Adler's thesis.[17]

3.1.2 Solution processing

Solution processing of a-oxides stands apart from PVD methods because of its potential for roll-to-roll processing of printed electronics. Traditional solution processing requires elevated substrate temperatures during processing which precludes the use of flexible plastic substrates.[6] Recently, the Marks group has applied combustion synthesis a new method of solution processing amorphous oxides.[43-44] In this method an internal fuel (typically acetylacetone) is added to an aqueous solution of metal nitrate salts (oxidizers). The internal fuel supplies a source of energy via the exothermic reaction which occurs upon low temperature annealing (Fig. 3.3).[44] This additional source of energy dissipates almost instantly, but it is enough to reduce the global processing temperature of a-oxide films to 300°C and below. At these temperatures, plastic substrates are stable.[43-45]

Combustion synthesis of films is achieved either through a spin coating process (Fig. 3.3) or a spray coating process. For the spin coating process, the metal nitrate solution is deposited drop wise onto a substrate attached to a spin coater. After spin coating the sample is placed on directly onto a hot plate at 200-300°C. This process is repeated 4-15 times to create films between 10 and 50 nm thick. For the spray-coating process, the metal nitrate solution is sprayed

through an ultrasonic nozzle directly on to a substrate sitting on a hot plate. In both processing methods, the final film is placed in a low-humidity box for a final annealing step.

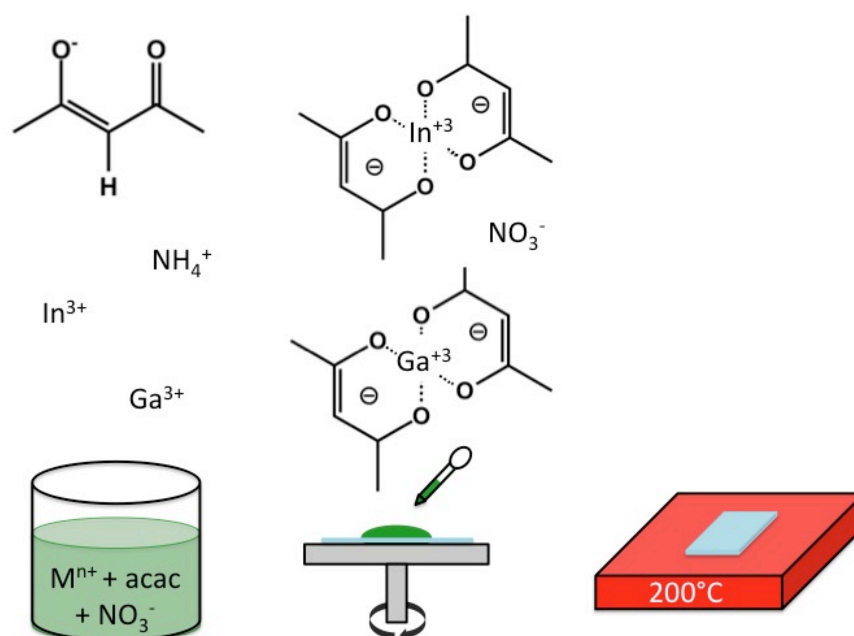

Figure 3.3. Combustion solution processing begins with an aqueous solution of dissolved metal nitrates and acetylacetone. This solution is spin coated onto a substrate and then placed directly onto a hot plate. The metal nitrate solution can also be sprayed through an ultrasonic nozzle directly onto a substrate sitting on a hot plate.

3.2 Structural Characterization and X-ray Techniques

3.2.1 Ellipsometry

Ellipsometry is a technique that determines film thickness by measuring the change in polarization direction that occurs when light is reflected from a film. This technique is often used

for thicker films (~ 1μm) that are beyond the resolution of typical lab-based XRR. A beam of light with known intensity, polarization, and incident angle is reflected from a film. The polarization of the reflected beam is given by the fundamental ellipsometry equation:

$$\rho = \frac{r_p}{r_s} = \tan(\psi)e^{i\Delta} \tag{3.1}$$

Where ρ is the ratio of reflectivity in the parallel direction (r_p) and the perpendicular direction (r_p). ψ and Δ are measured experimentally and depend on the dielectric constant of the film and the substrate, as well as the film thickness. In this work, the optical properties of the Si and SiO_2 substrates are well established. The Woollam ellipsometry software CompleteEASE is used to fit the optical constants and thickness of the films. Multiple-Angle-of-Incidence ellipsometry, using incident angles of 55°, 65°, and 75°, is employed to improve the accuracy of the fits.

3.2.2 X-ray characterization techniques

X-ray techniques are well suited to nondestructively study the structure of thin films, and their surfaces/interfaces, at multiple length scales. The refractive index (n) of X-rays for materials is slightly less than unity:

$$n = 1 - \delta - i\beta \tag{3.2}$$

Where δ is the wavelength-dependent scattering term and β is the wavelength dependent absorption term. As shown in Fig 3.4A, n being less than 1 causes the refracted angle (α') inside the medium to be less than the external incident angle (α). This is based on Snell's law:

$$\cos(\alpha) = n\cos(\alpha') \tag{3.3}$$

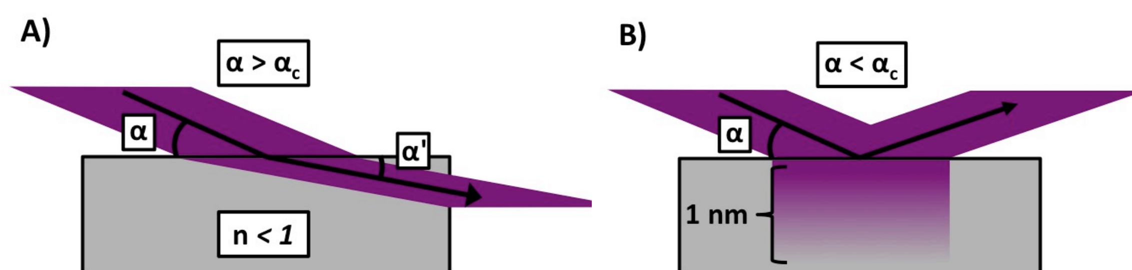

Figure 3.4. A) For X-rays, the index of refraction (n) for materials is less than 1. This results in the refracted angle (α') of X-rays being smaller than the incident angle (α). B) When the incident X-ray angle (α) is less than the critical angle (α_c), total external reflection occurs. At this condition, an evanescent wave penetrates into the material with a rapidly diminishing intensity characterized by an effective attenuation length of 1 to 10 nm. Figures adapted from Elements of Modern X-ray Physics. [46]

This relationship dictates that total external reflection will occur at small incident angles α (Fig. 3.4B) that are less than the critical angle (α_c), which is a function of the X-ray wavelength (λ) and electron density of the material (ρ).

$$\alpha_c = \sqrt{2\delta} = \frac{\lambda}{2\pi}\sqrt{4\pi\rho r_0} \quad (3.4)$$

Here r_0 is a constant equal to *2.818 x* 10^{-6} *nm*, the classical electron radius. At the critical angle and below, a highly surface-sensitive evanescent wave exists below the surface; its E-field intensity decaying rapidly with depth (Fig. 3.4B). In this work In_2O_3-based samples were measured with Cu kα rotating anode with λ = 1.54Å. Given that the electron density of In_2O_3 is 1.90 $e^-/Å^3$, α_c is calculated as 0.0064 radians or 0.36°.

3.2.3 Grazing incidence geometry

When studying thin films, the grazing incidence (GI) geometry is often used. Grazing incidence geometry refers to α being held in the vicinity of α_c, where the limited penetration depth of the X-rays (Fig. 3.5) results in maximizing the signal from the film and minimizing the signal from the substrate. The penetration depth or effective attenuation length (Λ) of a given incident angle can be calculated as follows:

$$\Lambda = \frac{\lambda}{2\pi}\left(Re\{[\alpha_c^2 - \alpha^2 + 2i\beta]^{1/2}\}\right)^{-1} \quad (3.5)$$

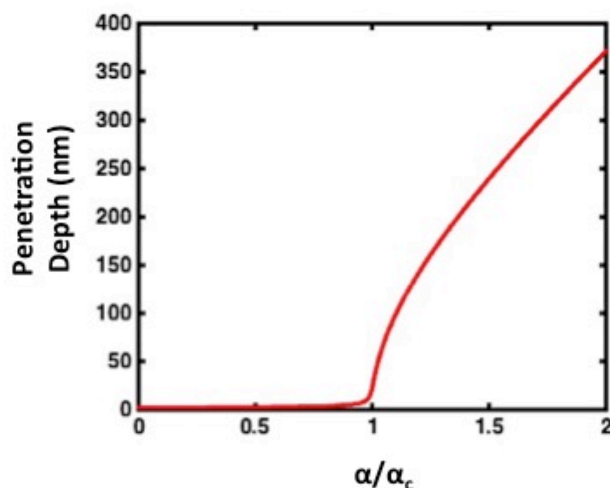

Figure 3.5. Above the critical angle (α_c), X-ray penetration depth rises quickly and approaches $\sin\alpha/\mu$. A suitable grazing angle can be determined based on the thickness of the film.

3.2.4 X-ray diffraction

With X-ray diffraction (XRD) one can use the presence of a short-range order (SRO) broad peak referred to as the "amorphous hump" and the lack of X-ray diffraction peaks to confirm the amorphous nature of oxide thin films. In the case of a crystalline film X-rays are diffracted by the lattice planes and produce sharp peaks in intensity following Bragg's law:

$$2d\sin(\theta) = n\lambda \tag{3.6}$$

Where θ is the angle between the incident beam and the lattice plane, λ is the wavelength of the X-rays, and d is the lattice plane spacing. Noting not only position of the peaks, but also their relative intensities, the diffracting phase can be identified. The intensity of each diffraction peaks

is a function of its structure factor (F), Lorentz polarization factor (LP), multiplicity (m), and absorption factor (A).

$$I\ (hkl) = |F|^2 \cdot LP \cdot m \cdot A \tag{3.7}$$

GIXRD can also be used to study of the onset of crystallization during annealing studies. Scanning a point detector through 2θ initially reveals the broad-range, low-intensity scattering hump from the amorphous film. As crystallization begins to occur the crystalline fraction of the film diffracts and the 2θ scan reveals a superposition of diffraction peaks and the amorphous hump (Fig. 3.6). In this partially crystalline state the degree of crystallinity can be calculated by dividing the area under the crystalline peaks by the area under the entire spectrum.

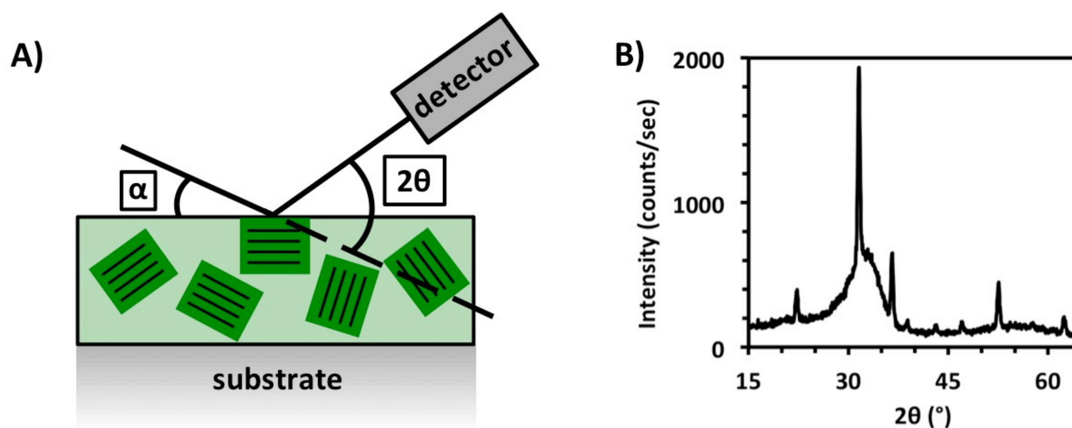

Figure 3.6. A) In GIXRD geometry the incident X-ray angle (α) is held just above the critical angle to limit the penetration depth in the material. The point detector is scanned through a range of 2θ angles to collect X-ray diffraction from the crystalline portion of the sample. B) In a partially crystalline film the X-ray diffraction pattern is a superposition of the broad scattering hump originating from the amorphous portion of the sample and the strong diffraction peaks originating from the crystalline portion of the sample.

3.2.5 X-ray absorption spectroscopy

X-ray absorption spectroscopy (XAS) utilizes the photoelectric effect to gain element specific, chemical state and local structure information. X-rays energies are on the order of the binding energies of core-shell electrons. When the energy of an incident X-ray matches the binding energy of a core-shell electron, a photoelectron is ejected and a sharp rise in X-ray absorption occurs (Fig. 3.7A and B). The rise in X-ray absorption is called an absorption edge; the X-ray energy at which a 1s core-shell electron is ejected is specifically called a K-edge. Since the electronic structure of each element is unique, the K-edge of each element is unique. The ability to tune X-ray energies to a specific K-edge is what makes XAS an element specific technique. The specific energy and shape of an observed absorption edge also provides information about the ionization state of that element. An element with a higher valence will require additional energy to eject a core electron, thus the K-edge will be observed at a higher X-ray energy (Fig. 3.7A).

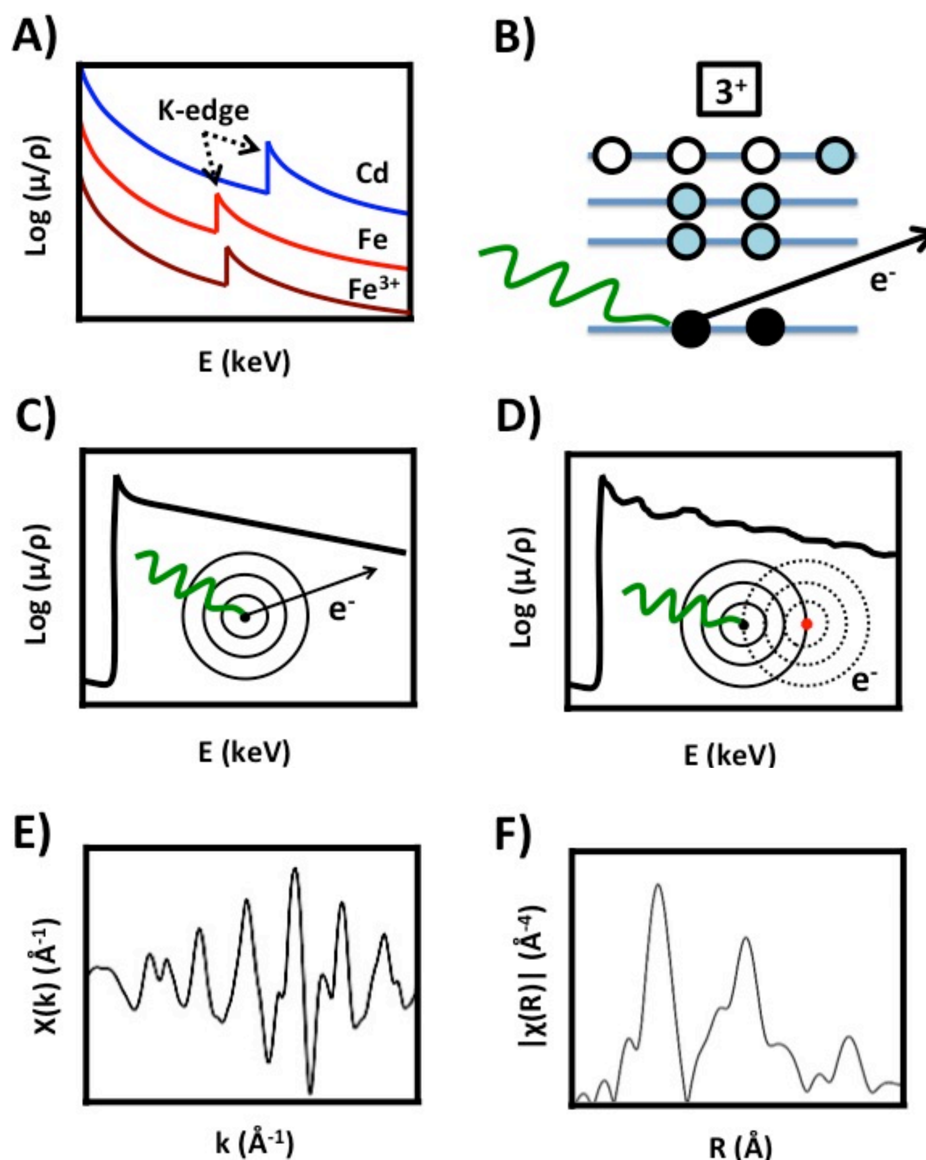

Figure 3.7. A) Each element has a unique absorption edge that depends on the energy of its core-level electrons, If an atom is ionized the edge position will shift. B) At the K-edge energy, X-ray absorption increases because a core-level photoelectron is ejected. The ability of light to eject electrons is known as the photoelectric effect. C) In a bare atom, or monatomic gas, the photoelectron leaves the atom and decays. It has no effect on the absorption spectrum. D) When the excited atom has a neighboring atom, the photoelectron has a probability of scattering back and causing interference in the absorption. E) EXAFS data are converted from energy space to inverse space (k-space) before fitting is performed. F) Fourier transforms of k-space EXAFS data reveal pseudo-radial distribution functions that are useful for visualizing data.

In a monatomic gas the ejected photoelectron will escape into the continuum (Fig. 3.7C). However, in any material more complex, even a diatomic gas, the outgoing photoelectron will scatter off neighboring atoms causing oscillations in the absorption spectra (Fig. 3.7D). These oscillations provide information about the local environment around the atom where the photoelectron originated. Synchrotron radiation sources are typically used for XAS measurements because the requirement of a continuous range of high energy X-rays generally precludes the use of lab sources. XAS data analysis is commonly broken up in to two regions (Fig. 3.8). X-ray absorption near-edge structure (XANES) refers to qualitative analysis of the data near the absorption edge. XANES data can yield both the ionization state and local geometry around the element of interest. This information is typically gained by comparing the data to a reference sample where the ionization state and site geometry are already known. Extended X-ray absorption fine structure (EXAFS) analysis utilizes the data at higher energies beyond the absorption edge. The data are fit using the EXAFS equation from which the location, identity, and number of atoms that surround the atom of interest can be determined.

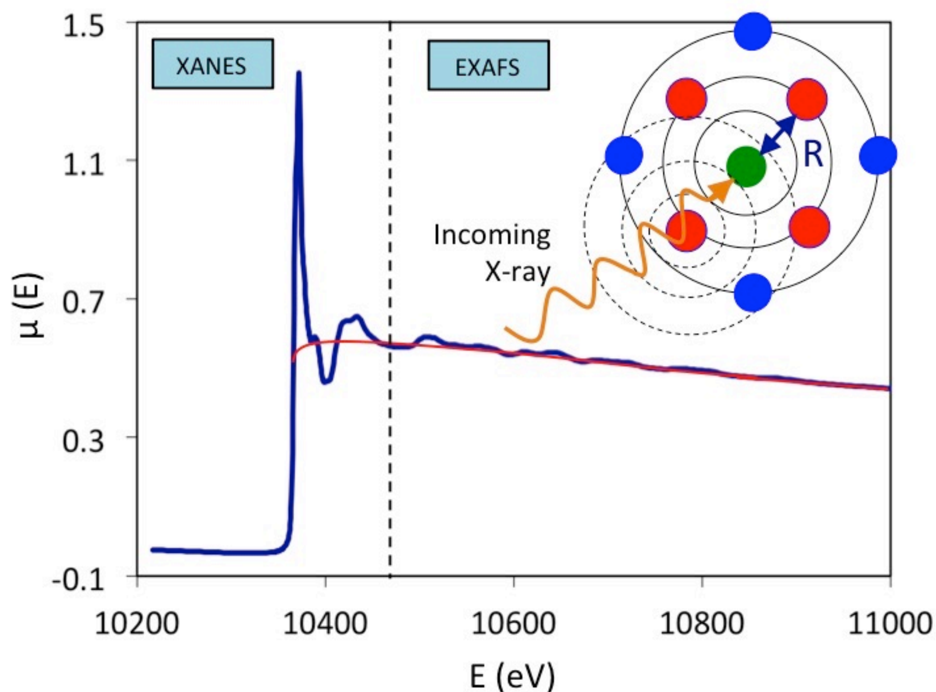

Figure 3.8. Normalized absorption as a function of incident photon energy is shown in dark blue. The absorption of a bare atom is shown in red. XAS is typically broken up in to two techniques. Analysis of data near the absorption edge reveals the "X-ray absorption near-edge structure" (XANES) and the data farther out in energy reveals the "extended X-ray absorption fine-structure" EXAFS.

To derive the EXAFS equation the outgoing photoelectron is treated as a wave. The kinetic energy (KE) of the ejected photoelectron is equal to the energy of the incident X-ray ($\hbar\omega$) minus the binding energy of the core electron (E_B). Thus, the wavelength of the outgoing photoelectron (λ_{pe}) decreases as the incident X-ray energy increases beyond the K-edge:

$$KE = \hbar\omega - E_B \quad (3.8)$$

$$\lambda_{pe} = \frac{\hbar}{\sqrt{2m_e(\hbar\omega - E_B)}} \Rightarrow \lambda_{pe}(\text{Å}) = \frac{12.3}{\sqrt{KE(eV)}} \tag{3.9}$$

In the energy range of EXAFS, λ_{pe} is on the order of Å and is therefore ideal for probing atomic-scale local structure.

The outgoing photoelectron wave can be treated as a spherical wave that scatters off neighboring atoms as a function of incident wave (Ψ_0), scattering probability (f) and the distance to the neighboring atoms (R). The phase shift (φ) and the scattering probability of the scattered photoelectron wave are both dependent on the elemental identity of the neighboring atoms.

$$\Psi_{scattered} = \frac{\Psi_0}{R^2} f e^{i(2kR+\varphi)} \tag{3.10}$$

Due to quantum nature of photoelectrons, knowledge of the wavelength, and in turn the momentum, requires that the position of the photoelectron is unknown. Therefore, the true wave equation at the element of interest (Ψ_{total}) is described by the superposition of both the outgoing photoelectron wave (Ψ_0) and the back-scattered photoelectron wave.

$$\Psi_{total} = \Psi_0 + \Psi_{scattered} \tag{3.11}$$

In this way, the back-scattered photoelectron influences the emission of photoelectrons from the element of interest and results in the oscillations of X-ray absorption cross-section. In a simplified two-atom model the intensity of the absorption spectrum (I) is just the complex conjugate of the Ψ_{total}.

$$I = \Psi_{total}\Psi_{total}^{*} = 1 + \frac{2f}{R^2}\sin(2kR + \varphi) + \frac{f^2}{R^4} \tag{3.12}$$

The third term is sufficiently small and is therefore neglected. In the full EXAFS equation, a summation is added to account for the multiple distances of different neighboring atoms. Typically, the 1st set of neighbors (j = 1) (Fig. 3.8, red atoms) is described as the first shell, the second set of neighbors (j = 2) (Fig. 3.8, blue atoms) as the second shell.

$$\chi(k) = \sum_{j} \frac{N_j f_j(k)\sin[2kR_j + \delta_j(k)]\, e^{-2k^2\sigma_j^2} e^{-\frac{2R_j}{\lambda(k)}}}{kR_j^2} \tag{3.13}$$

Fitting XAS data to the full EXAFS equation reveals quantitative information about bond lengths (R), bond disorder (σ^2), and coordination number (N). The elemental identity of the neighboring atoms is derived from the phase shift (φ) and the scattering probability (f). Before fitting, absorption ($\chi(E)$) is first normalized to ($\mu(E)$) by subtracting the theoretical absorption of a bare atom with no neighbors ($\mu_0(E)$) to isolate the oscillations which contain the local structure information. [47] Fits are typically performed on data that has been converted to inverse Å (k-space) (Fig. 3.7E). Fourier transforms of k-space data yield pseudo radial distribution functions that are often useful for visualizing the local structure in real space (Fig. 3.7F).

3.2.6 X-ray fluorescence

X-ray fluorescence (XRF) is similar to XAS in that it relies on the photoelectric effect. After an atom absorbs an X-ray and ejects a photoelectron (Fig. 3.7B) the atom briefly exists in an excited state. The atom relaxes back to the ground state by filling the core-level hole, left behind by the photoelectron, with an electron from an outer orbital. The binding energy difference between the outer-shell and the core-shell can be released as an X-ray photon: this process is known as X-ray fluorescence (Fig. 3.9). Relaxation can also be non-radiative, which leads to ejection of an Auger electron.

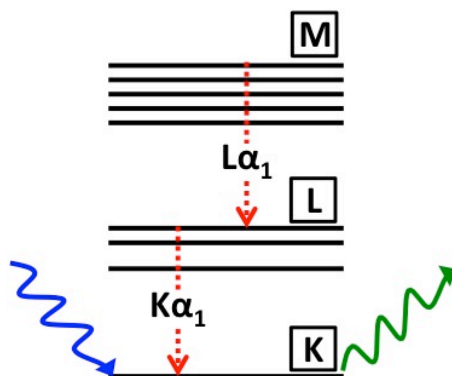

Figure 3.9. Once a photoelectron is ejected by an incident X-ray (blue) from the core (K) level or outer levels (L), an electron from a higher level (L or M) drops down and the atom is relaxed. A fluorescence X-ray (green) is released upon this relaxation event. The energy of the ejected photon depends on the energy difference between the two levels.

As in XAS, XRF is element specific because the electronic structure of each element is unique. A single energy X-ray source, Mo K-alpha (E = 17.48 keV) in this work, is used to excite a sample. Fluorescent lines are then detected at energies corresponding to the elemental identity of the sample and the orbital origin of the transition. For a given element relaxation between the M and L levels will result in lower energy X-ray fluorescence than transitions between the L and K levels (Fig. 3.9). By determining the intensity of fluorescence lines the composition/atomic ratio of a sample can determined. Quantitative compositional information requires that fluoresce intensities are corrected for their photoelectric cross section and fluorescence yield as well as the effects of self- absorption, air absorption, and detector efficiency (see Appendix A).

3.2.7 X-ray reflectivity

When X-rays are incident on a thin film they can reflect not only off the air-film interface but the film-substrate interface as well. These two reflecting interfaces result in wave interference and observed oscillations in the reflectivity intensity. These periodic oscillations in the reflectivity intensity are known as Kiessig fringes. The spacing of these fringes (ΔQ) results from the thickness of the film (t).

$$t = \frac{2\pi}{\Delta Q} \tag{3.14}$$

Where:

$$Q = \frac{4\pi \sin(\frac{2\theta}{2})}{\lambda} \tag{3.15}$$

Expanding beyond a simple one-dimensional interference function, the density of the film and the substrate can be considered. The density contrast of the interface will primarily affect the height of the thickness fringes (Fig. 3.10). Most physical systems also lack a perfectly sharp interface and instead have a density gradient at the interface. In the weak (kinematical scattering) reflectivity region, R < 0.1, the ratio between the measured reflectivity (*R(Q)*) and that of a perfectly sharp substrate ($R_F(Q)$) is a function of the density profile of the interface (*f(z)*).[12, 46]

$$\frac{R(Q)}{R_F(Q)} = \left| \int_{-\infty}^{\infty} (\frac{df}{dz}) e^{iQz} dz \right|^2 \tag{3.16}$$

In practice, analysis of X-ray reflectivity data (XRR) is done with the Igor Pro (Wavemetrics) MOTOFIT[48] fitting package, which uses the more rigorous dynamical scattering theory from Parratt's[49] multilayer recursion formulation. Model fits of reflectivity data reveal the thickness, density, and roughness of thin films. Films that are 5-20 nm thick provide the best samples for reflectivity measurements, especially if interfacial roughness is less than 1 nm. Fringe spacing is inversely proportional to film thickness and therefore the angular resolution of lab X-ray sources typically precludes the measurement of thicker films (> 1 μm).

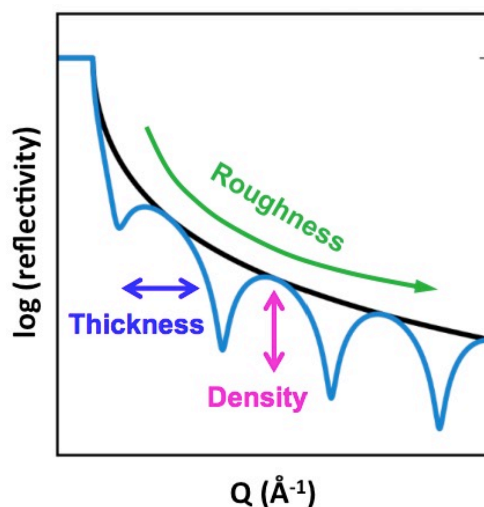

Figure 3.10. XRR measurements can provide the thickness, density, and roughness of thin films through the analysis of Kiessig fringes.

3.3 Electrical Characterization

3.3.1 Hall probe

Utilizing the Hall effect, carrier type, carrier concentration, and mobility can be determined. A magnetic field is applied perpendicular to the thin film surface and a current is applied diagonally across the film surface (Fig. 3.11). A resulting Hall voltage (V_H) is created orthogonal to both the magnetic field and the current. Applied current (I) and magnetic field (B) are related to V_H through equation 3.17.

$$V_H = -\frac{IB}{n_s e} \tag{3.17}$$

Where e is the charge of an electron and n_s is the area carrier concentration. Bulk carrier concentration (n) is produced by dividing n_s by the film thickness. The identity of the dominant carriers is given by the sign of n, where holes are shown by a positive value and electrons by a negative value.[50] By additionally recording sheet resistance (R_s), carrier mobility can be derived through the following equation:

$$\mu = \frac{1}{en_sR_s} \tag{3.18}$$

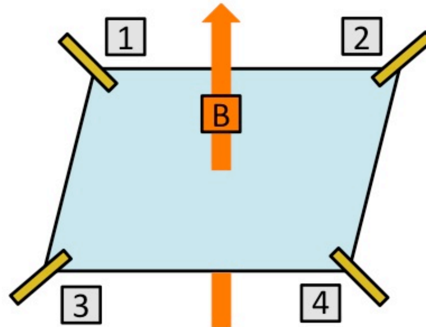

Figure 3.11. Hall-probe set up: Films are contacted in van der Pauw configuration by four gold probes. Current is applied diagonally (i.e. from contact 2 to 3) and the resulting voltage is measured perpendicular (i.e. from contact 1 to 4). IV curves are run before each measurement to ensure ohmic behavior.

CHAPTER 4: **The Role of Ga in the Local Structure and Thermal Stability of a-IGO**

This chapter explores the role of Ga in amorphous oxide semiconductors through combined theory and experiment. It exposes the impact of Ga substitution on the thermal stability of amorphous (a-) indium oxide (IO), an effect that has not previously been highlighted. A systematic study is performed on series of pulsed laser deposited a-In-Ga-O thin films. Element-specific structural studies (X-ray absorption and anomalous scattering) are combined with room temperature MD simulations to understand the results of thermal property (air-annealing) studies. The crystallization temperature of a-IO is shown to increase as much as 325°C by substituting Ga for In. This increased thermal stability is understood by revealing the persistence of low Ga-O coordination despite the surrounding higher coordinate matrix. Large changes must occur in the local structure that surrounds Ga, as compared to In, during crystallization. This understanding suggests that preferred coordination of substitutional cations is an important consideration for improving the thermal stability of amorphous oxides.

4.1 Introduction

Much of what is understood about transparent conducting oxides (TCOs) comes from structure-property relationships that presuppose the presence of long-range order. Crystalline TCOs helped revolutionize display technology, but their high deposition temperatures prohibit the use of flexible plastic substrates.[11] Required for the new frontier of display technology, deposition on flexible substrates can be realized with the use of amorphous (a-) TCOs created through low-temperature deposition. The consequence of low temperature is a loss of long-range structural order, which negates the use of characterization techniques such as X-ray diffraction and simulations with periodic boundary conditions. We employ local structure, element-specific, X-ray measurements, performed at the Advanced Photon Source, to gain an understanding of how cation composition affects the local structure in a-TCOs. The present investigation successfully couples these X-ray techniques with *ab-initio* molecular dynamics simulations. The close agreement achieved between theory and experiment provides a comprehensive understanding of the a-IGO structure.

Amorphous indium oxide (a-IO) often serves as the matrix material for oxides semiconductors used as the channel layer in thin film transistors (TFTs). However, a-IO is not a viable TFT device material on its own. a-IO has very low thermal stability, which can lead to the

breakdown of performance at high temperatures.[15, 37] To optimize the properties of a-IO the common practice, originating empirically, has been to add both Ga and Zn.[10, 51] Although these modifying cations improve the TFT performance of a-IO, a fundamental mechanistic understanding of how these cation modifiers influence the thermal stability of amorphous oxide is currently unresolved.

This study focuses on isolating the influence of Ga, which is rarely studied in the absence of Zn. The simpler two-cation system a-In-Ga-O (a-IGO) is employed here to elucidate the role of Ga in the thermal stability of a-IGO. Thermal stability in amorphous oxides refers to the tendency of these materials to resist the onset of crystallization. To maintain competitive TFT mobility, amorphous oxides must avoid nano- or micro- inclusions of crystallites that act as scattering centers.[15, 52] Small inclusions of crystalline phase always occur at the onset of crystallization. Thus, a sufficiently high crystallization temperature (T_{cryst}) is important to provide a thermal window for post-deposition processing without initiating crystallization. Substitutional cations have been shown to inhibit crystallization during post-deposition annealing as well as crystalline-phase growth from the vapor or solution phases.[9, 33-34, 40-41, 53] However, an understanding of which cations inhibit crystallization and why, is lacking. The results of the present study show that Ga substitution alone is capable of significantly increasing the T_{cryst} of

a-IO. The present structural studies clearly reveal that substitutional Ga cations displace the amorphous structure farther away from thermodynamic equilibrium, and that to undergo crystallization, large changes must occur in the oxygen coordination and bonding around the Ga cations.

4.2 Methods

4.2.1 Film growth

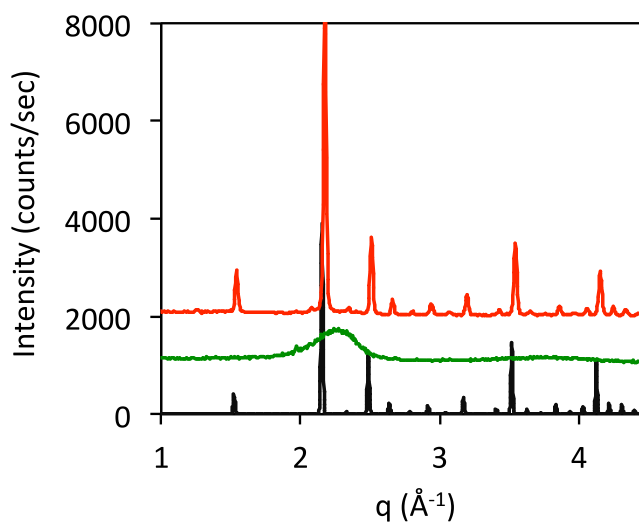

Figure 4.1. GIXRD data at 8.04 keV of a representative a-IGO thin film (8 at% Ga) as deposited (green, middle) and after air annealing has caused crystallization (red, top). For reference, the cubic $Ia\bar{3}$ In_2O_3 bixbyite powder[1] XRD pattern is shown in black (bottom). The small shift in the peak position is due to the lattice contraction induced by Ga substitution.

A series of a-IGO thin films was grown by pulsed laser deposition (PLD) in collaboration with Dr. Bruce Buchholz of the Chang group. A 248 nm KrF excimer-laser with a pulse duration of 25 ns and a beam energy of 200 mJ/pulse was employed. The beam was focused to a 1×2 mm^2 spot on the target material. Films were grown in a 7.5 mTorr O_2 environment and deposited onto quartz substrates (1×1 cm^2 and 1×2 cm^2 for local structure measurements). A deposition temperature of -25°C was chosen to ensure all films would be grown amorphous[15] (Fig. 4.1). Various Ga: In ratios were achieved by alternating ablation between an In_2O_3 target and a Ga_2O_3 target. Less than 1 monolayer is deposited during each In_2O_3/ Ga_2O_3 PLD cycle to insure mixing at the atomic-layer level. To prevent localized heating, the targets were rotated at 5 rpm and the laser beam was rastered radially. The target-substrate distance was fixed at 10 cm. Ellipsometry (J. A. Woollam M2000U Ellipsometer) indicated that the films were between 250 and 350 nm thick.

X-ray fluorescence spectroscopy (XRF) was performed to verify the correct In:Ga atomic ratio achieved in each film. XRF measurements were performed on an 18-kW rotating anode, two-circle diffractometer with multilayer monochromated Mo Kα radiation ($E = 17.4$ keV) operating at 50 kV and 160 mA. A Kapton bag filled with N_2 gas was placed over the sample to limit the signal from Ar. Spectra were taken at an incident angle of $\theta = 5°$. The horizontal by

vertical beam footprint at the sample was 0.6 × 6.3 mm^2 and the total collection time for each sample was 10 minutes. XRF data were collected with a Vortex-EM 350 μm thick silicon drift detector. The detector to sample distance was 8 mm. The Ga K and In L fluorescence yields were background subtracted, dead-time corrected and corrected for the different XRF cross-sections[54-58] and detector efficiency. See table below for example calculation:

$$D = \frac{A}{B} \div C \qquad E = \frac{D_{Ga}}{D_{Ga} + D_{In}} \tag{4.1}$$

	Integrated area of the peak (A)	XRF cross-section (B)	Detector efficiency (C)	Corrected peak intensity (D)	Atomic percent Ga (E)
Ga K alpha	2197077	2452.585	0.9618	861.6	41.9%
In L alpha	198893.0	166.8097	1.000	1192	

4.2.2 Crystallization study

Grazing incidence X-ray diffraction (GIXRD) was performed using a Rigaku Smartlab instrument with a multilayer monochromated Cu rotating anode source. GIXRD was used to study the thermally induced film crystallization process. The incident angle of the 8.04 keV X-ray beam was set at 0.4°. The critical angle for In_2O_3 is 0.37° at this energy. A GI geometry was used to avoid scattering from the substrate. To determine the T_{cryst} each film was subjected to a heat-quench-measure cycle. Samples were heated in air for 1.0 h and then quenched to 25°C.

Heating began at 50°C and was increased in each cycle by 25°C until strong crystalline diffraction peaks could be observed (Fig. 4.1). We use this to define the T_{cryst}, above which no further change in the diffraction pattern is observed. All crystalline samples were fit using whole pattern fitting in the MDI Jade software package (Materials Data, Inc., Livermore, CA) to confirm the crystalline phase and determine lattice parameters.

4.2.3 Short and medium-range structural characterization

The structures of the a-IGO films were studied using X-ray absorption spectroscopy (XAS) and X-ray scattering techniques. Both X-ray absorption and X-ray scattering measurements were carried out in collaboration with Dr. Qing Ma using synchrotron X-rays delivered from the bending magnet 5-BM-D beamline of the DuPont-Northwestern-Dow Collaborative Access Team at the Advanced Photon Source (APS) of Argonne National Laboratory. The beamline is equipped with a Si (111) double-crystal monochromator with energy resolution of $\Delta E/E = 1.4\times10^{-4}$, a vertical collimating mirror, and a vertical focusing mirror. Both the reflecting surfaces of the mirrors are Rh-coated. The maximum cut-off energy is ~21 keV. These mirrors were used in our X-ray scattering measurements for harmonic rejection and increasing the X-ray flux density (by ~10 fold). For X-ray absorption measurements, the harmonic rejection is achieved by detuning the monochromator. The incident X-ray intensity was detuned to 60% of

its maximum. XAS data were collected in fluorescence mode at the In and Ga K-edges, respectively, using a 4-element Si-drift detector (Vortex-ME4) with DXP-XMAP electronics (XIA LLC). The peaking time for pulse-height analysis was set at 1 μs, to insure dead-time effects were within a correctable range for a total counting rate that never exceeded 80,000 cps (counts per second) per detecting element. The samples were held vertically and the X-ray incidence angle was set at 54° to ensure that the best average structure was measured. The Vortex-ME4 detector was placed 90° to the X-ray beam direction or 54° to the sample surface normal.

For amorphous materials, the XAS measurements reveal, in most cases, only the structure of the nearest neighbor surrounding the atom of interest. In order to probe the structure beyond the first neighbor, grazing-incidence wide angle X-ray scattering (GIWAXS) measurements at a photon energy of 15.00 KeV and anomalous GIWAXS (A-GIWAXS) measurements around the Ga K edge were carried out. The former produces a pair distribution function (PDF) of the averaged structure. The latter produces a PDF of the structure around the Ga atoms in the form of a differential (d-) PDF. The grazing incidence angle was set between 0.4 and 0.5°, which was sufficient to remove substrate scattering. The incidence X-ray beam size was 0.1×8 mm^2. The beam intensity was monitored by an ion chamber. A Huber four-circle diffractometer was used

to ensure proper sample alignment. The same Vortex-ME4 detector was used on the 2θ arm to increase data collection efficiency since the amorphous state scatters weakly. This is crucial, in particular, for the A-GIWAXS measurement around a dopant edge, say, 10 at% doping for which statistics of < 0.1% are desired. A double-slit system, with a pair of detecting elements behind each slit, was used to define two separate 2θ scattering angles. A second double-slit system was placed halfway between the detectors and the sample and used as guard slits to remove stray scattering. Air scattering was minimized by using evacuated flight paths for both the incident and scattered beams. Both scattering (inelastic + elastic) and Ga K_α fluorescence emission intensities were collected, simultaneously. The latter were used to remove the distortion due to the GI geometry.

At 15.00 keV, the GIWAXS data were measured up to q = 15 $Å^{-1}$. For the A-GIWAXS the q-range was limited by the absorption edge energy to ~10.4 $Å^{-1}$. The A-GIWAXS technique takes advantage of the significant change in the atomic scattering factor:

$$f(q, E) = f_0(q) - f'(E) + if''(E) \tag{4.2}$$

Around the absorption edge of an element of interest, i.e., Ga in the present work.[59] Two scattering measurements are needed at different photon energies, one is 100 eV below the Ga K absorption edge (10367 eV) and the other is 2 eV below the edge. The difference of these two

measurements yields a difference-pair distribution function (d-PDF) that describes the structure around Ga. Therefore, the A-GIWAXS provides element-specific local structure, similar to XAS.

4.3.4 Data reduction

For XAS, the data analysis and extended X-ray absorption fine structure (EXAFS) fitting were done using the iXAFS package.[60] Several photoelectron wavenumber, k, ranges were explored to test the persistence of the results. Fittings of the first shell structure were carried out in real space in the R-range of 1.0 – 2.3 Å and 1.0-2.4 Å for the Ga and In K-edges, respectively. Data in the k-range of 2.59-13.31 $Å^{-1}$ for the Ga K-edge and in the k-range of 2.29 -12.43 $Å^{-1}$ for the In K-edge, were used. The amplitude reduction factors, $S0^2$, of 0.98 for the Ga K-edge and 1.04 for the In K-edge were determined from fits of the two crystalline reference samples (In_2O_3 and Ga_2O_3).

For GIWAXS, the measured scattering intensities, I_m, were scaled (using scaling factor B) to the atomic scattering intensity, f^2, in electron units:

$$I_m \times B = (f^2 + I_{ine}) \tag{4.3}$$

Using the so-called high-angle method[61] -- the region where scattering modulations are vanishing. From here, the structure factor, $S(q)$, or interference function was obtained:

$$S(q) - 1 = [\, I_e - \{(f^2) + I_{ine}\}] / (f)^2 \tag{4.4}$$

Whose Fourier transform yields the PDF. I_e and I_{ine} are the elastic and inelastic intensities, respectively. Both f_0 and I_{ine} were obtained using tabulated values[62-63] while $f'(E)$ was obtained by performing the Kramers-Kronig inversion of $f''(E)$, which was measured on the a-IGO film through the absorption channel. For A-GIWAXS, the data processing procedure is similar, except that the K_β emission intensity is removed from the measured scattered intensity, since it is unresolved when the measuring energies are close to the absorption edge. After that it is straight forward to obtain a differential structure factor, d-$S(q)$, the Fourier transform of which yields the d-PDF, which is the probability of finding an atom at distance R from a Ga atom.

4.3.5 Theoretical methods

The amorphous oxide structures were generated by Prof. Julia Medvedeva using first-principles molecular-dynamics (MD) liquid-quench simulations as implemented in the Vienna Ab-Initio Simulation Package (VASP).[64-67] The calculations are based on the density functional theory (DFT)[68-69] with periodic boundary conditions and employ the PBE functional[70-71] within the projector augmented-wave method.[72-73] A bixbyite cell of In_2O_3 with crystalline density of 7.12 g/cm^3 and with 134 atoms per cell was used as initial structure which was melted at 3000 K to eliminate any crystalline memory. For Ga-doped indium oxide, random In atoms were substituted with a specific fraction of Ga (11%, 19% or 41%) and the cell density was adjusted

prior to additional melting at 3000 K for 10 ps to randomize the multicomponent configuration. To model non-stoichiometric structures, oxygen atom(s) were randomly removed from the melt prior to additional melting. Next, liquid quench simulations were performed as follows. Each structure was cooled to 1700 K at the MD rate of 100 K/ps and then rapidly quenched to 100 K at 200 K/ps rate. An energy cut-off of 260 eV and single Γ point were used during melting and quenching processes. Finally, each structure was equilibrated at 300 K for 10 ps with a cut-off energy of 400 eV. All MD simulations were carried out in the NVT ensemble with the Nose-Hoover thermostat using an integration time step of 2 fs.

To compare the structural characteristics of the theoretically modeled amorphous oxides to those observed experimentally, room-temperature In-Ga-O structures were used. For an accurate structural analysis of the theoretically modeled amorphous oxides, the average pair correlation function and the average effective coordination number were calculated according to refs.[74-76] The resulting atomic structures were plotted using VESTA software.[77]

Next, the atomic configurations obtained from the *ab-initio* MD simulations were optimized at 0 K using the PBE functional. For the optimization, the cut-off energy of 500 eV and the 4x4x4 Γ-centered k-point mesh were used; the atomic positions were relaxed until the Hellmann-Feynman force on each atom was below 0.01 eV/Å. The electronic and optical

properties of the optimized amorphous In-based oxides were calculated using the hybrid Heyd-Scuseria-Ernzerhof (HSE06) approach[78-79] with a mixing parameter of 0.25 and a screening parameter μ of 0.2 $Å^{-1}$. To characterize the localization of the electronic states within the band gap and near the band edges, the inverse participation ratio (IPR) was calculated. Optical absorption was derived from the frequency-dependent dielectric function:

$$\varepsilon(\omega) = \varepsilon_1(\omega) + i\,\varepsilon_2(\omega) \tag{4.5}$$

Calculated within independent particle approximation as implemented in VASP. The imaginary part, $\varepsilon_2(\omega)$, is related to the optical absorption at a given frequency, ω, and is determined based on the electronic transitions of the hybrid functional solution. The real part of the complex dielectric function is obtained using Kramers-Kronig relations.

4.3 Results and Discussion

In the present study, measurements of T_{cryst} were performed for a series of a-IGO films with varying levels of Ga substitution. The T_{cryst} of a-IO is found to be 125°C (Fig. 4.2A), which agrees well with previously published results.[37] With 8 at% Ga substitution (IGO8), the T_{cryst} rises to 250°C. The maximum measured T_{cryst} is 425°C for 51 at% Ga (IGO51), with the trend of increasing T_{cryst} with increasing Ga substitution clearly established. All films crystallize in the

cubic-Ia$\bar{3}$ bixbyite phase, labeled c-In_2O_3 (Fig. 4.1). No secondary phases, such as β-Ga_2O_3, are evidenced in the final diffraction patterns. The lattice constants (Fig. 4.2B) of the crystalline phases decrease linearly, in accord with Vegard's law, further suggesting that Ga is fully incorporated in the In-O matrix and does not phase-separate. The present lattice contraction, observed experimentally in this work, is in a good agreement with previous single-phase simulations of crystalline (c-) IGO films.[80]

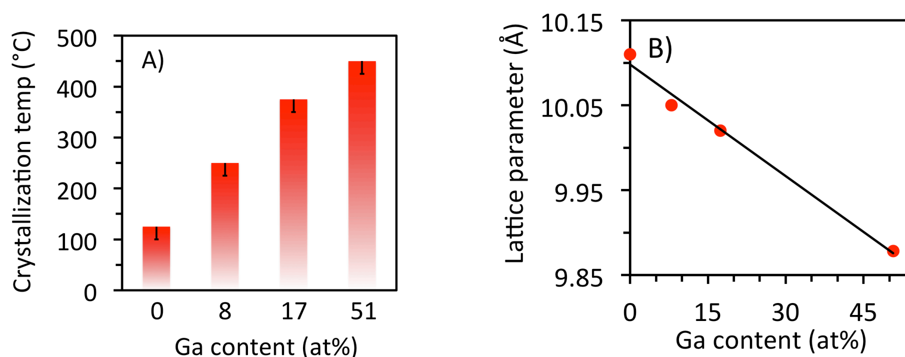

Figure 4.2. A) Crystallization temperature as a function of at% Ga substitution determined through 1 hour anneal/quench/GIXRD cycles spaced 25°C apart. Error bars represent the 25°C window of uncertainty between pre- and post- crystallization runs. B) GIXRD determined lattice constant of the bixbyite unit cell for fully crystallized IGO samples as a function of Ga substitution. The solid line is a linear least-squares fit to the four data points. Error bars are smaller than the data points.

The lack of secondary phases in the present crystalline IGO films is surprising from a thermodynamics perspective. In the In_2O_3-Ga_2O_3 phase diagram the solubility of Ga in the bixbyite phase is only 5 at% at 1000 °C. This bulk phase diagram suggests that given enough

heat and time, the present films would devolve into two-phase structures. The absence of β-Ga_2O_3 in our high Ga-content (> 5 at%) films highlights the difference between amorphous oxide thin films and bulk oxides. Clearly the amorphous films are only kinetically stable, not thermodynamically stable.

4.3.1 Experimental structure

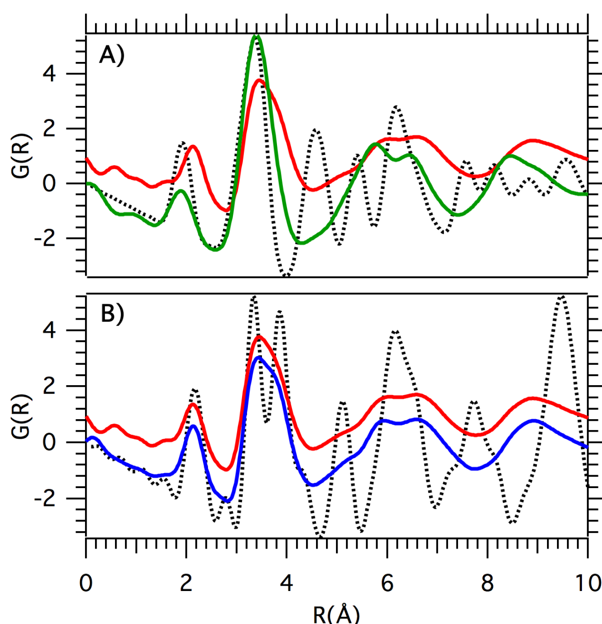

Figure 4.3. A) PDF of a-IGO with 17 at% Ga (red). Difference PDF of the structure around Ga in a-IGO17 (green). Calculated PDF for β-Ga_2O_3 is shown for reference (black dotted line). B) Measured pair distribution function (PDF) for a-IGO with 8 at% Ga (blue) and 17 at% Ga (red). Calculated PDF for bixbyite In_2O_3 is shown for reference (black dotted). The first and second peaks are produced by M-O and M··M distances, respectively. The first peak is weaker because O is a weak scatterer.

Anomalous X-ray scattering measurements (A-GIWAXS) also reveal the absence of phase

separation in the IGO amorphous state (Fig. 4.3A, green). From the difference pair distribution function (d-PDF)[59] we see the structure around Ga does not correspond to that of β-Ga_2O_3 (Fig. 4.3A, black). The position of the second shell peak is considerably larger than the Ga··Ga distance found in β-Ga_2O_3 (Fig. 4.3A, black). In addition, the number and shape of the density fluctuations around Ga bear great similarity to those of the X-ray scattering derived PDF for the averaged structure (Fig. 4.3A, red). These consistencies between the PDF and d-PDF results argue that a homogeneous distribution of Ga ions is achieved by the PLD growth technique. These distributed Ga ions increase the overall structural disorder of the system. A comparison of the PDF of IGO8 (blue) and IGO17 (red) (Fig. 4.3B) shows that as the Ga content increases from 8 at% to 17 at% there is a broadening of the PDF features, indicative of increased disorder. This disorder affects M··M distances and beyond.

EXAFS analyses of the present a-IGO samples were performed at both the Ga and In K-edges (Table 4.1). The fits reveal average coordination numbers (N) and bond distances (R). The local first shell structure of bixbyite (In_2O_3)[81] and β- gallia (Ga_2O_3)[82] derived from X-ray diffraction are presented as references. Crystalline In_2O_3 has a first shell (metal-oxygen, M-O) coordination number of 6. Crystalline β-gallia has two Ga-O coordination sites, half are N = 4 tetrahedral sites and the other half are N = 6 octahedral sites (Fig. 4.4). In a perfect crystal of

β-gallia, this results in an average N of 5.

In the present study, all a-IGO samples show significant under-coordination of both In and Ga, compared to their respective pure crystalline references (Table 1).

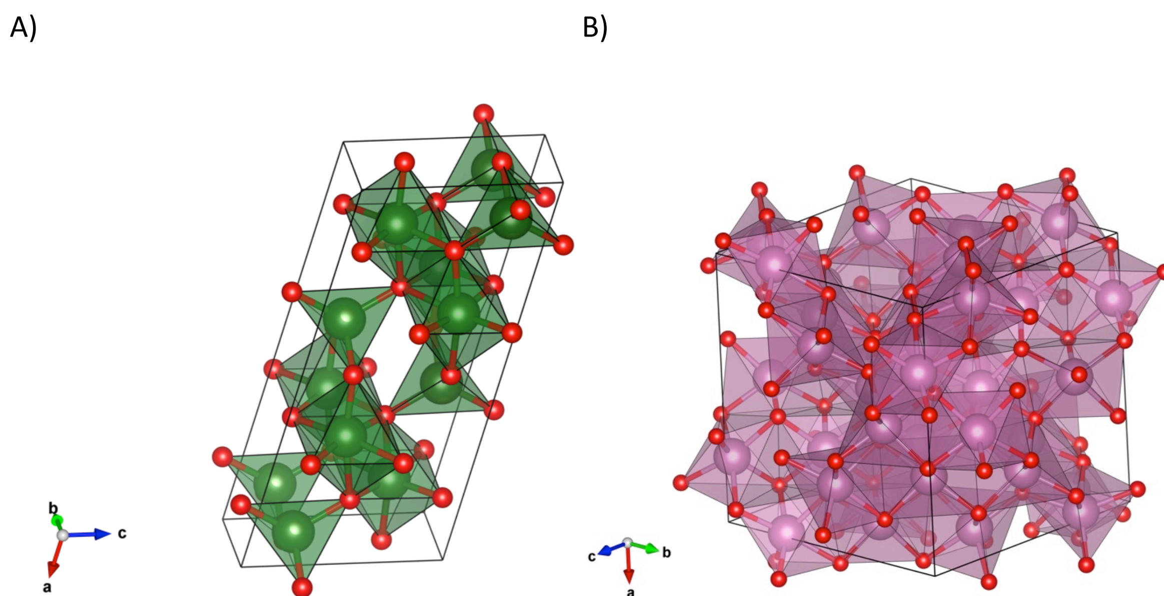

Figure 4.4. A) β-gallia Ga_2O_3 crystal structure.[10] *Ga atoms are green and O atoms are red. B) Bixbyite In_2O_3 crystal structure.*[1] *In atoms are purple and O atoms are red. Figures were drawn with the Vesta software package.*[11]

In addition, despite Ga being well dispersed in the In-O matrix, there is dissimilarity in the oxygen coordination around Ga versus In. In the amorphous films the oxygen coordination number around In is approximately 5 but around Ga it is much closer to 4. This trend is echoed in the fitting results of M-O bond distance. The average length of the Ga-O bond, 1.88 Å, is not unexpectedly far shorter than the average In-O bond length, 2.16 Å. Note that the present

EXAFS-derived 1.88 Å Ga-O bond length lies much closer to that for tetrahedral Ga (1.85 Å) than to that for octahedral Ga (2.01 Å). Assuming bond distance increases as average coordination number increases,[83] a 1.88 Å Ga-O bond distance suggests <20% of the Ga sites are 6-fold coordinate.

Table 4.1. First shell (metal-oxygen) EXAFS fitting results of experimental samples compared with room temperature MD simulations[a)]

	Samples	**N**	**R (Å)**	**Simulations**	**ECN**	**R (Å)**
Ga Local Structure	c-Ga_2O_3 (from XRD)	5 $\left(\frac{1}{2}4 + \frac{1}{2}\ 6\right)$	1.93 $\left(\frac{1}{2}1.85 + \frac{1}{2}\ 62.01\right)$			
	a-IGO8	4.25 ± 0.29	1.88 ± 0.014	a-IGO11	4.28	1.92
	a-IGO17	3.69 ± 0.28	1.90 ± 0.015	a-IGO19	4.38	1.93
	a-IGO51	4.14 ± 0.22	1.88 ± 0.011	a-IGO41	4.66	1.95
In Local Structure	c-In_2O_3 (from XRD)	6	2.17			
	a-IO	5.11 ± 0.53	2.16 ± 0.018	a-IO	5.30	2.17
	a-IGO8	5.26 ± 0.56	2.16 ± 0.023	a-IGO11	5.20	2.17
	a-IGO17	5.11 ± 0.53	2.16 ± 0.026	a-IGO19	5.13	2.17
	a-IGO51	4.76 ± 0.53	2.17 ± 0.026	a-IGO41	5.13	2.17

[a)]*N = coordination number, R = bond distance, ECN = effective coordination number.*

All of the a-IGO films studied here show a minority of 6-fold Ga sites. Note that Ga prefers the local coordination of its native oxide, β-Ga_2O_3 (a mixture of 4- and 6-fold coordination), over that of the amorphous indium oxide matrix, which clearly has a bixbyite-like structure at local- (Table 4.1) and medium-range distances (Fig. 4.3).

The X-ray scattering measurements in this study provide independent experimental confirmation of the EXAFS results in table 4.1. Figure 4.3B shows the PDFs obtained for two of the amorphous films, which are compared with the PDF calculated for the c-In_2O_3 reference. The first peak positions of the PDFs (Fig. 4.3B) are composed of the weighted sum of the Ga-O and the In-O bond distances. The downward shift of the first peak from 2.14 Å for IGO8 to 2.12 Å for IGO17 is consistent with the increasing quantity of short Ga-O bonds as the Ga content increases. Figure 4.3A compares the PDF of IGO17, the d- PDF of IGO17 (the structure surrounding Ga), and the reference PDF of c-Ga_2O_3. The comparison highlights the departure of the Ga first-shell structure from the first-shell structure of the surrounding In-O matrix. The A-GIWAXS d-PDF (Fig. 4.3A, green) demonstrates an average Ga-O bond length is 1.88 Å, in agreement with table 4.1. Thus, both the EXAFS and A-GIWAXS/GIWAXS results find a departure of the Ga first-shell structure from the first-shell structure of the In-O matrix: both support the presence of low Ga-O coordination.

The tendency to maintain lower coordination within a higher coordinated matrix may contribute to the increased thermal stability of a-IGO over that of a-IO. Increased thermal stability has been reported in systems with Zn substituting for In, such as in a-IZO or a-ZITO (amorphous zinc indium tin oxide),[34, 84-85] and systems with Zn substituting for Sn, a-ZTO (amorphous zinc tin oxide).[14]

Table 4.2. Comparison of first-shell (metal-oxygen) EXAFS fitting results of as-deposited (amorphous) versus annealed (crystallized) films, showing changes in coordination numbers and bond lengths[a)]

	Sample	**N**	**R (Å)**	**ΔN**	**ΔR (Å)**
Ga K-edge	As-dep IGO8	4.25 ± 0.29	1.88 ± 0.014	1.39	0.15
	Anneal IGO8	5.64 ± 0.48	2.03 ± 0.021		
	As-dep IGO51	4.14 ± 0.22	1.88 ± 0.011	1.16	0.13
	Anneal IGO51	5.30 ± 0.63	2.01 ± 0.028		
In K-edge	As-dep IGO8	5.26 ± 0.41	2.16 ± 0.023	0.53	0.01
	Anneal IGO8	5.79 ± 0.53	2.17 ± 0.020		
	As-dep IGO51	4.76 ± 0.56	2.17 ± 0.026	0.82	0.01
	Anneal IGO51	5.58 ± 0.53	2.18 ± 0.021		

[a)]N = metal-oxygen coordination number, R = bond distance. ΔN and ΔR = the difference in coordination and bond distance between as-deposited and air-annealed samples.

The capacity of both Ga and Zn to raise the T_{cryst} of amorphous oxides suggests that the presence of distinctly low- coordinated sites suppresses long-range order. Additionally, as a-IGO films crystallize, Ga transitions to a significantly higher average coordination number and the Ga-O distance increases (Table 4.2). This observation strongly suggests that 4- and 5-fold coordinated sites must transition to 6-fold coordinated sites for crystallization to occur. This transition is supported by the crystal structure of the crystalline films, bixbyite, which consists entirely of 6-fold coordinated metal sites (Fig. 4.4B). This increase in coordination number (ΔN), and the resultant increase in bond distance (ΔR) is far larger for Ga than for In. The increase in Ga coordination number upon crystallization is almost twice that of In. Additionally, the ΔR for the In-O bond distance is negligible, especially in comparison to the ΔR of the Ga-O bond. Thus, because of the capacity to maintain a unique local structure within a more highly coordinated matrix, Ga substitution creates a barrier to crystallization.

4.3.2 MD-simulated structure

The results of *ab-initio* MD simulations support our experimental observations and provide further insight into the effect of Ga substitution on the structural properties of amorphous IGO. Specifically, in excellent agreement with our EXAFS results, table 4.1, an analysis of the calculated first-shell structural characteristics shows, (i) the average In-O distance remains the

same in all three a-IGO structures, 2.17 Å; and (ii) the average In-O coordination decreases slightly with increasing Ga content: 5.30, 5.20, 5.13, and 5.13 for amorphous $In_2O_{2.96}$ (IO), $In_{1.78}Ga_{0.22}O_{2.96}$ (IGO11), $In_{1.63}Ga_{0.37}O_{2.96}$ (IGO19), and $In_{1.19}Ga_{0.81}O_{2.96}$ (IGO41), respectively. The calculated distribution of In-O coordination numbers (Fig. 4.5A) reveals that the presence of Ga suppresses the population of In atoms coordinated by 6 oxygen, i.e., those with the effective coordination number ECN = 5.7-6.0; whereas the number of under-coordinated In atoms (ECN = 4.0-5.0) increases with the Ga content. In agreement with the Ga K-edge EXAFS measurements, the Ga atoms in amorphous IGO are primarily four-fold-coordinated: the calculated average Ga-O coordination is 4.28, 4.38, and 4.66 for Ga substitutions of 11 at%, 19 at%, and 41 at%, respectively. The calculated distributions of Ga-O coordination (Fig. 4.5B) suggest that with increasing Ga fraction, Ga atoms coordinated to 5 oxygen atoms (ECN = 4.5-5.0) begin to prevail, while Ga atoms coordinated with 6 oxygen atoms remain negligible. Accordingly, the Ga-O distances increase slightly, from 1.92 Å to 1.93 Å and to 1.95 Å for 11 at%, 19 at%, and 41 at% of Ga, respectively. These values are in agreement with the average Ga-O distance in β-gallia, 1.93 Å (Table 4.1), again showing that, in the amorphous phase, Ga prefers the local oxygen environment of pure Ga_2O_3 to that of the In-O matrix.

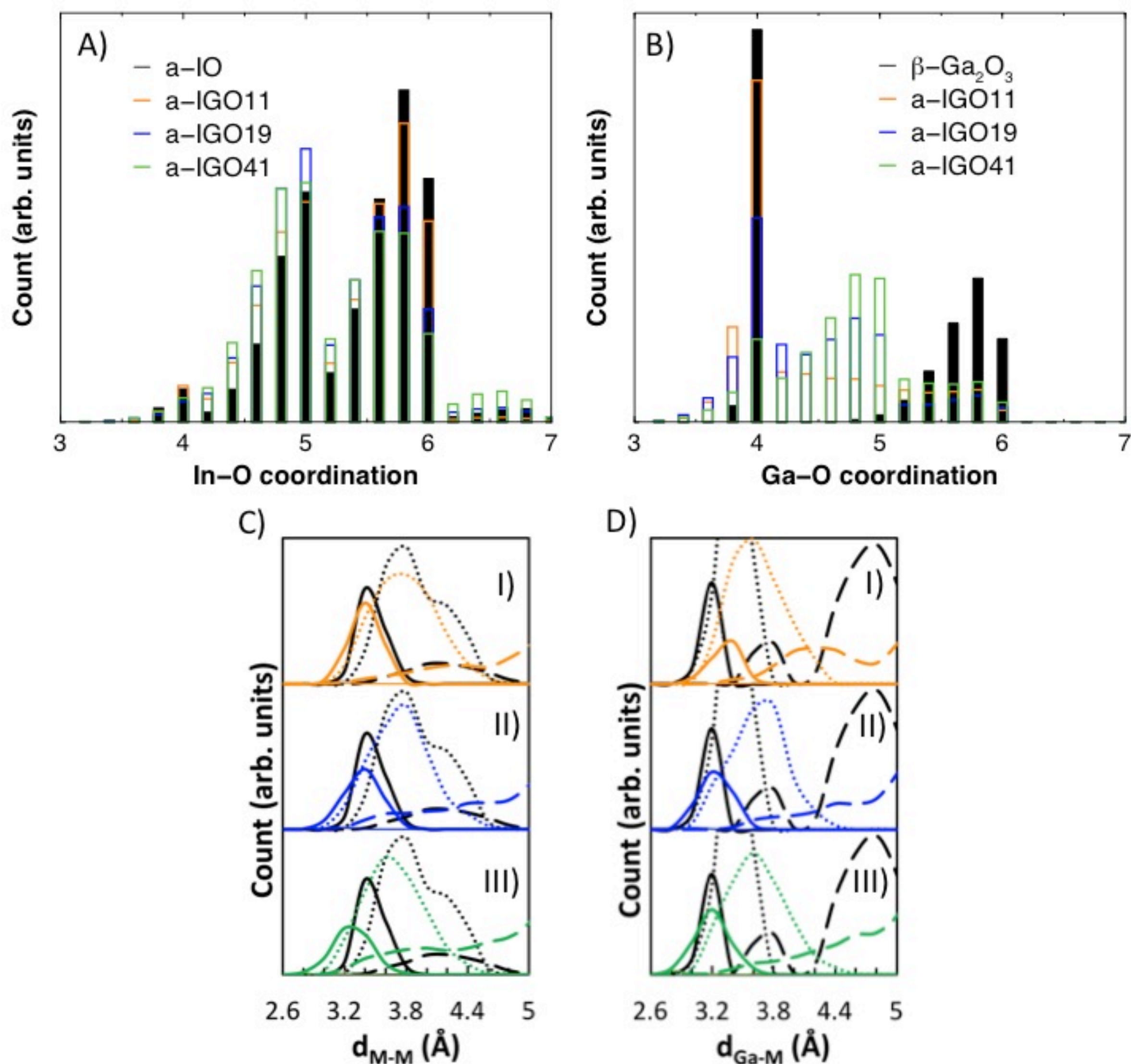

Figure 4.5. Distribution of calculated ECN values in a-IO and three a-IGO compositions as obtained from room termperature MD simulations for In-O, A) and Ga-O, B). Spread of polyhedra edge-shared (solid line), corner-shared (dotted line), and lack of sharing (dashed line), C) M··M distances and D) Ga··M distances shown for I) a-IGO11 (orange), II) a-IGO19 (blue), and III) a-IGO41 (green). Black lines show the sharing distributions for a-IO in C) and for β-Ga_2O_3 in D).

Note that the effect of Ga on the local structure opposes the formation of nanocrystallites, composed of all M-O octahedra, observed at the onset of crystallization; the

Ga-O octahedral population remains negligible while the In-O octahedra decrease in response to the Ga substitution.[15, 52]

Evolution to 6-coordinate Ga may in principal impede crystallization for thermodynamic and/or kinetic reasons. A thermodynamic argument can be made using the In_2O_3-Ga_2O_3 phase diagram[86] in which bulk $In_{2-x}Ga_xO_3$ has very limited solubility at the bixbyite/In_2O_3 side of the phase diagram,[86] with only 5 at% Ga known to incorporate into bixbyite In_2O_3 before reaching the phase boundary, i.e., the solubility limit. Thus, having a large fraction of the Ga sites in a-IGO 6-fold coordinated is thermodynamically unfavorable. A kinetic argument can also be made by suggesting that there may be an activation barrier to the transition of Ga-O tetrahedra to octahedra. This transition, from tetrahedral coordination to octahedral coordination could arise from an uptake of oxygen in the film. After all, these films were grown in a vacuum chamber at an oxygen pressure of 7.5 mTorr and are annealed in ambient air to induce crystallization. However, work by Buchholz *et al*.[15] (especially figures 7 and 8) demonstrates how an amorphous structure can undergo polyhedral rotations to decrease the M-O coordination number without removing any oxygen atoms from the system. Evidence for rotated polyhedra in our amorphous samples can be seen by comparing the a-IGO PDFs to the c-In_2O_3 reference PDF (Fig. 4.3B). The differentiation of edge and corner sharing polyhedra disappears and instead there is

continuous density between the edge-connected distance and the corner-connected distance. Rotated polyhedral would provide this smearing out of corner-shared vs. edge-shared distinction. In addition, Buchholz[15] suggests that M-M bonding should be under-coordination. Fits of the M-M In K-edge peak (Table 4.3) show significant under-coordination of M-M bonding.

Table 4.3. A-IGO second shell EXAFS fitting results of In K-edge (metal-metal)[a)]

	Samples	N	R (Å)	σ^2 (Å^2)	R^2
In K-edge	a-IO	2.73	3.37	1.52E-2	2.32E-3
	a-IGO8	2.52	3.39	1.51E-2	1.15E-2
	a-IGO17	2.82	3.34	1.72E-2	9.26E-3
	a-IGO51	3.03	3.40	1.68E-2	1.38E-3

[a)] N is coordination number. R is bond distance. σ^2 is a measure of the thermal and structural disorder.

Additionally, the multi-coordinate nature of Ga cations renders the Ga-O coordination geometry more sensitive to the O stoichiometry than does In-O coordination. From additional MD simulations of the amorphous oxide with lower O stoichiometry, $In_{1.19}Ga_{0.81}O_{2.92}$ (Fig. 4.6), it is found that the Ga-O coordination is reduced to 4.45, whereas the In-O coordination decreases only slightly, to 5.09 – as compared to ECN(Ga-O)= 4.66 and ECN(In-O)= 5.13 in $In_{1.19}Ga_{0.81}O_{2.96}$. A closer look at the distribution of the coordination numbers (Fig. 4.6) suggests that the number of four-coordinate Ga atoms nearly doubles upon oxygen reduction, whereas

the number of both low-coordinate (ECN<4.0) and high-coordinate (ECN>5.5) In atoms increases making the average ECN value unchanged. These results are in accord with the observed higher sensitivity of the Ga-O coordination to annealing (Table 4.2) – the additional energy from heating the samples may promote O diffusion and enable long-range structural reconstruction; both factors facilitate the higher coordination of Ga. Clearly, additional energy is required for IGO vs. IO crystallization because the system must dramatically increase M-O coordination to form the bixbyite phase.

Moreover, in accord with the observed trend in IGO crystallization temperature (Fig. 4.2A), the calculated distortions in the In-O polyhedra become more pronounced with increasing Ga fraction: the average variance of the first-shell In-O distances is 8.42×10^{-3} Å^2, 9.55×10^{-3} Å^2, 10.74×10^{-3} Å^2, and 11.64×10^{-3} Å^2 for amorphous IO, IGO11, IGO19, and IGO41, respectively. The Ga-O polyhedra are also strongly distorted with the average variance for the Ga-O distances of, 1.40×10^{-2} Å^2, 1.89×10^{-2} Å^2, and 1.66×10^{-2} Å^2 for IGO11, IGO19, and IGO41, respectively, being larger than those for the corresponding In-O distances reported above. This result may at first appear counterintuitive given the fact that the Ga-O bonding is stronger than the In-O bonding.

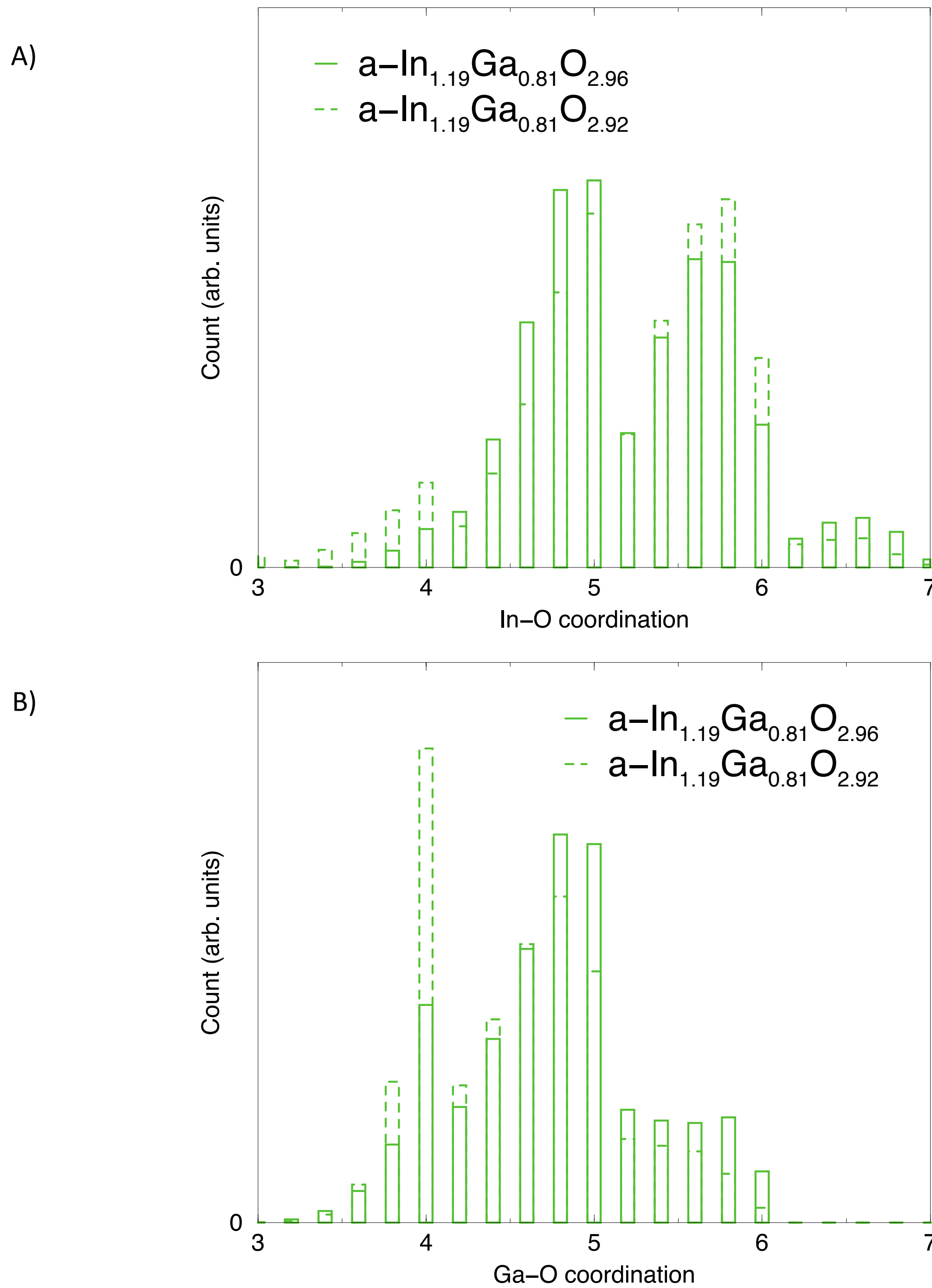

Figure 4.6. Distribution of calculated ECN in a-IGO41 with variable oxygen content as obtained at room temperature MD simulations for A) In-O and B) Ga-O.

However, we believe that the strong local distortions in Ga-O polyhedra stem from their intrinsic multi-coordinate nature (4 and 6-coordinate in monoclinic β-Ga_2O_3); in addition, the weaker metal–O bonding of the host In atoms facilitates the coordinative transformations for Ga. Thus, the presence of Ga increases disorder in the M-O bonding and moves the system farther away from an ordered crystalline lattice.

Medium-range structural characteristics, i.e., how the M-O polyhedra combine to form a network, plays a crucial role in amorphization.[15] Connectivity or O sharing between the M-O polyhedra having different coordination patterns and degrees of distortion, determines their spatial distribution and, hence, governs the structural reorganization, crystallization, and phase formation phenomena. In bixbyite In_2O_3, the second and third shells of In are associated with 6 In neighbors at 3.3 Å that share two O atoms with the central In atom (i.e., the corresponding polyhedra are edge-shared) and 6 In neighbors at 3.8 Å that share one oxygen atom (corner-shared polyhedra). In the amorphous phase, a significant amount of edge-shared connections become corner-shared, figure 4.5C: out of the total number of all In-In pairs that share 1, 2, or 3 O atoms, as many as 80% share only a single O atom.[14, 87] As a result, the distance distribution for the corner-sharing connections in undoped a-IO is nearly twice as wide as that in crystalline In_2O_3, overlapping significantly with the distance distribution for the

edge-shared In··In pairs (Fig. 4.5C). In a-IGO, both the edge- and corner-shared distributions shift toward shorter metal-metal (M··M) distances in agreement with the small ionic size of Ga. Significantly, addition of Ga broadens the edge-sharing distribution so that it overlaps completely with the corner-sharing distribution for the Ga fraction of 19% and above (Fig. 4.5D). Experimentally, the second and third shells cannot be distinguished in this case but, the comparatively shorter Ga··M distances, as compared to M··M distances, can be seen in the comparison of the PDF and d-PDF (Fig. 4.3A). Thus, the stronger local distortions caused by the capacity of Ga cations to assume different O environments than the surrounding In-O matrix and the higher medium-range disorder in a-IGOs with increased Ga content, contribute to the observed increase in the crystallization temperature in these oxides.

Besides the changes in structure that must occur upon crystallization, significant strain may be also be induced upon crystallization. Figure 4.2B of the manuscript demonstrates the lattice contraction that Ga substitution produces. In addition, comparison of the d-PDF (Fig. 4.3A) with the PDF of IGO17 also suggests that there is a strain field that exists around the Ga atoms out to ~10Å. Though the density modulations in the d-PDF roughly match the PDF, all peaks appear at slightly shorter distances. Given the small cation size of Ga, we suggest that the strain created by Ga in the crystalline bixbyite structure would be even further exacerbated and

thus provide a barrier to crystallization.

4.4 Conclusion

A systematic investigation of the thermal and structural properties of a series of amorphous Ga-substituted In-O thin films was performed. Strong agreement between experimental structure results and theoretical simulations are demonstrated. The results of the *ex situ* crystallization study reveal that the thermal instability of a-IO can be overcome by Ga addition. The mechanism underlying this effect is identified as the tendency of Ga to maintain the lower coordination, seen in pure Ga-O, even when surrounded by a more highly coordinated In-O matrix. While the coordination and bonding of pure a-IO is fairly close to that of crystalline bixbyite, Ga must undergo significant changes in coordination and bonding before crystallization occurs. This understanding suggests that when choosing a substitutional cation, the crystal structure of its native oxide may inform how the local structure of the cation will behave when it is used as an amorphous cation modifier. Furthermore, it suggests that substitutional cations with a “native coordination” dissimilar to that of the amorphous matrix, may be most effective in increasing thermal stability.

CHAPTER 5: **The Role of Ga in the Electrical Properties of a-IGO**

The a-TCO system, amorphous indium gallium oxide (a-IGO), is a model system for developing structure-property relationships to investigate the influence of substitutional cations on the electrical performance of amorphous oxides. Gallium is known to decrease conductivity when added to indium-based amorphous oxides. Hall measurements reveal the initial sharp drop in conductivity upon Ga substitution is due to a decrease in both carrier concentration and mobility. At >20 at% Ga content, the influence of Ga on the carrier concentration and mobility begins to lessen. The decline in both the carrier concentration and mobility with increasing Ga is attributed to dilution of the charge-carrying In-O matrix and to increased structural disorder. The latter effect saturates at high at% Ga, explaining the diminished effect of Ga at high substitution.

5.1 Introduction

The discovery of high carrier mobility in amorphous In-Ga-Zn-O (a-IGZO)[88] films grown at room temperature stimulated intense academic and industrial research efforts aimed at exploring a-IGZO as a channel layer material for thin film transistors (TFTs).[2, 5-6, 11] The isotropic conduction orbitals of a-IGZO provide a marked charge transport advantage over the heretofore most common low-temperature semiconductor, amorphous (a-) Si. This advantage is rooted in the resilient s-state conduction manifold of a-IGZO; mobility is only minimally degraded by the bond disorder of the amorphous state. In contrast, a 2-3 order-of-magnitude decline in mobility occurs upon the transition from crystalline Si to a-Si.[1-2, 4]

The a-TCO system of indium gallium oxide (a-IGO) is a model system for developing structure-property relationships to investigate the influence of substitutional cations on the performance of a-TCOs. We will present a systematic study of the evolution of electrical properties, as a function of gallium content, in a series of a-IGO thin films. These property studies were understood on a fundamental level by pairing them with local structural studies, X-ray absorption spectroscopy (XAS) and anomalous X-ray scattering (AXS). Although amorphous oxides lack long-range order, previous studies have established the persistence of local-scale order,[15, 40, 52, 89] and the use of element-specific local structure techniques, specifically

X-ray absorption spectroscopy and X-ray scattering, have proven to be incisive tools for understanding the structures of amorphous materials.[39, 90] The present investigation successfully couples these X-ray techniques with *ab-initio* molecular dynamics simulations. The close agreement achieved between theory and experiment provides a comprehensive understanding of the a-IGO structure, which in turn provides an unprecedented description of how Ga influences the structure-property relationships at play in a-IGO.

The channel layer of a TFT requires a semiconductor with low carrier density, so that control of carrier concentration is imperative. There is a growing consensus that the predominant point defect species responsible for carrier generation in a-TCOs are doubly-charged oxygen vacancies.[10, 17, 26, 91-92] Thus, experimental studies a-IZO[26, 92] and a-IGZO[17] have shown that in both cases the d(log conductivity)/d(log pO_2) slope is observed to be -1/6, which is consistent with doubly-charged oxygen vacancies as the carrier generating species. The modifying role of Ga is typically defined in reference to the reduction of free carriers due to its strong oxygen binding affinity.[10, 91, 93-95] Here, using theoretical modeling, we probe deeper to show that the true role of Ga in carrier production is two-fold: 1) Ga decreases carrier density because the Ga-O polyhedra do not contribute to carrier generation, and 2) Ga cations impede the clustering of under-coordinated In-O polyhedra, the source of free carriers.

Several different models have been proposed to simulate the nature of carrier mobility in amorphous oxide films.[96-101] The challenge is that those factors which limit mobility can vary with growth conditions, such as temperature,[40] which affect film quality.[88, 101-102] As this work emphasizes, film quality and TFT performance are tied to the structure of the film. Here we use the well-developed experimental and theoretical understanding of structure to discuss the nature of conduction and the role of Ga in the mobility of a-IGO. The agreement between experimental results and our model structure provides confidence in the electronic calculations. We show that Ga increases percolation barriers and trap states, as well as increases the range of hopping centers, which negatively affect both band conduction and variable range carrier hopping in the system.

5.2 Methods

A series of a-IGO thin films was grown by pulsed laser deposition (PLD) in collaboration with Dr. Bruce Buchholz of the Chang group. The structures of the a-IGO films were studied using X-ray absorption spectroscopy (XAS) and X-ray scattering techniques. Simulations of amorphous oxide structures were generated by Prof. Julia Medvedeva using first-principles molecular-dynamics (MD) liquid-quench simulations. Calculations are based on the density

functional theory (DFT)[68-69] with periodic boundary conditions and employ the PBE functional[70-71] within the projector augmented-wave method.[72-73] For details on film growth, X-ray absorption spectroscopy (XAS), X-ray scattering, and theoretical methods please see chapter 4.

The carrier concentration, carrier mobility, and conductivity of the a-IGO films were measured at room temperature using an Ecopia HMS-3000 Hall measurement system. Gold spring contacts were used in 4-point Van der Pauw configuration. A 0.58 T field was applied using a permanent magnet. I-V curves were collected before each Hall measurement to ensure that Ohmic contact was achieved.

5.3 Results and Discussion

To investigate the influence of Ga substitution on the electrical properties of the present PLD-deposited a-IGO films, a systematic Hall effect study as a function of Ga content was carried out at room temperature, and the results are shown in figure 5.1A. Note that the growth conditions of all films represented in Figure 4 were identical. The ~75% fall electrical conductivity is consistent with the relatively modest decline in carrier content (~25%) and the drop in carrier mobility of ca. 50%. All three properties approach constancy beyond a Ga content

of 18 at%.

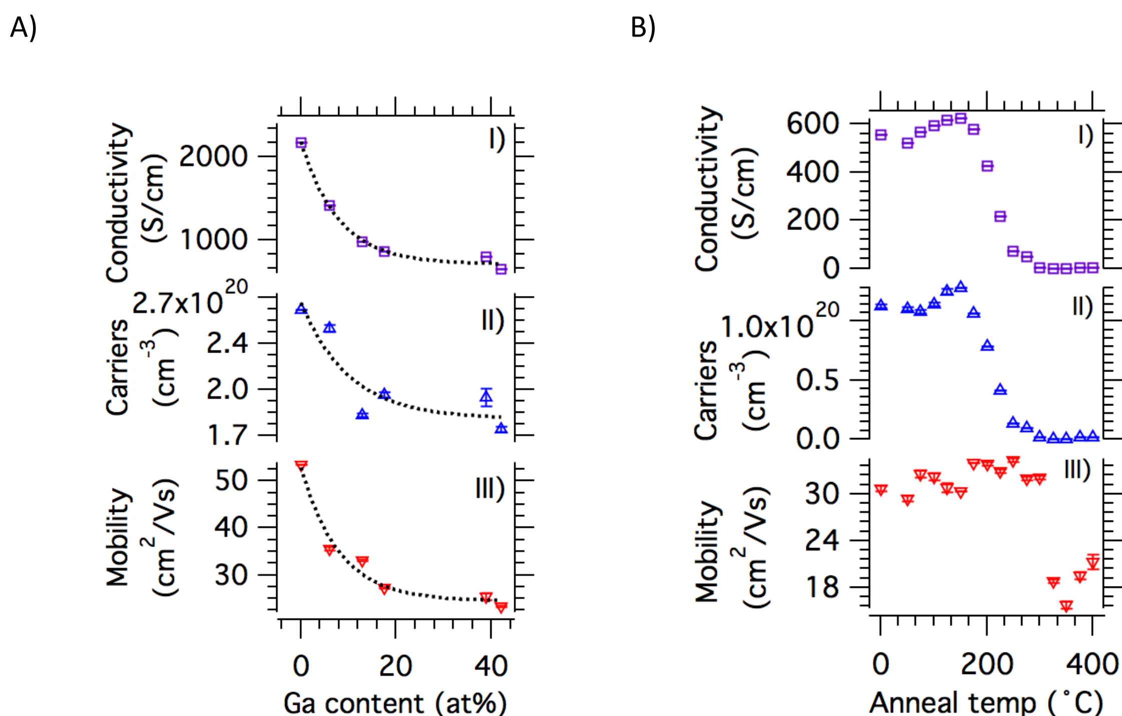

Figure 5.1. A) Hall effect data for a series of a-IGO thin films as a function of at% Ga. Error bars represent the standard deviation between three samples of the same composition, grown under the same conditions. The error bars are the size of the data points for conductivity and mobility. Dashed lines represent exponential fits of the data and are provided as visual guides for the observed trends. B) Room temperature Hall effect data on IGO51 (blue), as a function of annealing temperature. As-deposited results are plotted at -25°C. The sample was cycled through air annealing (at increasing temperatures), quench, and room temperature Hall measurements. Error bars are calculated as the standard deviation of 10 consecutive measurements and are smaller than the data points in most cases.

5.3.1 Carrier generation: experimental

The change in the n-type carrier content upon Ga substitution is less than one order of magnitude, indicating that Ga is not a major source of carriers. At 10 at% doping and beyond, the Ga concentration is ~$10^{22}/cm^3$, two orders of magnitude greater than the measured carrier density. Additionally, The In K-edge XANES data for the a-IO and the three a-IGO films display good agreement with the c-In_2O_3 reference, bixbyite (Fig. 6.2A), supporting the conclusion that In remains in the 3^+ state. There is no visible change in the In K-edge in response to the 3 levels of Ga substitution. The Ga K-edge spectra for the 3 a-IGO samples have slightly more variation between them than the In K-edge. The agreement of the near-edge structure is less persuasive than the agreement seen at the In K-edge (Fig. 6.2B). However, comparison with Ga K-edge data from other compounds α-Ga_2O_3 (GaO_6)[103] and $GaPO_4$ (GaO_4)[103] confirms that β-Ga_2O_3 is the best reference. We can conclude that Ga also has a 3^+ charge. Thus, Ga is isovalent with In and produces neutral "defects" that do not affect the electroneutrality condition.

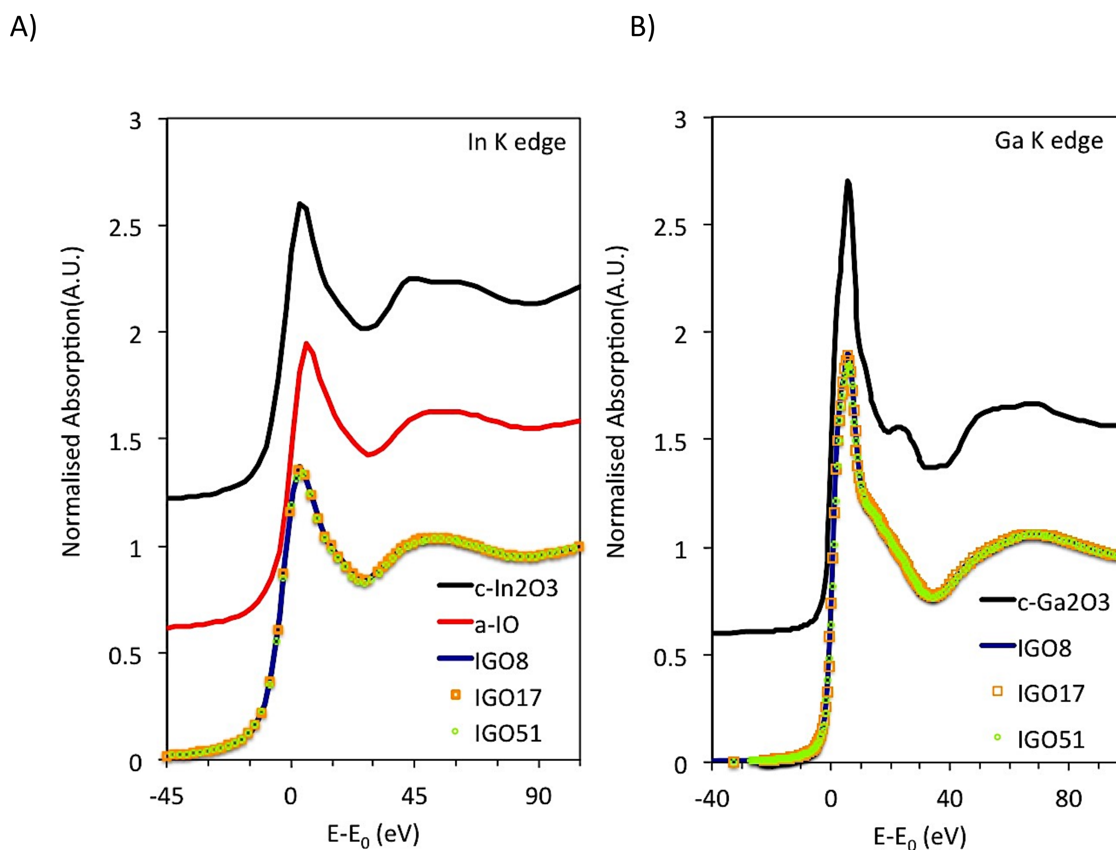

Figure 5.2. A) The In K-edge XANES data for the crystalline (c-) In_2O_3 reference (bixbyite), amorphous (a-) IO, and the three a-IGO films. B) The Ga K-edge spectra for the c-Ga_2O_3 (beta gallia) reference and the 3 a-IGO samples.

Next, a 51 at% Ga-substituted film (IGO51) was annealed for 1 hour at progressively higher temperatures, quenched to room temperature at each point, and characterized by Hall effect measurements. Note that above 150°C there is a rapid fall in carrier content to a level 1-2 orders of magnitude below that of the as-deposited film. Note also that the crystallization temperature for this film is approximately 450°C (see chapter 4, Fig. 4.2A). Therefore, the decline in carrier content between 150°C and 250°C is not associated with crystallization. Instead, we interpret this

behavior as the onset of O exchange/equilibration of defects, similar to the equilibration of O vacancies seen in defect studies of a-IZO[26, 92] and a-IGZO,[27] Oxygen tracer diffusion measurements show that O exchange and diffusion can take place at 200°C in a-IGZO films;[27] theoretical calculations have also shown that vacancies can be neutralized at 200°C in a-IGZO.[104]

5.3.2 Carrier generation: MD simulations and DFT calculations

As discussed in section 5.3.1 above, Ga does not serve as a carrier donor in amorphous In-Ga-O. This is supported by the present DFT calculations for *stoichiometric* amorphous In-Ga-O oxides; independent of the level of fractional Ga substitution, the electronic band structure of a-IGO corresponds to an insulator, *i.e.*, the conduction band is empty. Furthermore, it can be argued that the carrier-producing entities in a-IGO films are only the In-O polyhedra. As discussed in chapter 4, all Ga atoms satisfy their natural coordination with O atoms – in marked contrast to In atoms, the large fraction of which are under-coordinated, ECN < 5.0, figure 4.5A and table 4.1. The assertion that only In-O polyhedra contribute to carrier production is consistent with the observed behavior of the end-member films in the a-IGO series; a-IO is highly conductive (see Figure 5.1A), whereas a-Ga-O is known to be highly resistive, *i.e.*, having immeasurably small carrier densities.[105] Note that, although the under-coordination of In-O polyhedra suggests a role in carrier production, there is not a direct correlation between under-coordination and carrier

concentration. Indeed, if each instance of under-coordination was the site of a charged O vacancy, the carrier concentration would exceed the experimental values by 2 orders-of-magnitude.

Accurate DFT calculations on *non-stoichiometric* a-IO and a-IGO, with the same O stoichiometry of 2.96 for each structure, provide additional insight into the carrier generation mechanism in these materials. It is found that low coordination of In is a necessary but not a sufficient condition to form a donor defect. The charge density distribution (Fig. 5.3) calculated for the partially occupied conduction band in a-IO and a-IGO, reveals that a notable charge density accumulates in the interstitial region between two or three In neighbors that not only have low coordination (ECN = 4.4-5.0 for all four compositions considered), but are also under-shared, i.e., lack an O atom to form a connection that is expected based on the distance between the corresponding In atoms. In a-IO and in three a-IGO structures with variable Ga content, low-coordinate In polyhedral pairs are separated by a short distance of 3.1-3.5 Å and are corner-shared, missing the additional O atom expected at this separation. Hence, despite the large fraction of low-coordinate In atoms (chapter 4, Fig. 4.5A), only under-shared In atoms located at short distances show charge accumulation. Structurally, the pair of under-shared, under-coordinated In atoms resembles an O vacancy defect in a crystalline oxide. The difference

between what is observed as an O vacancy in crystalline materials and what is observed in our a-IGO models is seen in the range of structural rearrangement that accompanies the O defect.

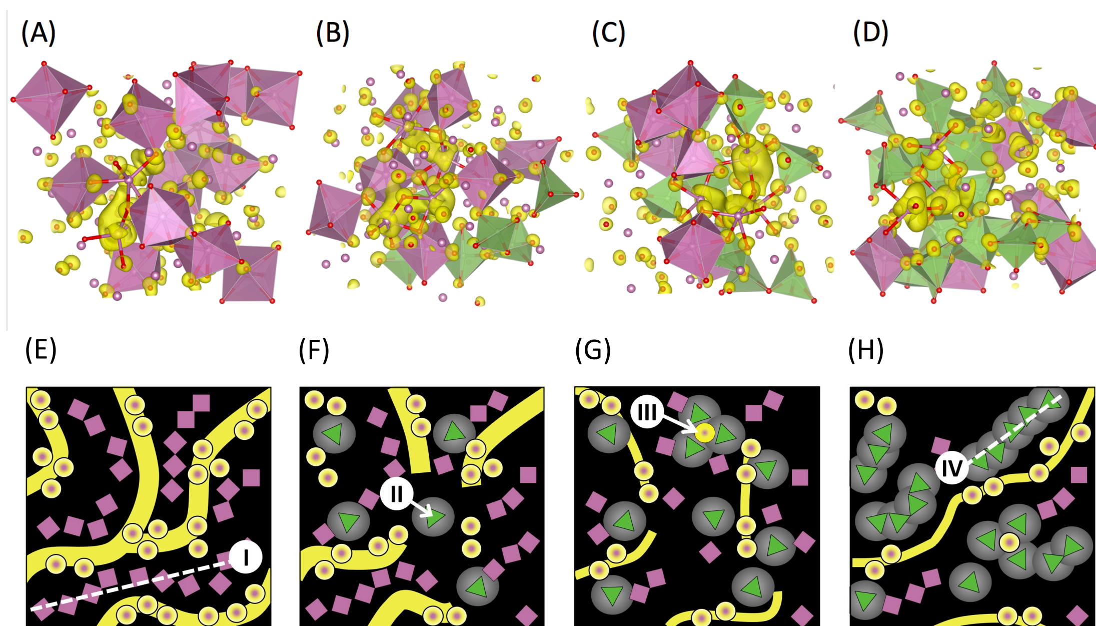

Figure 5.3. A,B,C,D) Calculated charge density distribution in the conduction band of a-IGO. Independent of Ga presence or content, the shallow defect state is associated with the charge accumulation between under-shared, low-coordinated, In-In pairs in: A) a-IO, B) IGO11, C) IGO19, D) IGO41. In all cases, the charge avoids octahedrally-coordinated In-O polyhedra (purple) as well as Ga-O polyhedra (green). For the under-shared, low-coordinated In atoms (no polyhedra), the In-O bonds are shown (red-purple). E,F,G,H) 2D simplification of the structures for E) a-IO, F) IGO11, G) IGO19, H) IGO41. In-O octahedral, represented as purple squares, form chains (I), which organize under-coordinated In-O polyhedra, represented as purple circles. This organization produces the yellow conduction manifold of high electron density. The conduction manifold begins to break up in the presence of Ga-O tetrahedra (II), represented as green triangles. Traps (III) form when Ga-O tetrahedra surround low-coordinated In atoms. At high Ga content, chains of Ga-O tetrahedra begin to form (IV), negating Ga's disruptive effect on the conduction manifold.

Owing to the many degrees of freedom in the amorphous structure, the entire cell adjusts to accommodate the O defect during the MD quench process for a-IO and a-IGO -- in marked contrast to the local atomic relaxation, *i.e.*, within the nearest and next nearest neighbors only, which occurs around O vacancies in crystalline oxides.

The long-range reconstruction of the amorphous structure in non-stoichiometric oxides limits the influence of secondary cations on carrier production. The theoretical results suggest the cation composition has little effect on the conduction states below the Fermi level. In figure 5.4, the calculated inverse participation ratio (IPR) for the occupied states in the conduction band is low, signifying that the defect is shallow and the delocalized nature of the occupied states in the conduction band persists in all 3 a-IGO simulations. This finding is supported by the fact that the Burstein-Moss (BM) shift, i.e., the Fermi level shift into the conduction band, calculated to be 1.41 eV, 1.46 eV, and 1.55 eV in IGO11, IGO19, and IGO41, respectively, is only slightly smaller than the BM shift in a-IO, 1.61 eV, with the same oxygen stoichiometry. Thus, Ga does not change the source of carriers in a-IGO.

The electron concentration calculated from integrated density of states within a 0.2 eV window below the Fermi level is, 2.80×10^{20} cm^{-3}, 2.03×10^{20} cm^{-3}, and 2.30×10^{20} cm^{-3} for 11%, 19% and 41% of Ga, respectively.

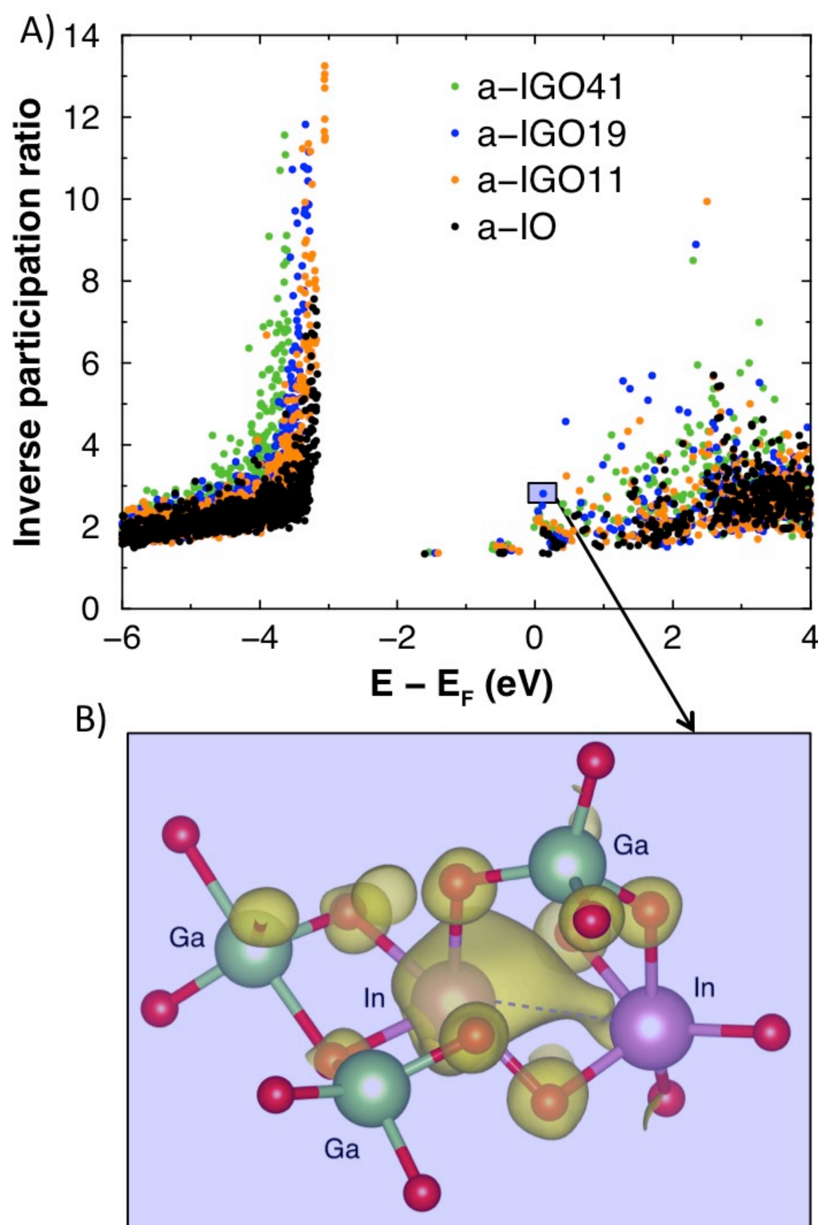

Figure 5.4. The calculated inverse participation ratio for a-IO and a-IGO. The valence band tail states are more localized in IGO than in IO owing to the presence of under-coordinated oxygen atoms. The conduction states below the Fermi level (at 0eV) are delocalized suggesting the formation of a shallow defect even at high Ga content. Localization of the empty conduction states above the Fermi level associated with non-uniform charge distribution, explain the observed mobility drop in a-IGO as compared to a-IO. Above the Fermi level, the charge density is localized at low-coordinate In atom surrounded by fully-coordinate Ga atoms as in B) a-IGO19.

The values as well as the trend for the a-IGO series are in excellent agreement with those observed experimentally (Fig. 5.1A). Based on the results of these calculations, the carrier concentration behavior in a-IGO can be explained as follows. In undoped a-IO, the majority of In atoms form a long-range network of octahedrally-coordinated In-O polyhedra[15] leaving behind O-depleted areas. These oxygen-depleted areas facilitate the formation of the remaining under-shared low-coordinated In into pairs, which generate charge carriers (Fig. 5.3A). Introduction of Ga suppresses the number of six-coordinate In-O polyhedra (Fig. 4.5A and 5.3A-C and E-G) and also dilutes the In-O lattice; both factors hamper the ability of two or more under-coordinate In atoms to cluster and form a donor defect. When the fraction of Ga increases above 17 at%, a long-range network of fully-coordinated Ga-O polyhedra emerges (Fig. 5.3D and H), re-enabling the formation of the O-depleted areas associated with under-shared low-coordinate In pairs. As a result, the carrier concentration is nearly independent of the Ga substitution in the range of 17-40 at%, Fig. 5.1A.

5.3.3 Carrier mobility experimental

The observed concomitant reduction of both carrier mobility and carrier concentration as a function of Ga content (Fig. 5.5), suggests that a-IGO transport is not limited by ionized impurity scattering.[106] Additional support is seen in the lack of a carrier mobility response to the drop in

carrier concentration, occurring upon air annealing between 150°C and 250°C (Fig. 5.1B). There is, however, a sharp fall in mobility above 325°C; this is attributable to the nucleation of the crystalline phase,[15] in the form of nano-scale inclusions, beginning ~100°C before the observation of strong diffraction peaks. Previous microscopy studies on a-IO[15] and a-IGZO[35] demonstrated the presence of nano-scale regions of ordering before the onset of X-ray diffraction peaks.

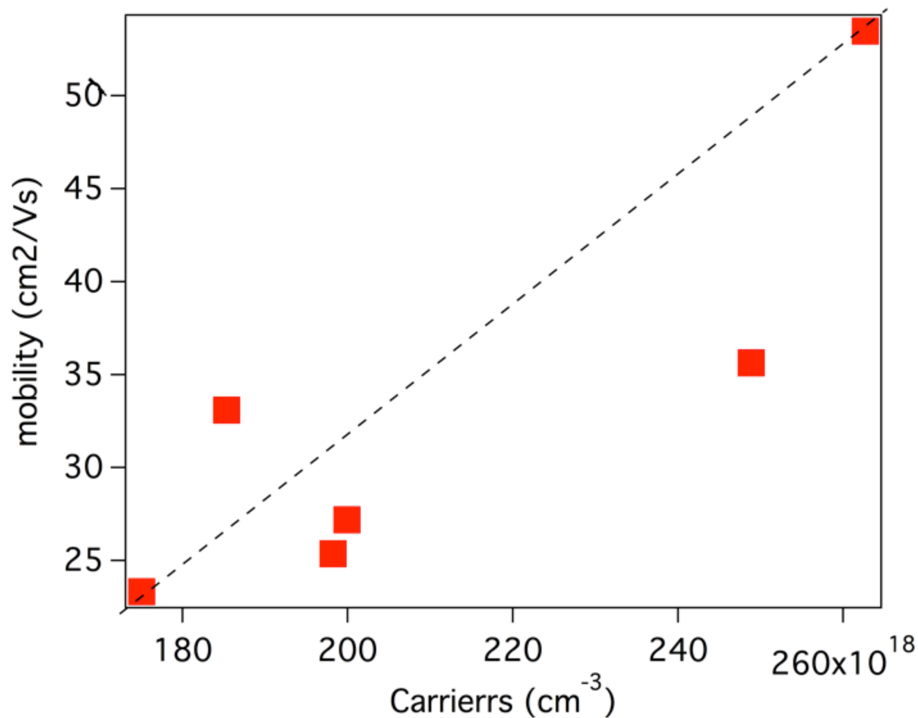

Figure 5.5. Plot of the Hall mobility of a-IGO films versus the corresponding carrier concentration. Mobility increases with increasing carrier content. If ionized impurity scattering were limiting mobility, the mobility should drop in response to rising carrier concentration. The dashed line serves as a guide for the eye.

The observation of a well-developed Hall effect suggests that band conduction is at play in the a-IGO system.[88, 96, 100-101] The proposed transport models which incorporate band-conduction typically consider a combination of trap states and percolation barriers as the factors limiting mobility in amorphous oxide semiconductors.[96, 99-100] From the above discussion, Ga is expected to affect the number and energy of percolation barriers and trap states by changing the O bonding and medium-range order of M-O polyhedra in a-IGO. The first shell structure around Ga is dissimilar to the surrounding In-O matrix (chapter 4, Table 4.1), suggesting Ga-O polyhedra may have a higher energy barrier associated with them.[4, 40] Ga also increases the overall structural disorder of the system. A comparison of the PDF of IGO8 (blue) and IGO17 (red) (chapter 4, Fig. 4.3B) illustrates Ga-induced disorder affecting the M··M distances and beyond. Greater disorder and a less relaxed structure has been associated with a greater number of trap states.[40, 88] The creation of barriers and traps by the addition of Ga is consistent with the observed fall in a-IGO mobility with increasing Ga content (Fig. 5.1A).

5.3.4 Carrier mobility: DFT computation

Electronic structure calculations on amorphous oxides provide microscopic insights into the origins of the complex transport behavior in materials such as a-IGO. Although the presence of additional cations in In-based AOSs does not directly govern the free carrier generation (see

Section 5.3.2), composition-induced differences in the O-sharing and medium-range spatial distribution of the differently-coordinated M-O polyhedra affect the carrier mobility. First of all, Ga suppresses the number of octahedrally-coordinated In atoms, and hence hampers the formation of shared InO_6 polyhedral chains. The latter have been shown to contribute to high mobility in a-IO:[15] chain formation organizes polyhedra with similar energy states and creates conducting paths along the chains (see Section 5.3.2). Accurate DFT-based hybrid-functional calculations of under-stoichiometric a-IGO reveal that the electron localization *above* the Fermi level increases significantly in all three a-IGO structures, as compared to a-IO. This increased localization supports the assertion that Ga inclusion adds to the density of traps. The calculated charge density distribution for the energy slice of 0.5 eV above the Fermi level (unoccupied states) demonstrates (Fig. 5.4) that an extra free electron is likely to be trapped at an under-coordinated In atom surrounded by three fully-coordinated Ga atoms. The empty states of the four-coordinate Ga atoms have a higher energy and, hence, are not available for conduction electrons. When the substitutional doping level in a-IGO increases, clustering of fully-coordinate Ga atoms leads to a non-uniform charge density distribution in the conduction states, rendering variable range hopping (VRH)[97-98] through the states of different energy the primary conduction mechanism. Indeed, the calculated electron velocity for the states *above* the Fermi level (the

states that form conductivity paths for the free electrons to hop through) decreases from $9.44x10^5$ m/s, to $9.35x10^5$ m/s, $8.96x10^5$ m/s, and $8.42x10^5$ m/s, for amorphous IO and IGO11, IGO19, and IGO41, respectively. Thus, the introduction of Ga affects VRH by increasing the range (distance) between hopping centers.

Once the Ga content approaches 20 at%, Ga has a greater role in the conduction manifold.[107] At higher Ga contents, the charge localization above the Fermi level decreases as evident from the comparison of the IPR values (fig. 5.4) for IGO19 (blue) and IGO41 (green): the IPR (IGO19) =4.6 is nearly two times larger as compared to the IPR (IGO41) = 2.5 within 0.5 eV above E_F (Figure 5). The weaker localization of the conduction states in a-IGO with higher Ga content is associated with the formation of an extended network of shared GaO-GaO polyhedra within the In-O matrix. As with the long chains of InO_6 that organize the low-coordinate In-O polyhedra together (Fig. 5.3A and E and Buchholz[15]), the formation of shared Ga-O polyhedral chains within the predominantly low-coordinate In-O matrix (Fig. 5.3D and H), again organizes the electron density and establishes two interwoven networks with dissimilar energies. Therefore, it can be argued that above 20 at% Ga in a-IGO, when the structure begins to transform from isolated Ga-O polyhedra to long-range Ga-O chains, the hopping between the low-coordinate In-O states is maintained. This explains the observed

unchanged mobility in a-IGO with Ga 20% and above (Fig. 5.1). Thus, the energy and the long-range spatial distribution of the polyhedra ultimately determine the complex behavior of mobility in amorphous IGO.

5.4 Conclusion

A systematic investigation of the electrical properties of a series of amorphous Ga- substituted In-O thin films was performed. Strong agreement between experimental results and theoretical simulations are demonstrated. The drop in carrier concentration and mobility coincident with Ga substitution was explored. The decline in both properties is shown to wane at Ga >20 at%. Ga dilutes carrier production because it inhibits the formation of under-shared low-coordinated In-O polyhedral pairs; these pairs, which are the amorphous equivalent of an O-vacancy, are identified as the source of carriers. Ga interrupts carrier mobility because it introduces disorder that leads to increased trap states. In addition, Ga dilutes the In-O polyhedral matrix increasing both the energy and range between variable range hopping centers. At high Ga contents the formation of Ga-O polyhedral chains limits the disrupting effects of Ga on both carrier production and carrier mobility. From a structure-property analysis of a-IGO in chapters 4 and 5 it is clear that changes in the local and medium-range structure affect thermal stability, carrier concentration, and carrier

mobility. Future modifications of AOSs through substitutional cations must balance such subtle interwoven effects.

CHAPTER 6: **Confirmation of the Dominant Point Defect Mechanism in a-IZO through the Application of *In Situ* Brouwer Analysis**

The dominant point defect mechanism of amorphous (a-) indium zinc oxide (IZO) was probed though *in situ* electrical characterization of sputtered, a-IZO thin films in response to changes in oxygen partial pressure pO_2 at 300°C. The results yielded a power law dependence of conductivity σ) versus pO_2 of ~ -1/6. This experimental method, known as Brouwer analysis, confirms doubly-charged oxygen vacancies as the dominant defect species in a-IZO. The success of this study suggests that Brouwer analysis is a viable method for studying the defect mechanisms of amorphous oxides.

6.1 Introduction

Amorphous (a-) oxide, transparent electronic, thin film materials are becoming increasingly prevalent in modern technology. Their low deposition temperatures, lack of grain boundaries, smooth surfaces, and high level of uniformity make them especially useful in display technology and suggest the possibility of fully transparent, flexible electronics.[4, 11, 13] Some of these materials, such as a-In-Ga-Zn-O, have already been commercialized. However, in order to fine-tune processing and inform the next generation of a-oxide materials, these materials must be fully understood on a fundamental level. Of particular note is the lack of understanding concerning the prevalent defect mechanism(s) and source(s) of carriers in these materials.[108]

The system of zinc-substituted indium oxide (a-IZO) is a strong candidate to develop the understanding of defects in amorphous oxides due to its technological relevance and thermal stability. Despite the differences in ionization state (Zn: 2^{+}, In^{3+}) combinatorial studies of a-IZO have shown a complete absence of p-type character. [9, 23-24]Additionally, composition has minimal effect on carrier concentration and has been shown to have no effect on the relationship between carrier concentration and mobility.[23] [9]Conversely, the amount of oxygen present during film deposition has drastic effects on carrier concentration. [10, 23-24] In order to understand the

persistent n-type character in a-IZO, as well as the drastic effects of oxygen content during deposition, the dominant defect mechanism in this system must be identified.

Brouwer analysis is a classical method used in the field of oxides to experimentally identify the dominant defect mechanism in a crystalline oxide.[28] Recently, this method was applied to an amorphous system for the first time. Work by Adler et al.[27] provided experimental results pointing to oxygen vacancies as the dominant defect species in a-IGZO (In-Ga-Zn-O). Oxygen vacancies have also been suggested as the primary source of carriers in a-IZO[24] and direct experimental evidence of doubly-charged oxygen vacancies as the dominant defect species was recently reported in an *ex situ* study of carrier concentration.[26] This work seeks to expand the understanding of the electrical properties of a-IZO, and to develop the application of Brouwer analysis to amorphous oxides, by using Brouwer analysis to identify the dominant defect mechanism in a-IZO.

Traditional Brouwer analysis is conducted with bulk polycrystalline samples at high temperatures (600-1200°C) where carrier concentration is driven to equilibrium at different oxygen partial pressures (pO_2).[28-31] A log-log plot of the resulting equilibrium conductivity vs. pO_2 yields a signature slope consistent with the underlying defect mechanism. For example, if

doubly-charged oxygen vacancies $V_O^{\bullet\bullet}$ are the dominant donor species, they would obey the following equilibrium reaction:

$$O^x \rightleftharpoons \frac{1}{2}O_{2(g)} + V_O^{\bullet\bullet} + 2e' \tag{6.1}$$

Where the equilibrium constant is given as:

$$K_{eq} = P_{O_2}^{\frac{1}{2}}[V_O^{\bullet\bullet}][n^2] \tag{6.2}$$

Utilizing the electroneutrality condition, $n = 2V_O^{\bullet\bullet}$, it can be shown that carrier content n should be proportional to $P_{O_2}^{-\frac{1}{6}}$. Thus, the expected signature slope on a log-log plot of carrier content (or conductivity, assuming negligible change of mobility) vs. oxygen partial pressure would be -1/6.

Though the amorphous nature of these materials provides many characteristics beneficial to their application in display technology, it also presents a significant challenge to fundamental studies. Of particular relevance is the limit of temperature, which must remain low to avoid both recrystallization and structural relaxation, thus careful and creative measures must be employed to extend the method of Brouwer analysis to amorphous materials. In a-oxides, Brouwer analysis has to date only been reported for a-IZO[26] and a-IGZO[27]. In the case of a-IZO an *ex situ* method was applied, which looked at carrier density of dc magnetron-sputtered ~100nm thick films subsequently annealed at 300°C under high oxygen pressures (200, 300, 600, and 800 atm). Pre-experiments were conducted to guarantee that the times employed (50h) were sufficient to

achieve defect equilibrium. A log-log plot of carrier density vs. oxygen fugacity (to correct for oxygen activity at high pressures) showed a -1/6.13 slope, consistent with the -1/6 signature slope for doubly-charged oxygen vacancies.[26]

The a-IGZO system was studied via an *in situ* method more analogous to traditional Brouwer analysis. Pulsed-laser deposited a-IGZO thin films, ~70nm thick, were placed in a tube furnace at 200°C and the time response of conductivity of the film to abrupt changes in oxygen partial pressure (using pre-mixed gas tanks of O_2 balanced with Ar: 100ppm, 1000ppm, 1%, and 10%) was recorded. Log-log plots of both conductivity and Seebeck coefficient (to confirm that negligible changes in mobility took place) exhibited slopes of -1/2, which was interpreted in terms of oxygen vacancies (doubly-charged and neutral, in combination).[27]

6.2 Experimental Procedure

6.2.1 Deposition

Indium zinc oxide films were deposited by magnetron sputtering on glass substrates ~1cm^2 in area by the Ginley group at the National Renewable Energy Laboratory. A 10.16 cm diameter 18/73 wt.% In_2O_3/ZnO oxide target (from Plasmaterials Inc.) was used to deposit the film. The film was sputtered with a power density of 2.5 W/cm^2 and the target-to-substrate distance was

~11 cm. System base pressure was 0.67 mPa (5×10^{-6} torr). A shuttered burn-in was performed with equal parts of oxygen and argon gas for 7 min to ensure target stoichiometry, followed by 3 minutes at the desired O_2 flow. During deposition, the pressure was held constant at 0.60 Pa (4.5 mTorr) with a total gas flow of 0.28/14.48 SCCM O_2 to SCCM Ar (SCCM denotes cubic centimeter per minute at STP). The actual argon and oxygen partial pressures in the chamber were monitored with a residual gas monitor. The films were deposited at ambient temperature with no intentional substrate heating (substrate temperature <100°C). The deposition resulted in films ~76 nm thick. Thickness was confirmed via ellipsometry (J. A. Woollam M2000U Ellipsometer). Initial Hall measurements confirmed the expected n-type character of the film. Initial carrier concentration was measured as 3.5×10^{19} carriers/cm^3 with a mobility of 46 cm^2/Vs. X-ray fluorescence (18 kW Rigaku generator equipped with a Mo rotating anode and a Vortex Si-drift diode detector, Tokyo Japan) confirmed the composition of the film was 85/15 at% In/Zn.

6.2.2 *In situ* electrical characterization

The film was placed in a 5.08 cm diameter quartz tube placed within a tube furnace initially held at 200°C (for 6 weeks) and then increased to 300°C to promote oxygen kinetics (Fig. 6.1). Though a-IZO of comparable composition has been shown to remain amorphous up to

500°C,[32] an upper limit of 300°C was chosen due to the extended anneal time (54 d total) used to explore the response of the film. Premixed gases of oxygen balanced with argon were flowed though Drierite desiccant to remove any water vapor and ensure that the reactivity of the gas environment was due solely to its oxygen content. Each gas mixture was flowed over the sample for 24 hours before being rapidly switched to the next mixture utilizing a 4-way valve (Fig. 6.1).

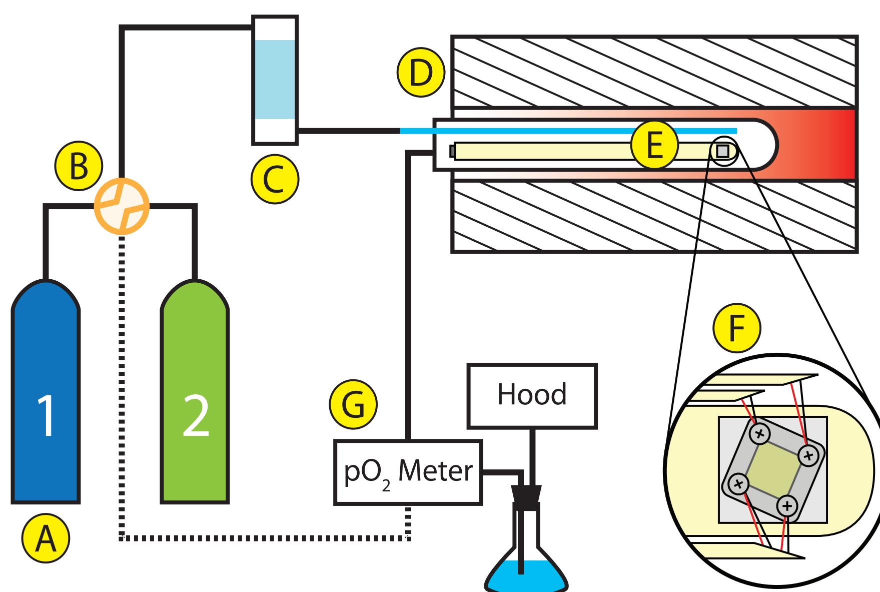

Figure 6.1. Experimental set up used to measure in situ conductivity as a function of O_2 partial pressure. A) Gas tanks of pre-mixed O_2/Ar, B) 4-way switch, C) Desiccator, D) Furnace held at 300°C, E) Sealed quartz tube, F) Van der Pauw contacts, G) pO_2 meter

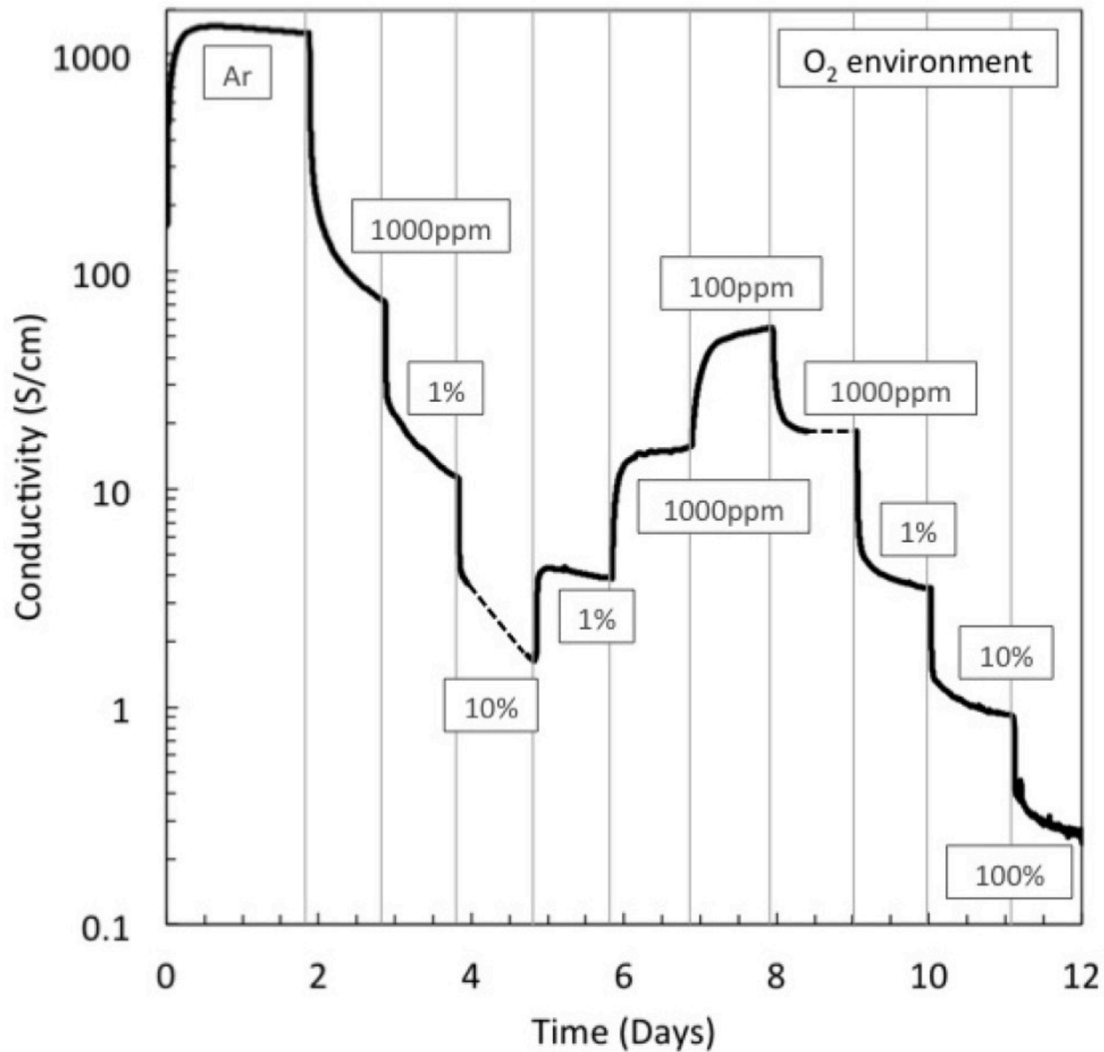

Figure 6.2. Conductivity transients of a-IZO as a function of time in response to varying oxygen environments. Dashed lines represent temporary interruptions in data acquisition.

The oxygen level of the film environment was monitored as the gas exited the furnace with an Ametek Thermox CG-1000 oxygen analyzer. Film conductivity, temperature, and thermopower were monitored via 4 thermocouples arranged in 4-point van der Pauw configuration. Electrical

measurements were taken with a scanner, current source, and multimeter (Keithley Instrument models 705, 224, 196) and automated to collect sheet resistance every 30 seconds. IV curves were collected periodically to ensure that Ohmic behavior was maintained throughout the experiment. Thermopower (Q) was monitored throughout the experimental campaign. A plot of the DOS-mobility product ($\ln(\sigma)$-Q_{red}) (Fig. 6.4) illustrates that mobility remains constant throughout the experiment and implies that changes in conductivity can be interpreted as changes in carrier concentration. For a full derivation of the DOS-mobility product please see the supplementary information of Adler et al.[27]

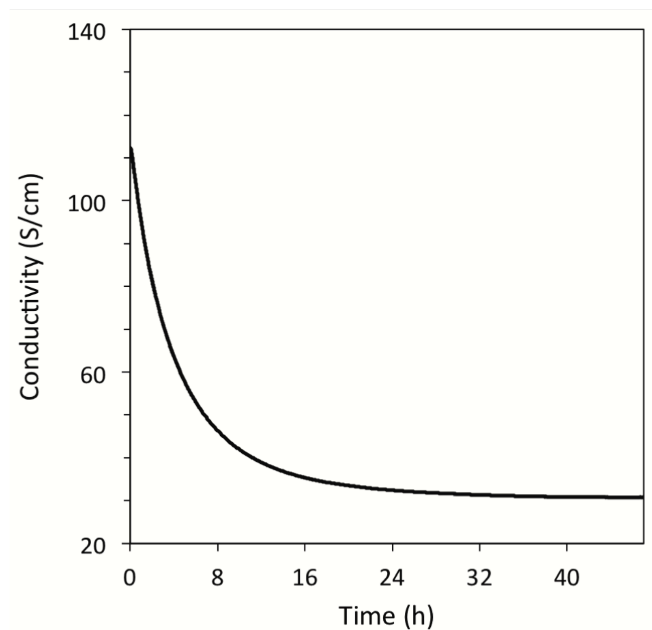

Figure 6.3. Conductivity response of a-IZO thin film at 200°C during an oxidative transient measured in situ as a function of time. $PO_{2initial}$: 1000 ppm PO_{2final}: 1.0%

An initial campaign at 200°C (6 weeks) proved inconclusive; individual transients did not display discrete relaxation regimes as were seen at higher temperatures (see discussion below). Therefore, all subsequent measurements were made at 300°C. A sample oxidative transient at 200°C is shown in figure 6.3.

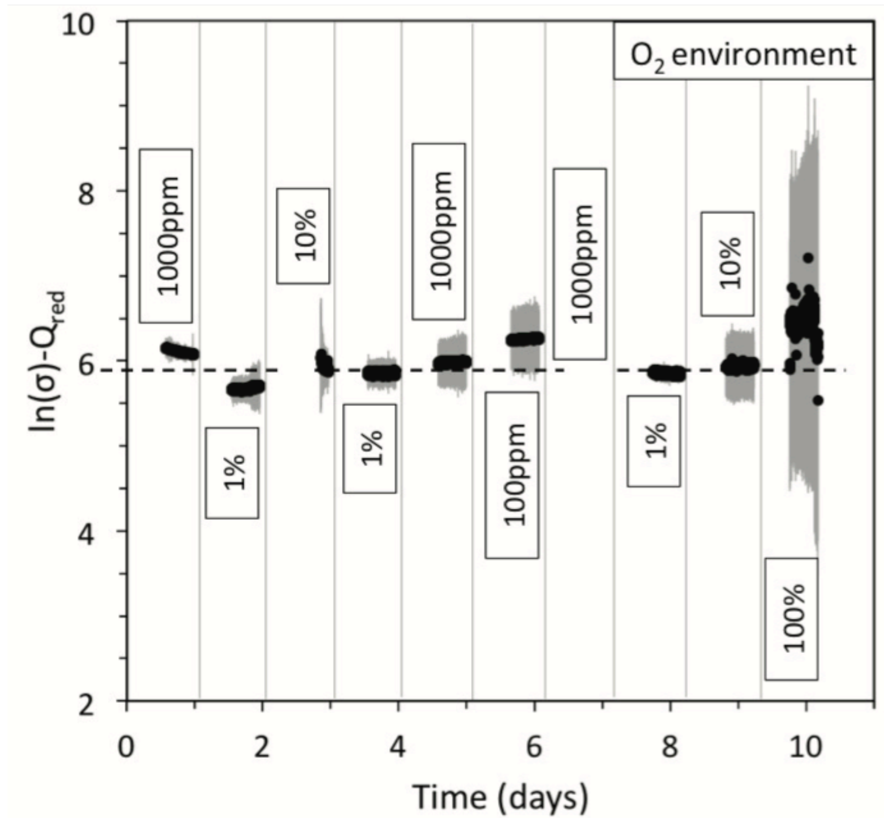

Figure 6.4. In situ DOS-mobility product ($\ln(\sigma)-Q_{red}$) for a-IZO films at 300°C as a function of time illustrating that mobility remains constant in response to changes in O_2 environment over the experimental campaign. The last 10 hours of exposure to each pO_2 are represented as black dots and error bars are represented as grey lines. Disruptions in the dashed line represent temporary interruptions in data acquisition, as seen in the conductivity results (Fig. 6.2).

6.3 Results and Discussion

Conductivity was seen to decrease under oxidizing conditions and increase under reducing conditions, as is expected for an n-type material. However, as with the results seen by Adler et al., the oxidizing response (Fig. 6.5) displayed three regimes: a rapid surface response (regime 1, blue), a slow background decay (regime 3, red), and a middle regime (region 2, white) attributed to defect modulation (Fig. 6.5a).

6.3.1 Regime 3: background decay

The slow background decay under all pO_2 values is attributed to gradual structural relaxation independent of oxygen environment throughout the entire 54-day campaign. Evidence of a sluggish conductivity response (on the order of days) has been previously seen and similarly attributed to a structural relaxation.[27, 109] Evidence of this structural relaxation can be seen in glancing incidence X-ray diffraction scans (GIXRD) (Fig. 6.6) performed before and after the 54-day campaign. Though the broad nature of the peaks and their low intensities (comparable to the underlying glass substrate) confirm the maintained amorphous nature of the film, a small secondary hump appears in the post anneal scan around 55 degrees (2θ). This suggests that the film moves towards a more ordered state over the experimental campaign.

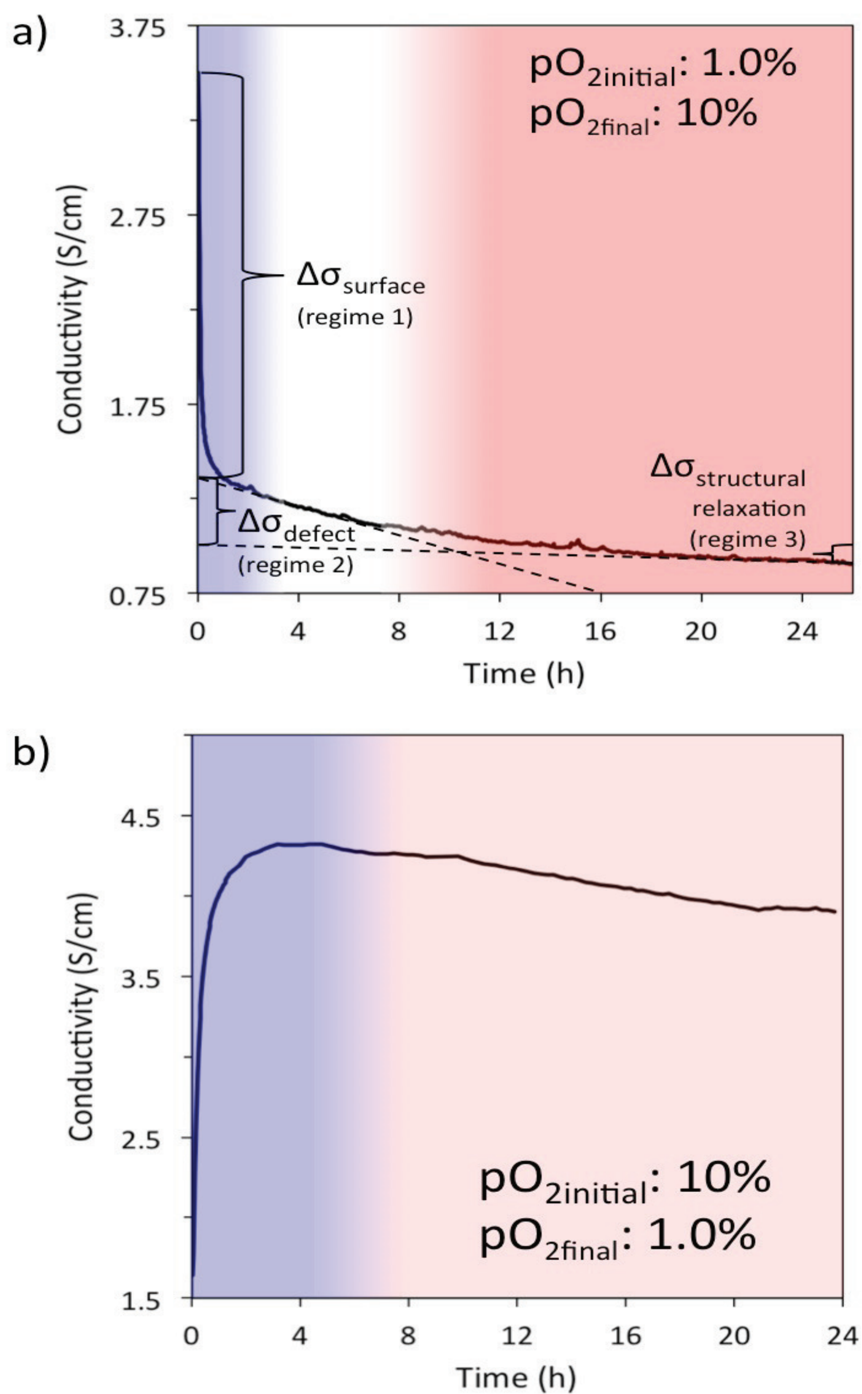

Figure 6.5. Conductivity response of a-IZO thin film during a) oxidation and b) reduction measured in situ as a function of time. From left-to-right: regime 1 (blue), regime 2 (white), and regime 3 (red) correspond to the dominant mechanism during the indicated time periods (surface response, bulk defect modulation, and background structural relaxation).

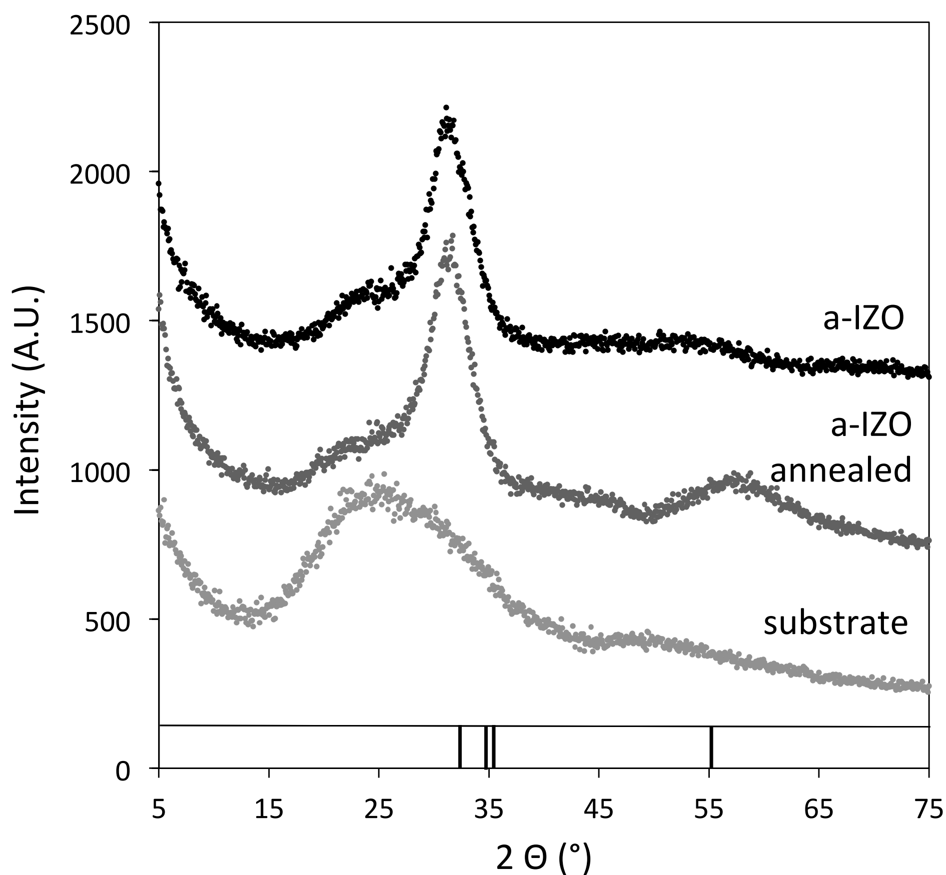

Figure 6.6. GIXRD scans of the a-IZO thin film before (top) and after (middle) the experimental campaign, in comparison with the glass substrate (bottom). The major peaks of crystalline InZnO are indicated by the vertical dashes above the x-axis.[7] GIXRD scans were performed with a Rigaku Smartlab diffractometer.

Given that sputtered amorphous oxides are kinetically, but not thermodynamically, stable it is reasonable to assume that small local rearrangements could take place over the extended time frame of the experiments. Furthermore, theoretical studies[91] have suggested that local

environment can affect the ability of amorphous oxides to create oxygen defects, suggesting that small changes in local structure could be reflected as slow changes in the conductivity of the film with time. Further quantification of this response is being explored through local structure studies (EXAFS, extended X-ray analysis fine structure), but is beyond the scope of this chapter.

6.3.2 Regime 1: surface response

The initial response of the film is similar to that of a gas sensor. Due to the low temperatures required, adsorbed oxygen species remain on the surface of the film. These adsorbed species create a space-charge layer near the surface of the film, which results in band bending. This band bending is reflected as a sharp drop in the conductivity of the film under oxidizing conditions and a sharp increase under reducing conditions.[110-111] This response is seen to exponentially decay as the equilibrium adsorbed-population is approached. Though a-IZO has not been explored as a gas sensor, similar systems (IZO nanowires[112] and a-IGZO[113] have been explored under both oxidizing and reducing conditions and the response times of these materials are on the order of those seen in the present work (~1-2h).

6.3.3 Regime 2: bulk defect modulation

In order to study the effects of defect modulation as a function of oxygen pressure and to extract a Brouwer slope, the effect of surface adsorbed oxygen and background defect modulation must

be removed from the total conductivity response. In order to deconvolute the middle regime and reveal the effect of carrier concentration on pO_2, the contributions of regimes 1 and 3 need to be subtracted out. At 200°C the three regimes were found to be too convoluted for meaningful analysis. A sample oxidative transient at 200°C can be seen in Figure 6.3. Therefore, the temperature was increased to 300°C. Even at this temperature, the three regimes could only be deconvoluted when oxidizing to higher pO_2 values (1, 10, 100%). Under these conditions, three distinct regimes emerge for positive ΔpO_2 (oxidizing changes). However, for negative ΔpO_2 (reducing changes), owing to the conflicting nature of the background contribution (decreases σ) and defect reduction (increases σ), the defect response modulation response (regime 2) could not be obtained, as shown in figure 6.5.

Because the background decay operates on such a long time scale we can approximate the response due to structural relaxation within a 24-hour period as linear (Fig. 6.5a). Due to noise and the imprecise nature of the transition from one regime to the next, there is some uncertainty to the linear fits. To account for this uncertainty, the response due to background decay was fit to five linear best-fit lines to extract an average y-intercept indicating the equilibrium value obtained only by defect modulation. The standard deviation between each of the five fits was used to create error bars. The delineation between the first (surface) and second (defect) regimes

is more clearly seen due to the exponential nature of the adsorbed oxygen response. The defect response appears to be well modeled by a linear fit (Fig. 6.5 a). As with the background decay, five best-fit lines were used to extract a y-intercept value (and corresponding error bars) where the initial conductivity of the film would begin at the onset of defect modulation if adsorbed oxygen were not a factor. In this fashion, the conductivity response owing solely to the defect response of the film could be obtained. In equation 6.3, the β value corresponds to the signature slope of carrier concentration versus oxygen partial pressure.

$$\sigma = A \times pO_2^{\beta} \tag{6.3}$$

Values of β were obtained using the following equation:

$$\beta = \frac{\Delta \log \left(\sigma_{defect}^{regime2}\right)}{\Delta \log (pO_2)} \tag{6.4}$$

The results are plotted in figure 6.7, where a signature slope (β value*)* of ~ -1/6 is obtained. This result supports the previous report that the dominant defect mechanism in a-IZO is doubly-charged oxygen vacancies. The present *in situ* results on a-IZO films combined with the *ex situ* results of Lee et al.[26] are significant in that they suggest that, despite their amorphous character, a-oxide films are amenable to point defect studies by Brouwer analysis. In addition, the present work supports the contention of Adler et al.[27] that *in situ* Brouwer studies can be

successfully carried out on a-oxide films over a wide range of compositions. Ongoing work is applying Brouwer analysis to other a-oxide systems.

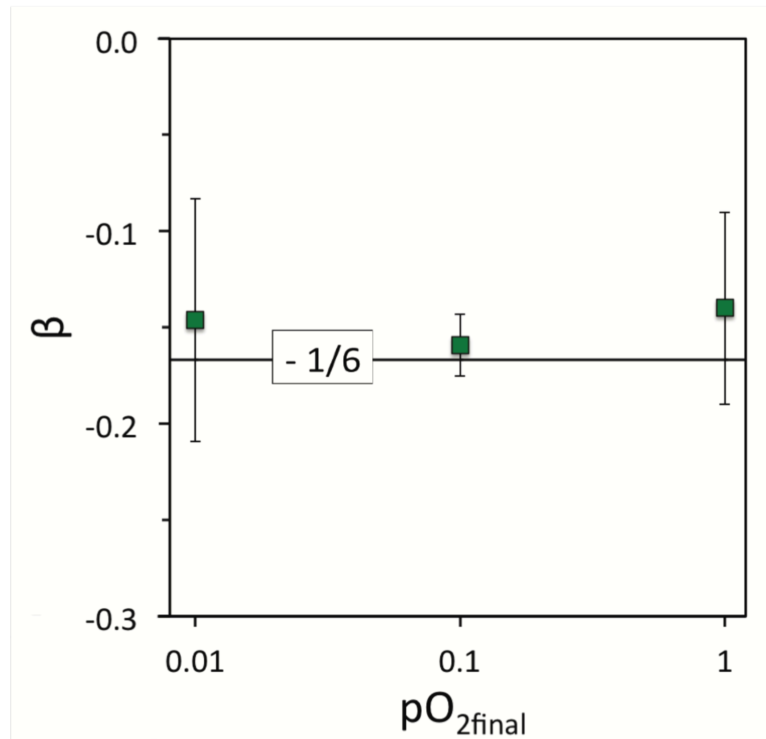

Figure 6.7. β values (which correspond to the slope in a Brouwer plot) as a function of equilibrium O_2 partial pressure (pO_2).

6.4 Conclusion

In situ electrical characterization of sputtered, ~76nm thick, a-IZO thin films in response to changes in oxygen partial pressure was carried out at 300°C. The oxidizing response (positive ΔpO_2) was seen to fall into three regimes dominated by three effects: surface adsorbed oxygen,

bulk defect modulation, and a long-term background decay. These regimes were deconvoluted to yield $\Delta\log(\sigma)/\Delta\log(pO_2)$ values of ~ -1/6 in the defect modulated regime, which is consistent with doubly-charged oxygen vacancies being the dominant defect species in a-IZO, as seen previously at high pressures by *ex situ* analysis. [26] The success of this study and the agreement between *in situ* and *ex situ* studies suggests that *in situ* Brouwer analysis is a viable method for studying the defect mechanisms of amorphous oxides.

CHAPTER 7: **A Fundamental Comparison of Combustion Synthesis and Pulsed Laser Deposition: Film Growth Processes in the a-IGO System**

Solution processing of amorphous oxide semiconducting films will likely provide a significant step towards the realization of affordable, flexible, transparent electronics. This work directly compares one of the most promising solution processing techniques, combustion synthesis (CS) (via spin and spray methodologies), with the more conventional synthesis technique, pulsed laser deposition (PLD). Films and devices are compared in the a-IGO system, across the In-Ga composition space, as calibrated by X-ray fluorescence. Semiconducting layers deposited by either CS or PLD are used as the channel layer in thin film transistors (TFTs) fabricated on SiO_2/Si substrates. Devices are evaluated under ambient conditions to compare the effect of processing method on film performance. In this work, TFTs with PLD channel layers demonstrate the highest mobility 42 $cm^2 \cdot V^{-1} \cdot s^{-1}$, but CS films exhibit comparable performance in other transistor metrics (on-voltage, etc.). Of the growth methods assessed, spin-coated CS films produce TFTs with the most reliable performance and the clearest Ga-dependent trends. This work also demonstrates that spray-coated CS TFTs have consistently low threshold voltages, suggesting the spray-coating method leads to low carrier concentrations.

The role of processing method on amorphous oxide thermal stability is analyzed through *in situ* glancing incidence X-ray diffraction annealing studies. All of the CS films have superior thermal stability versus the PLD films. Insight into film performance is gained by analysis of film microstructure over several length scales and includes analysis of local bonding and density.

7.1 Introduction

Amorphous transparent conducting oxides (a-TCOs) have many attractions over their crystalline counterparts. Their amorphous nature results in a lack of grain boundaries, making a-TCOs well suited for large area applications.[2-3] Of even greater importance, a-oxides can be grown as semiconductors with high mobility at low temperatures, and have demonstrated excellent thin film transistor (TFT) device performance when grown at room temperature.[4-6] Depositions only requiring low temperatures result in lower processing costs and, more notably, open the door to depositing on flexible polymeric substrates.[114-115] Flexible electronics could provide more durable, portable, and biocompatible devices for the increasingly pervasive personal electronics industry.[116-118]

Recent work has demonstrated that amorphous (a-) oxide films can be prepared via solution processing methods at low temperatures.[6, 119-121] Before that, most a-oxide films were grown by

physical vapor deposition (PVD) techniques near room temperature (RT), such as sputter deposition and pulse laser deposition (PLD).[51] However, solution processing offers the potential of roll-to-roll printing/patterning of flexible electronics, increasing the large-scale manufacturability of amorphous oxides.[118] The realization of high-quality/high-mobility amorphous oxide films on flexible substrates was initially hindered by the requirement of high synthesis temperatures ≥ 400 °C in more traditional sol-gel methodologies.[122-123] However, by introducing additional energy to the film growth precursors through UV irradiation[115, 124-125] or solution-based fuel-containing precursors,[43-44, 126-127] low substrate temperatures can be maintained during growth, and good device-quality, densified films can be produced. One of the most promising low-temperature solution processing methods is combustion synthesis.[44] Combustion synthesis creates small, local-scale, exothermic reactions though the addition of acetylacetone "fuel" into metal nitrate precursor solutions; these local-scale reactions effectively lower the activation barrier to metal-oxide lattice condensation and reduce the global annealing temperature.[43-44] Combustion synthesis (CS) solutions can be deposited onto substrates through either a spray (Spray-CS, Figure 1B)[128-129] or spin (Spin-CS, Figure 1C)[40, 44, 127] coating process.

This work provides a direct and in-depth comparison of these fundamentally dissimilar synthesis techniques, pulsed laser deposition (PLD, Figure 1A) and combustion processing

(spray and spin, Figures 1B and C), to elucidate the effects of processing methodology on the properties and performance of a-oxide semiconductors.

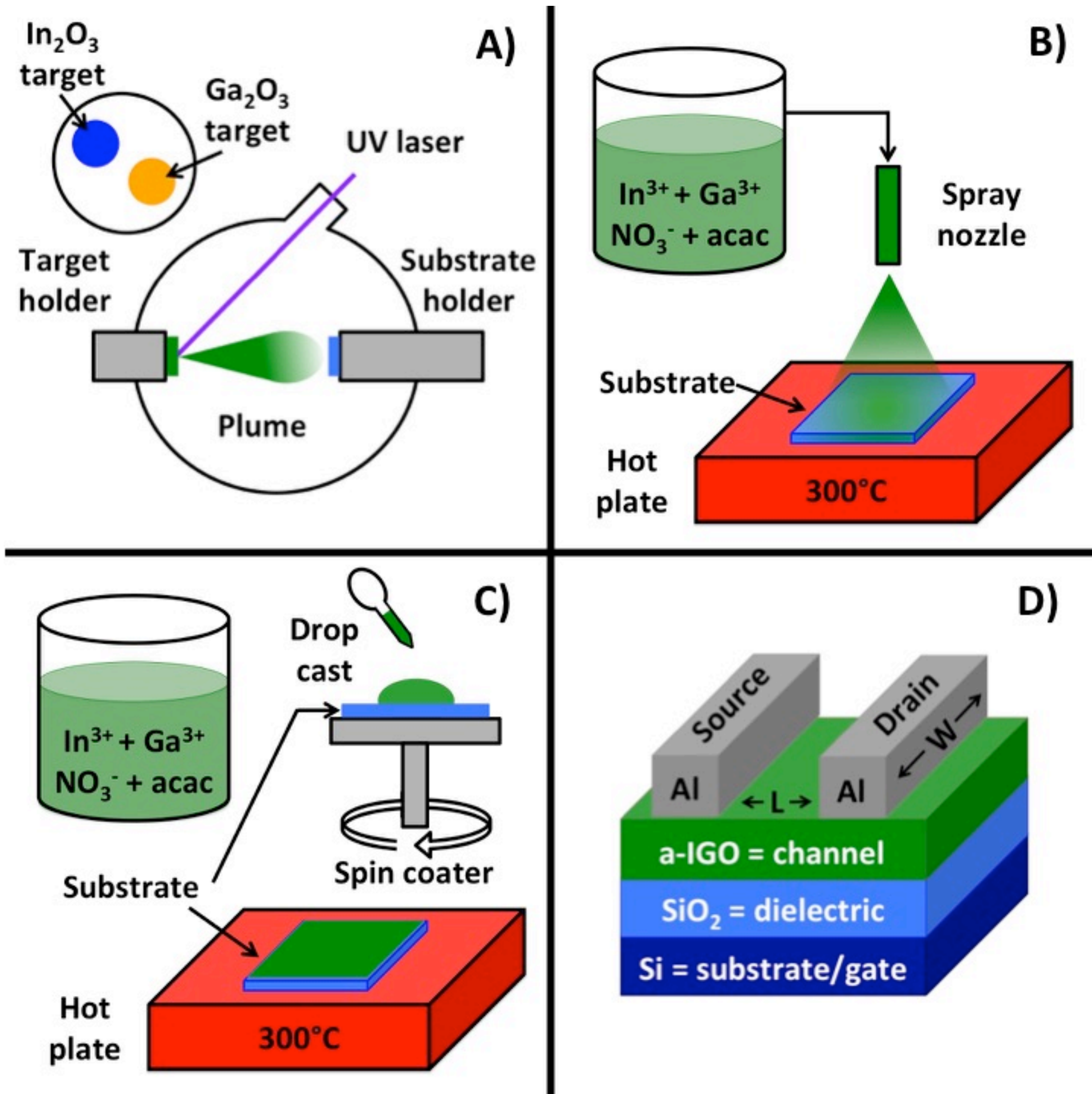

Figure 7.1. A schematic demonstrating the A) PLD deposition method, B) Spray-CS method, and C) Spin-CS method. All three methods were used in creating the channel layer of transistors with the architecture shown in D).

These methods are compared using the amorphous In-Ga-O (a-IGO) system as a model TCO class. The use of a materials system rather than a single composition enables the systematic comparison of structure-property trends and provides greater confidence in assessing underlying causes. a-IGO provides a simpler two-cation system where a foundational study on PLD a-IGO can be referenced (chapters 4 and 5).[130] TFT performance is evaluated for devices fabricated on SiO_2/Si substrates with Al contacts; a-IGO films prepared by PLD, Spin-CS, and Spray-CS serve as the channel layer. TFT mobility is an important metric in creating efficient TFTs capable of operating at high speeds and enabling devices with fast refresh rates. In this investigation, we demonstrate that PLD films exhibit the highest mobilities, but that solution processed combustion-derived films are close competitors The highest performing Spin-CS films in this work establish devices with the best reported average mobility for a solution processed IGO transistor (17.67 $cm^2 \cdot V^{-1} \cdot s^{-1}$). Control of on-voltage is important for improving the energy efficiency of transistors. An ideal transistor can be turned on at low-voltage and does not require a back voltage to remain in the off state. The most consistent, and composition independent, V_{on} in this work are seen in the Spray-CS films and suggests that the Spray-CS method leads to consistently low carrier concentrations.

The role of deposition parameters on a-IGO thermal stability is assessed here through *in situ* glancing incidence X-ray diffraction (GIXRD) measurements taken during air annealing studies. The need to ensure thermal stability of the amorphous phase was emphasized as early as Nomura's work in 2004.[4] Multiple studies since have explored the thermal stability of amorphous phases in response to post deposition annealing, but only for PVD films.[33-34, 36, 41, 131] Previous work has shown that the onset of crystallization can greatly reduce carrier mobility[15, 41] and result in poor uniformity of the threshold voltage (V_{th}).[132] As channel layers, amorphous oxides are only a single layer within a multi-layer device; thermal stability is important to maintain stable film performance after additional layer deposition. Insight into thermal stability is obtained here through X-ray reflectivity (XRR) and X-ray absorption spectroscopy (XAS) characterization. It will be seen that the evolution of density upon crystallization is greatest for the combustion processed films and contributes to the superior thermal stability of combustion-processed films over PLD films.

7.2 Results and Discussion

7.2.1 Transistor characterization

PLD channel layers were grown at 25°C in 48.5 mTorr of O_2. It was necessary to optimize the O_2 partially pressure; reducing it in the deposition chamber by only 3 mTorr resulted in films that were too conductive to create functioning TFTs. Note that the importance of O_2 environment has also been reported in sputtered a-IGO films.[41, 133] PLD devices with channel layers containing 9.3 at% Ga (IGO9.3) exhibit the highest saturation mobility (μ_{sat}), 42.13 $cm^2 \cdot V^{-1} \cdot s^{-1}$ (Table 7.1). PLD IGO transistors have not been reported however, top-performing sputtered IGO channel layers having μ between 27[134] and 43[133] $cm^2 \cdot V^{-1} \cdot s^{-1}$ have been reported, in good agreement with the top-performing PLD TFTs in this work. Spin-CS channel layers were fabricated at 300 °C. The highest μ_{sat}, 17.67 $cm^2 \cdot V^{-1} \cdot s^{-1}$, was measured on the film with the lowest Ga content, mirroring the trend measured in PLD devices. The μ_{sat} values of the IGO13.9 devices represent a significant improvement over other solution-processed IGO TFTs with reported mobility ranges between 1-12.7 $cm^2 \cdot V^{-1} \cdot s^{-1}$, while the report[121] of 12.7 $cm^2 \cdot V^{-1} \cdot s^{-1}$ is from a film processed at 500 °C.[120-121, 132, 135-139]

Table 7.1. Performance metrics from TFT devices made with 10-15 nm a-IGO channel layer films deposited on SiO_2/Si with Al contacts fabricated via PLD, Spin-CS, and Spray-CS[a]

Composition	μ (cm^2/Vs)	V_{th} (V)	V_{on} (V)	Log (On/Off)	Sub. Slope (V/dec)
PLD IGO 9.3	42.13 ± 0.87	9.65 ± 0.94	-1.80 ± 0.63	6.76 ± 0.11	1.27 ± 0.07
PLD IGO 18.0	20.05 ± 5.31	-67.40 ± 10.43	-74.8 ± 2.39	3.65 ± 0.97	8.02 ± 4.91
PLD IGO 28.0	16.21 ± 4.32	-24.3 ± 6.51	-28.70 ± 1.95	5.89 ± 0.40	1.84 ± 0.34
PLD IGO 35.0	4.56 ± 2.06	-1.09 ± 8.92	-8.20 ± 1.32	6.16 ± 0.41	1.20 ± 0.14
Spin-CS IGO 13.9	17.67 ± 1.15	-13.96 ± 11.35	-25.78 ± 4.76	4.95 ± 1.13	4.30 ± 5.07
Spin-CS IGO 25.6	10.60 ± 0.22	4.85 ± 2.31	-13.22 ± 7.33	6.20 ± 0.41	2.11 ± 0.98
Spin-CS IGO 39.1	9.52 ± 1.05	6.21 ± 6.59	-7.88 ± 3.80	6.64 ± 0.22	1.69 ± 0.55
Spin-CS IGO 50.9	2.51 ± 0.54	10.13 ± 2.08	-0.22 ± 1.20	6.67 ± 0.26	1.44 ± 0.20
Spray-CS IGO 18.2	5.52 ± 0.49	4.92 ± 5.23	-12.00 ± 4.67	5.19 ± 0.17	2.88 ± 0.34
Spray-CS IGO 26.2	6.60 ± 0.16	9.67 ± 2.04	-8.50 ± 2.46	5.64 ± 0.30	2.13 ± 0.31
Spray-CS IGO 33.1	6.74 ± 0.35	9.03 ± 1.55	-6.70 ± 1.64	5.70 ± 0.23	1.99 ± 0.21
Spray-CS IGO 42.3	5.03 ± 0.23	12.98 ± 0.82	-2.00 ± 1.25	6.02 ± 0.29	1.68 ± 0.24

[a] From ≥ 10 devices made on each representative film

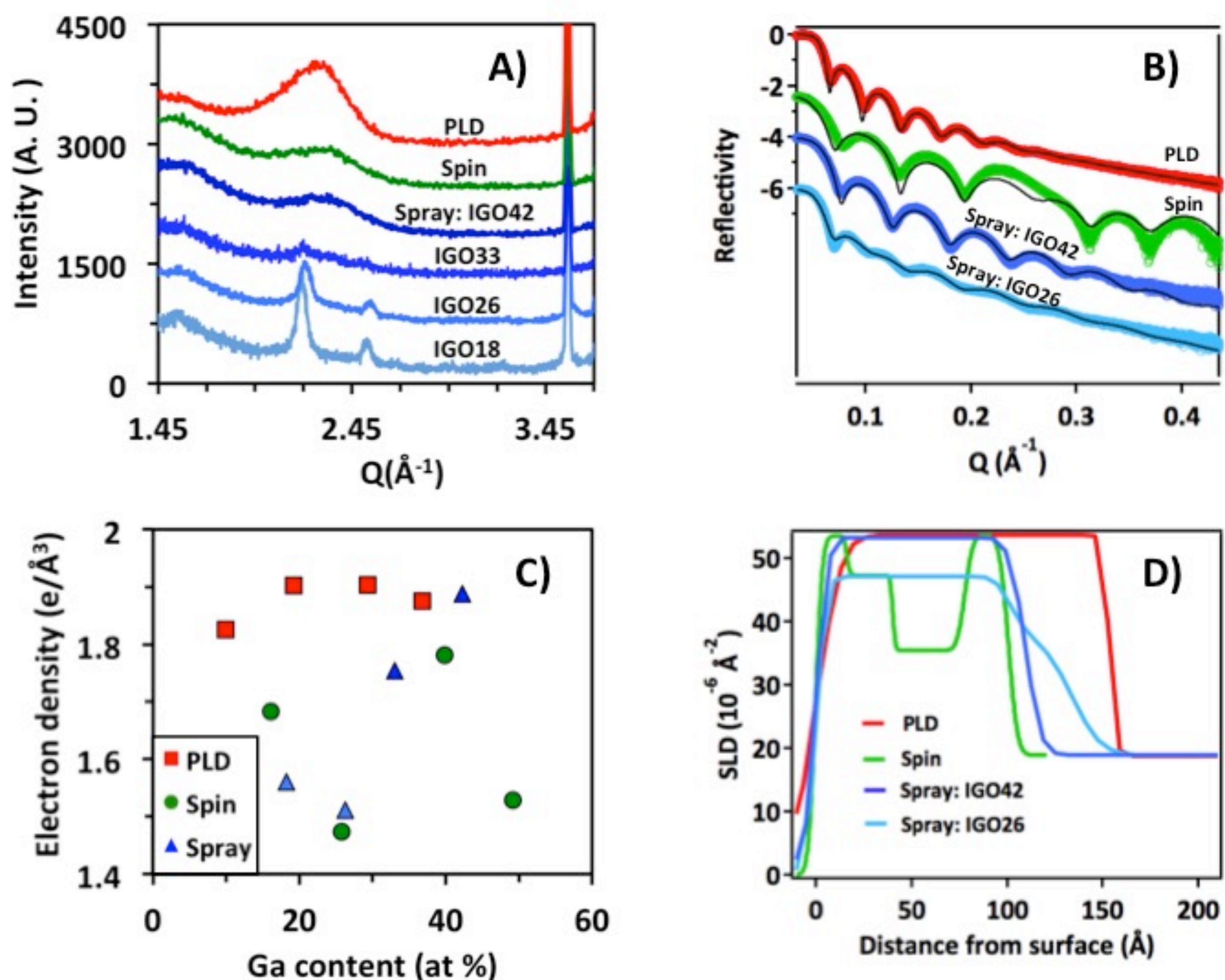

Figure 7.2. X-ray characterization data for IGO TFT films grown by PLD (red), Spin-CS (green), and Spray-CS (blue). A) GIXRD patterns of as-deposited IGO films before the deposition of Al contacts. Note, that at low Ga content, Spray-CS films are partially crystalline and display peaks at Q values of ~2.2 and 2.5. The 400 peak from the Si substrate can be seen at Q ~3.6. B) XRR plots of as-deposited IGO films. Fits are shown as black lines. C) Electron density of each TFT channel layer. Films with multiple layers are presented as the average density of all layers. D) Scattering length density (SLD) as a function of distance from the surface of the film.

Spray-CS channel layers were initially grown at 250 °C where all films are amorphous across the entire In-Ga composition space however, charge transport was immeasurably low in these films so that functioning TFTs were unobtainable. However, functioning TFTs could be fabricated with Spray-CS films grown at 300 °C. This work represents the first report of IGO TFTs made through a spray solution processing method. The highest μ_{sat} for a Spray-CS film, 19.99 $cm^2 \cdot V^{-1} \cdot s^{-1}$, was measured for devices fabricated with an IGO26.2 film. However, the large spread in μ_{sat} values for IGO26.2 film devices resulted in a standard deviation >2× higher than for devices made with other Spray-CS films. In addition, μ_{sat} for a second IGO26.2 film was lower, 6.60 $cm^2 \cdot V^{-1} \cdot s^{-1}$. This discrepancy is likely due to the partially crystalline nature of the IGO26.2 films (Fig. 7.2A) and highlights the importance of film thermal stability in creating reproducible devices.

Both Spin-CS and PLD TFTs exhibit a downward trend in IGO μ_{sat} with increasing Ga content (Fig. 7.3A). This trend has previously been reported in both TFT-derived mobility [41, 120, 138] and Hall mobility[140] for a-IGO films grown via sputtering [140] [41] and solution processing methodologies [120, 138]. MD simulations combined with DFT illustrate that the preference of Ga to remain 4-fold coordinate is effective in disordering and disrupting the conduction manifold and thus decreasing mobility (chapter 5). [87]

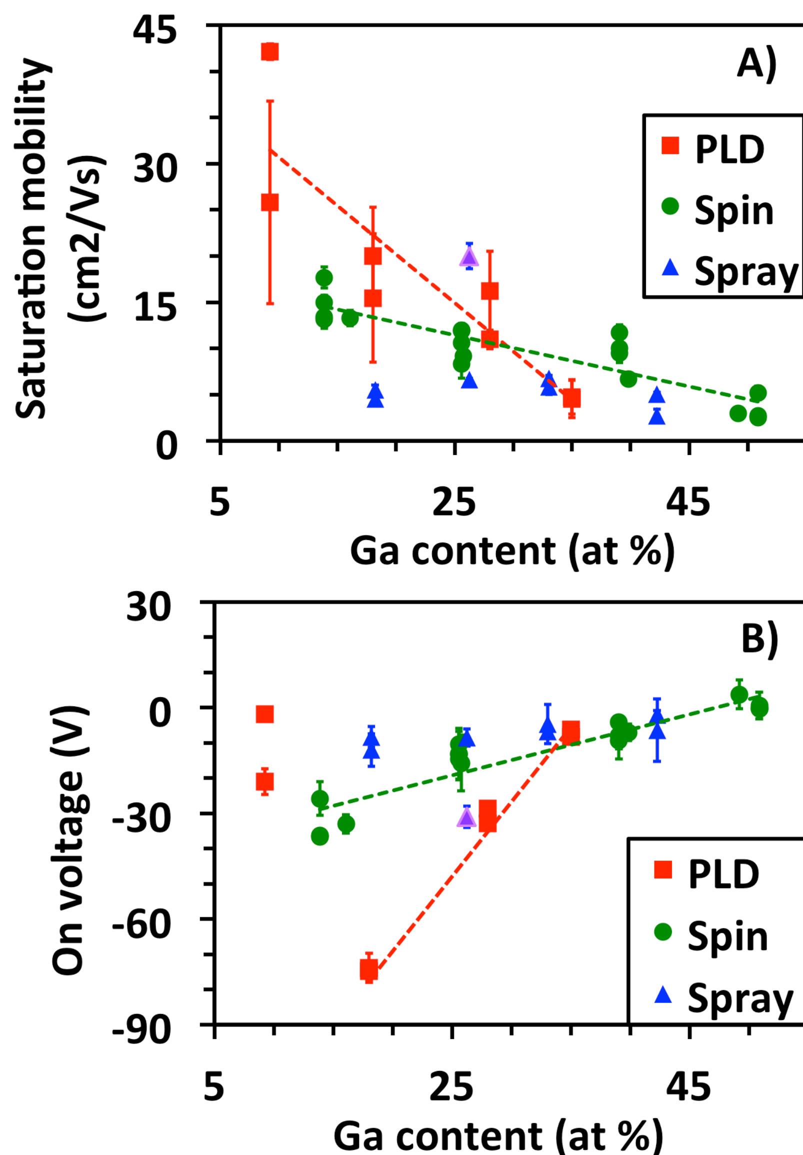

Figure 7.3. Saturation mobility A) and on voltage B) of TFT devices made with a-IGO channel layers deposited by PLD (red squares), Spin-CS (green circles), and Spray-CS (blue triangles). Each point represents a separate film deposition. Greater than 10 devices were measured on each film; error bars represent the standard deviation between devices. Dashed lines represent linear best fits of PLD (red) and Spin-CS (green) data and are provided to highlight Ga-dependent trends. Purple triangle represents partially crystalline Spray IGO26 film.

Note that evidence of 4-fold coordinate Ga in the present IGO films is provided by extended X-ray absorption fine structure (EXAFS) analysis (Fig. 7.4) of the PLD and Spin-CS films. Furthermore, 4-fold coordinate Ga is also found to be a significant source of traps (chapter 5). This is indicated by the increase in the hysteresis of forward-and-reverse voltage sweeps (Fig. 7.5) as the Ga substitution level increases, and is observed for both the Spin-CS and PLD TFTs. No significant Ga-dependent trends are seen in the Spray-CS films, suggesting that processing conditions have the dominant influence on μ_{sat} and trap density in Spray-CS films. Along these lines, the sub-threshold swing is large and μ_{sat} is similar for all Spray-CS devices, regardless of composition. In comparing the PLD devices to the solution processed devices (Spin-CS and Spray-CS), μ_{sat} is clearly the device metric where the PLD films are superior. The fully amorphous (Fig. 7.2A) nature and consistently high as-deposited film densities (Fig. 7.2D) are likely the contributing factors to the high mobilities of the PLD films, as compared to the solution-processed films.[15, 128, 134]

An uptrend in a-IGO TFT on-voltage (V_{on}) with increasing Ga content is established here for all Spin-CS devices and PLD TFTs with >10 at% Ga (Fig. 7.3B; Table 7.1). Such an increasing V_{on} suggests that carrier concentrations decrease with increasing Ga content, and is in

accord with reduced a-IGO carrier concentrations with added Ga reported previously from transistor metrics[120, 137-138] and Hall measurements[140].

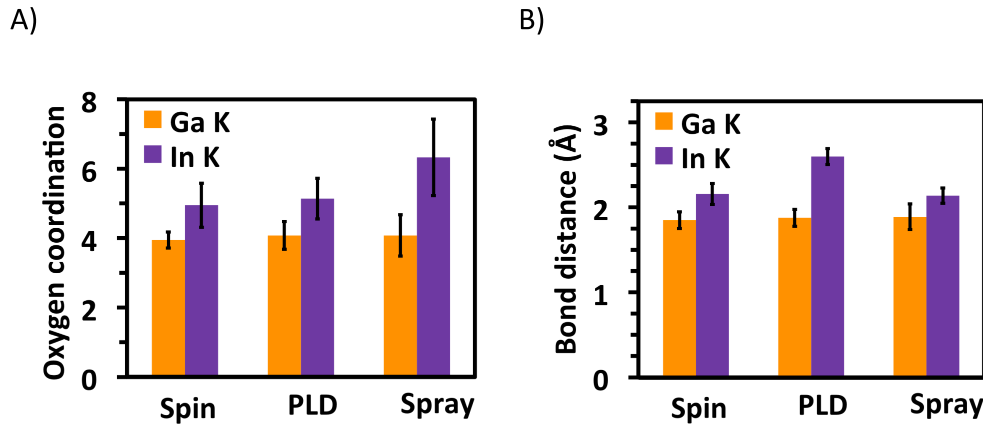

Figure 7.4. Coordination number comparisons from In K-edge and Ga K-edge EXAFS data for PLD films grown at 7.5 mTorr, Spray-CS films grown at 250 °, and Spin-CS films. A) Comparison of M-O coordination. B) Comparison of M-O bond length.

The role of Ga in modulating carrier concentrations is attributed to the high Ga-O binding affinity, with oxygen vacancy-like defects being the primary source of carriers in a-IGO, and previous work suggesting that Ga creates an unfavorable environment for forming these defects. A significant range of V_{on} values, or those of the similar metric, threshold voltage (V_{th}), are reported for a-IGO films deposited via sputtering (-14 to 3.05 V) [41, 133] and solution processing (15.1 to -17)[132, 136, 138-139]. In the present study, PLD devices are found to almost always operate in depletion mode, where V_{on} is negative (Table 7.1). In depletion mode, transistors must be

driven while in the off state. Devices fabricated from IGO18 PLD films are especially conductive, with V_{on} falling below -60 V. Note that spray-CS and Spin-CS films have much higher V_{on} and V_{th} values, with the majority of films having V_{on} no less than -10 V.

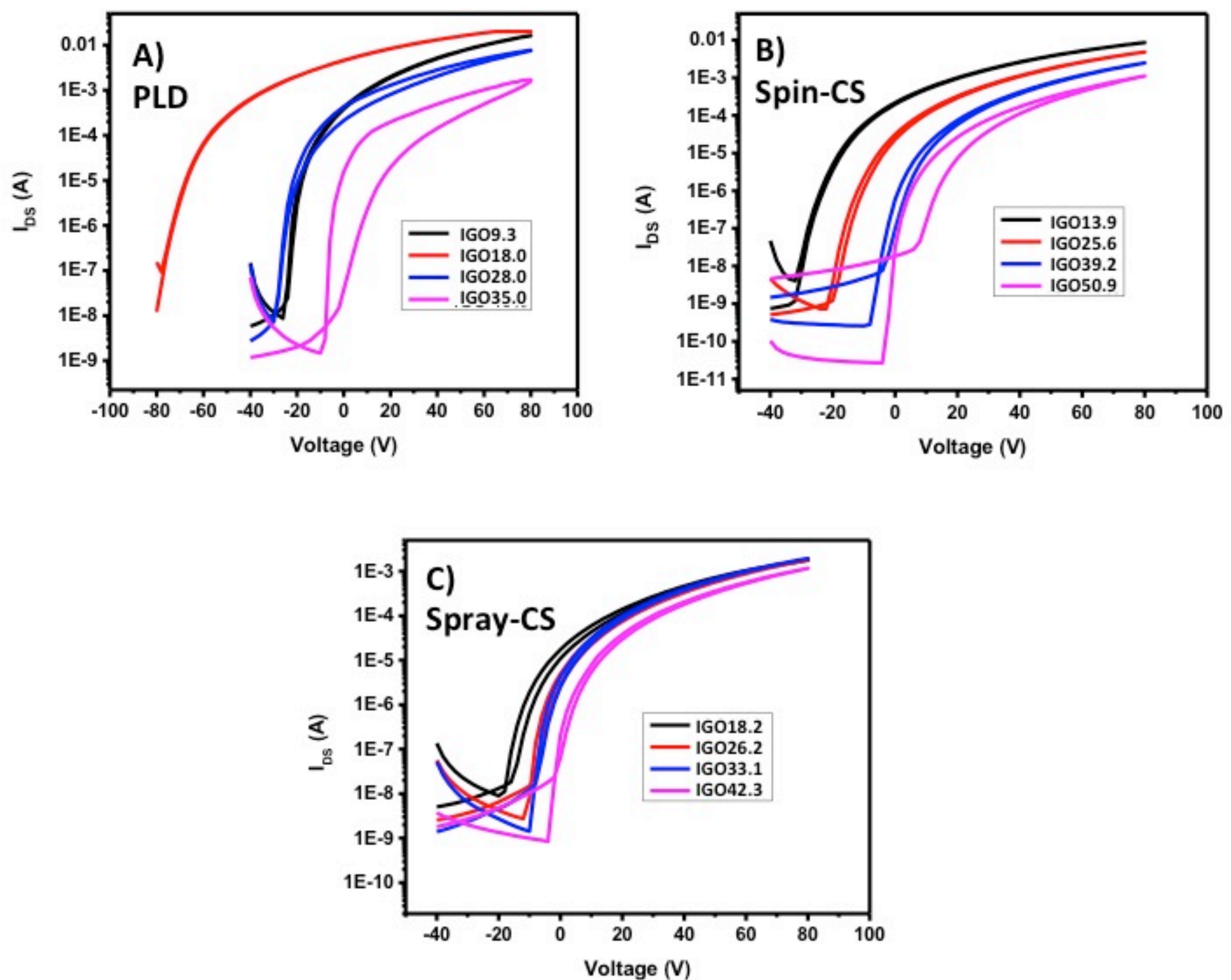

Figure 7.5. Comparison of forward-to-reverse voltage sweep hysteresis observed after 10 voltage sweeps of devices with a-IGO channel layer deposited via A) PLD, B) Spin-CS, and C) Spray-CS.

V_{th} for Spray-CS films suggests that all Spray-CS films operate in enhancement mode where is V_{th} positive. The more positive V_{th} of all Spray-CS, over the Spin-CS and PLD films (Table 7.1), suggests that the Spray-CS processing method is especially effective at reducing the carrier concentrations.[41] The EXAFS analysis in this work (Fig. 7.4) reveals high In-O coordination numbers for the Spray-CS films (Fig. 7.4A), also suggesting that oxygen vacancy-like defects around the In atoms (the source of carriers) are correspondingly low. The fine mist created during Spray-CS presumably enables rapid solvent evaporation and likely, high O_2 exposure to for the metal atoms, leading to dense, well-formed metal-oxygen matrices and a low densities of oxygen vacancy-like defects (i.e., carriers).[128]

Overall the highest performing PLD transistors identified in this study are those fabricated from IGO9.3 films. These devices have the highest average μ_{sat}, reasonable V_{on}, and no visible hysteresis. Note however that output plots of PLD transistors (Fig. 7.6) suggest there may be issues with charge injection in some devices and that Al contacts may not be perfectly ohmic for these devices. Better performance may be achieved with contact optimization.[141] Consistent with similar solution-processed a-IGO studies,[120, 137] the highest performing Spin-CS films are those grown in the 25-40 at% Ga composition range. They consistently display μ_{sat} above average for

solution-processed films (6.67-11.92 cm2 · V -1 · s -1), have limited hysteresis, competitive on/off ratios (106 – 107 V), and positive Vth.

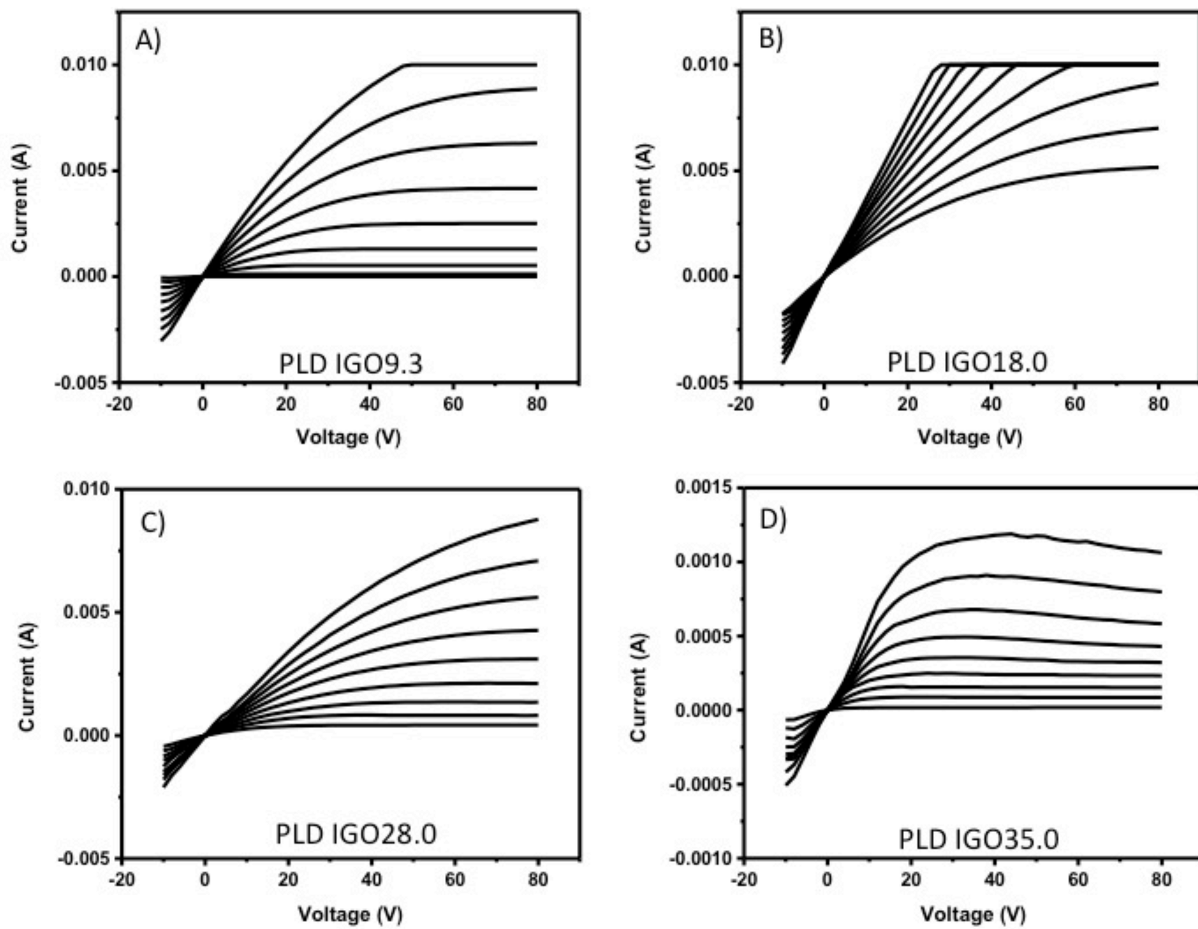

Figure 7.6. PLD output plots for A) 9.3 at% Ga, B) 18.0 at% Ga, C) 28.0 at% Ga, and D) 35.0 at% Ga.

Although slightly underperforming in comparison to Spin-CS devices, Spray-CS devices still display very good device performance for solution processed films.[6] The only metric where

Spray-CS truly underperforms, in comparison to the other processing methods in this work, is μ_{sat}. The significant difference in density for Spray-CS deposited at 300 °C (Figure 2C) vs. at 250 °C (Figure 7B) highlights the strong dependence of Spray-CS films on processing parameters. The Spray-CS method clearly has a much larger optimization space than the Spin-CS technique and is still relatively new. With additional rounds of optimization, Spray-CS films have the potential to perform as well as, or even out-perform Spin-CS-derived films.

7.2.1 Thermal stability

To understand the interplay of deposition method on thermal stability, *in situ* GIXRD measurements were performed during air annealing studies. Films were heated at a constant rate of 2 °C/min, and the crystallization kinetics were sufficiently slow to record multiple 5.5 min diffraction scans during the crystallization of a series of a-IGO films deposited by PLD, Spray-CS, and Spin-CS. From the GIXRD data the crystalline phase fraction could be tracked over time and temperature (Fig. 7.7). The onset of crystallization (T_{onset}) and crystallization temperature (defined as the temperature at which 60% crystallization is achieved) are plotted as a function of Ga content and deposition method (Figure 7.8A). As seen in an *ex situ* study of PLD IGO (chapter 4), the crystallization temperature rises with the addition of the substitutional Ga cation. The results of this study further suggest that the preference of Ga to remain 4-fold

coordinate, in contrast to the surrounding In-O matrix, inhibits the onset of crystallization. EXAFS fits establish that persistence of 4-fold coordinate Ga holds true for all compositions and all processing methods (Fig. 7.4). The short Ga-O bond distances provide additional support for the low Ga-O coordination numbers. From figure 7.8 it is clear the Ga concentration is the dominant factor in determining thermal stability of a-IGO films.

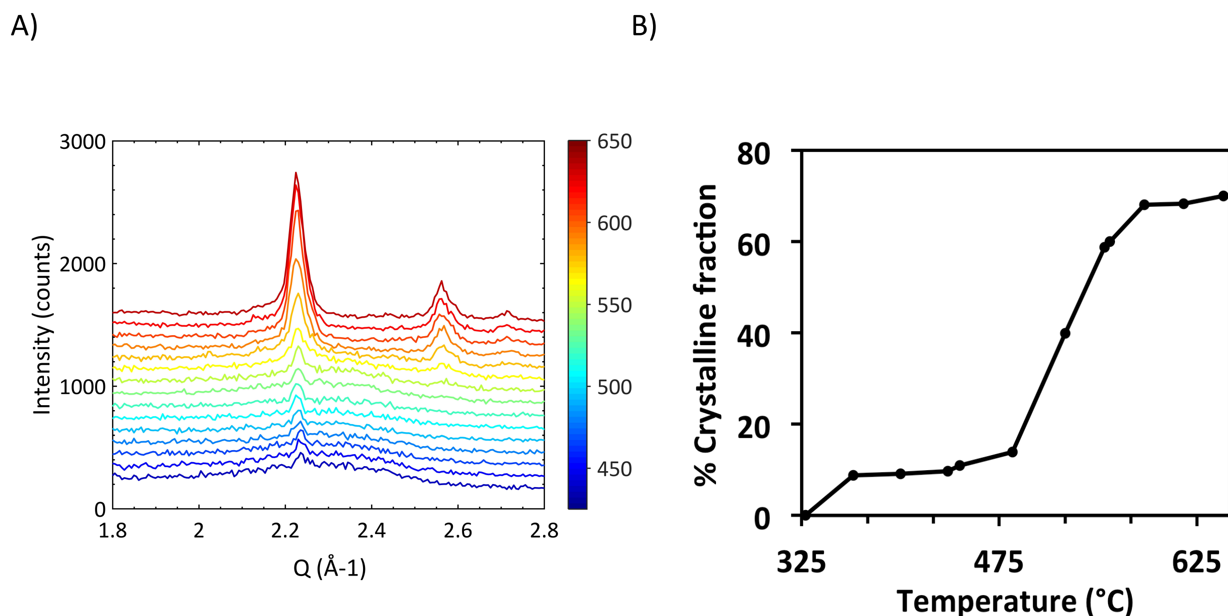

Figure 7.7. A) GIXRD patterns are taken continuously during air annealing. Films are heated inside a graphite dome at a rate of 2 °C per minute. 2θ scans each lasted 5.5 minutes. B) Percent crystalline fraction of Spin-CS IGO17 sample is plotted as a function of median scan temperature.

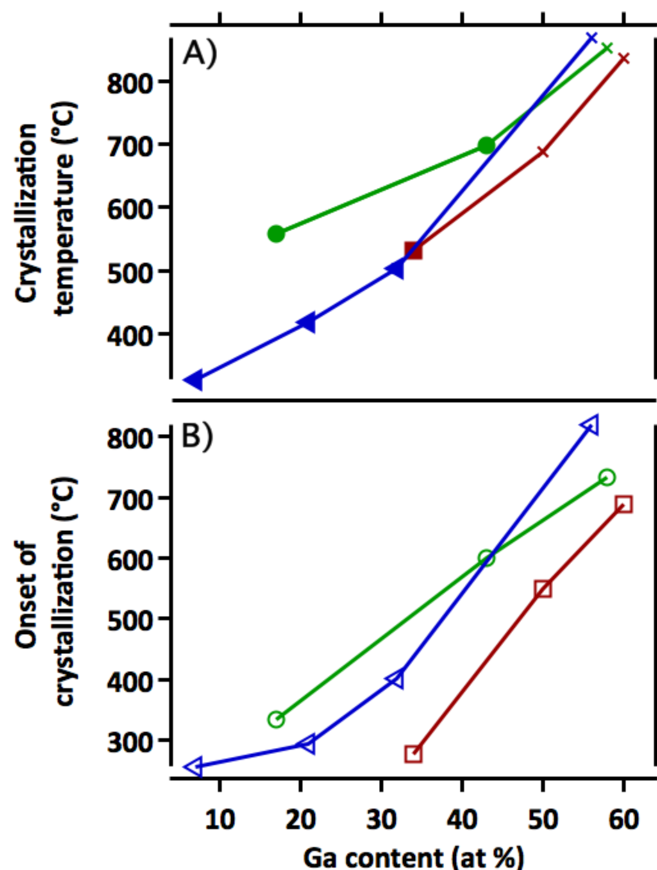

Figure 7.8. A) Crystallization temperature and B) temperature at the onset of crystallization, of spin combustion (green), spray combustion (blue), and PLD (red) a-IGO films as a function of at% Ga. Data points indicated by × in figure A represent those which required extrapolation due to sample deterioration or instrumental temperature limitations.

The PLD films exhibit the lowest thermal stability. The onset of crystallization occurs at lower temperatures than either the Spin- or Spray-CS films; this trend holds true for all a-IGO compositions. A likely reason is that heat is not dissipated in burning off the organic residue remaining in the CS films. XPS studies of Spin- and Spray-CS films reveal residual organic material in the as-deposited CS films,[129, 132] in contrast, PLD takes place in vacuum. XRR scans taken before and after annealing show (Fig. 7.9) the as-deposited PLD films have relatively high

densities. Recent work by Cui *et al.* [142] on a-In-Ga-Zn-O determined that thermal conductivity decreases linearly with film density. Therefore, PLD films may crystallize quickly because they have the highest thermal conductivity. XRR results also reveal that the present as-deposited PLD films are closest in density to their final crystalline density (Fig. 7.C); thus, the structural rearrangement required for PLD films to crystallize may be reduced versus the Spin- and Spray-CS films.

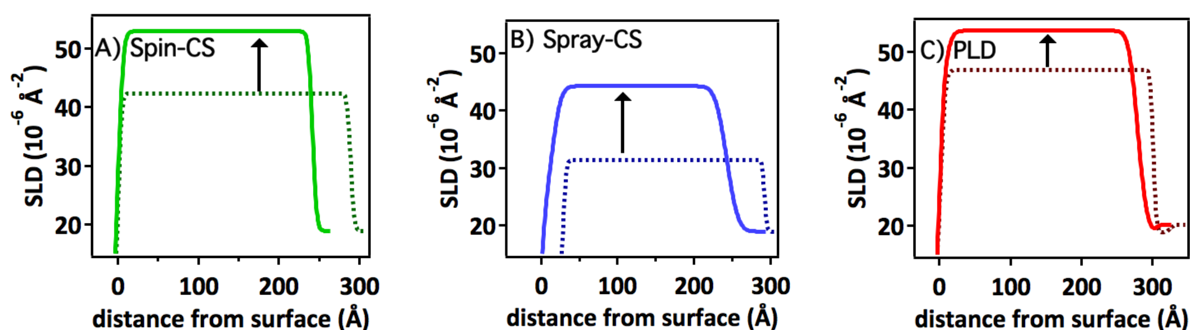

Figure 7.9. Scattering length density showing the increase in density and decrease in thickness from before crystallization (dotted line) to after crystallization (bright line) for a representative Spin-CS (green, A), Spray-CS (blue, B), and PLD (red, C) film.

Spin-CS films exhibit the highest thermal stability below ~45 at% Ga and 600 °C. Previous XPS studies[128] suggest that Spin-CS films may have the highest level of organic content remaining in the film. XRR of thin films also highlights the layered nature of the Spin-CS films (Fig. 7.2C) that results from the layer-by-layer spin coating process (Fig. 7.1C). The presence of

distinct layers in Spin-CS films has been seen previously.[143-144] These layers likely play a role in the crystallization mechanism and may hinder the structural relaxation that takes place upon crystallization.[36] Additionally, the film may act as multiple very thin films, as opposed to a thick film. Very thin films have much slower crystallization rates, due to their higher interface-to-bulk ratio.[145]

For the thermal stability study, all Spray-CS films were grown at 250 °C to ensure these as-deposited films were amorphous. The onset of crystallization was found to occur below 300 °C for films with Ga contents below 22 at% Ga (Fig. 7.8), providing insight into why Spray-CS films deposited for TFTs at 300 °C are crystalline in the low-Ga regime. Spray-CS films initially have lower thermal stability than Spin-CS films but they outperform both Spin-CS and PLD films in the high-Ga, high-temperature regime. Note that unlike the more linear trend in T_{onset} vs. Ga content seen in PLD and Spin-CS films, the thermal stability of Spray-CS films becomes increasingly dependent on Ga content as Ga substitution is increased. Interestingly, the density of the crystalline Spin-CS films is lower than that of both crystalline PLD and crystalline Spin-CS films. Furthermore, the densities of the post-annealed crystalline films (Fig. 7.9B) are essentially identical to the densities of the crystalline-as-grown films (Fig. 7.2C, IGO18). Previous work on the IGO system has shown that In-O coordination number rises during crystallization (chapter 4);

this coordination number increase is due to either structural relaxation[15, 36] (i.e. densification), O_2 uptake into the film, or more likely, a combination of both mechanisms.[27] Since high In-O coordination numbers (Figure 7.4) are already achieved in as-deposited Spray-CS, the level of densification required for crystallization may be reduced.

7.3 Conclusion

PLD, Spin-CS, and Spray-CS processing methods were compared in the a-IGO system across a broad range of Ga substitution. The thermal stability of amorphous oxides was found to be significantly influenced by the processing method. Films grown by combustion processing methods have higher stability than films grown by PLD. For all processing methods, the a-IGO thermal stability can be tuned by controlling the film Ga content. The results of PLD and Spin-CS TFTs suggest that these processing methods are responsive to composition-dependent property tuning, with Spin-CS TFTS showing the clearest and most consistent trends. PLD films were shown to have the highest carrier mobilities, due in part to their superior density. EXAFS and V_{th} measurements of Spray-CS films suggest these films contain high levels of M-O coordination that lowers carrier concentrations.

7.4 Methods

7.4.1 Film and TFT synthesis

Films used for thin film transistors (TFTs) were deposited onto SiO_2/Si substrates purchased from WRS Inc. The SiO_2 layer was confirmed to be 300nm thick and served as the dielectric layer. Films used for the crystallization study were deposited on <100> Si wafers purchased from WaferNet Inc. The single crystal substrate was important for insuring that observation of the amorphous-to-crystalline transition was not obscured by excess background scattering or Bragg peaks. Films used for XAS studies were deposited on quartz substrates. All substrates were ~2 × 2 cm^2. Before film deposition, substrates were sonicated in 200-proof ethanol for 10 min and O_2 plasma cleaned on high for 5 min.

7.4.2 Pulsed laser deposition (PLD)

All pulsed laser depositions employed a 248 nm KrF excimer-laser; the laser was focused to a 1 × 2 mm^2 spot size and used to ablate the ceramic targets, creating a plume of target material. A laser-pulse-duration of 25 ns and a beam energy of 200 mJ/pulse was used. To prevent localized heating, the targets were rotated and the laser beam was rastered radially. Various gallium-to-indium ratios were achieved through alternating ablation between an In_2O_3 target and

a Ga_2O_3 target, both purchased from Super Conducting Materials Inc. Less than 1 monolayer of target material was deposited during each In_2O_3/ Ga_2O_3 cycle to insure mixing at the atomic-layer level.

For TFTs, films were grown at room temperature in a 48.5 ± 0.5 mTorr O_2 environment. O_2 pressure in the deposition chamber was automatically set with feedback from a baratron pressure gauge. A convectron pressure gauge was used to verify the oxygen pressure. A target-to-substrate distance of 60 mm was used. Films were 15-17nm thick. For crystallization studies, films were grown at -25 °C in a 7.5 ± .5 mTorr oxygen environment. A target-to-substrate distance of 10 mm was used. Films were 25-35nm thick.

7.4.3 Combustion synthesis

All reagents where purchased from Sigma Aldrich and used as received. The precursor solutions were prepared with $In(NO_3)_3 \cdot xH_2O$ and $Ga(NO_3)_3 \cdot xH_2O$ salts in 2-methoxythanol to produce 0.05 M solutions. After the salts were completely dissolved, acetylacetone (2:1 ratio of acetylacetone to metal center) and ammonium hydroxide (1:1 ratio of NH_4OH to metal center) where added. The solutions were stirred at room temperature and aged overnight. The precursor

solutions were mixed in the desired ratios and stirred at room temperature for approximately 1-2 hours before use.

7.4.4 Spray combustion synthesis (Spray-CS)

The substrates were heated to 300 ˚C for the duration of the spray coating. For the crystallization and XAS study a lower temperature of 250 ˚C was used to insure all films were amorphous. The precursor solution was sprayed through an ultrasonic nozzle, held 7.5cm above the substrate, at a rate of 0.5 mL/min. The films were then annealed for 1 minute without any additional solution. Total spray time was adjusted to create films with thicknesses of 9-16 nm for TFTs, 30-58 nm for crystallization studies, and 200-400 nm for XAS studies.

7.4.5 Spin combustion synthesis (Spin-CS)

Inside a dry-box (humidity ≈ 23%) the precursor solutions were deposited drop-wise onto clean substrates, using syringes fitted with 0.2μm filters, and spun at 3500 rpm for 30 seconds. After each spin-coated layer, the films were annealed in air for 20 minutes at 300 ˚C. A total of four layers were deposited to create 10 nm thick films for use in TFTs. 14 layers were used to create 30nm thick films for XAS and crystallization studies.

7.4.6 Transistor fabrication and testing

TFTs were fabricated with 10-15 nm thick channel layers deposited by PLD, Spin-CS, and Spray-CS across a range of a-IGO compositions. Precautions were taken to eliminate as many variables between the devices as possible. Transistors were made and tested within weeks of each other in the same laboratory, by the same researcher. All films were grown on the same SiO_2/Si substrates. After deposition, all films were etched with oxalic acid to produce films slightly smaller in area than the shadow mask used for contact deposition. For Spin-CS and Spray-CS, the etched films where annealed at 300 ˚C in low humidity (5%<) for 50 minutes. Aluminum contacts were deposited via thermal evaporation (rate of > 1 Å/s and pressure < 4 x 10^{-6} torr) through shadow masks. The channel geometry had a width (W) of 1 mm and length (L) of 50 μm. Immediately before testing, PLD films were annealed at 300 ˚C in low humidity (5%<) for 45 minutes. The devices were tested in ambient using an Agilent B1500A Semiconductor analyzer.

7.4.7 Film composition

X-ray fluorescence spectroscopy (XRF) was performed on each sample to verify the In/Ga atomic ratio achieved in each film. This measurement was essential since film composition did

not follow the PLD pulse ratios or solution processing precursor ratios; film compositions were always gallium-weighted and pulse/solution ratios had to be adjusted. Note that a similar trend has been observed previously. [137] The Ga K and In L fluorescence yields were corrected for the different absorption cross-sections and detector efficiency (See Supplemental Information, Equation S1).

7.4.8 Crystallization study

In situ grazing incidence X-ray diffraction (GIXRD) was performed to monitor the onset of crystallization in IGO films. Films were heated in air at 2 °C/min with an Anton Paar heating stage fitted with a graphite dome. The 5.5-minute Q-range scans from 1.8-2.8 $Å^{-1}$ were taken continuously during the annealing processes with a Rigaku Smartlab instrument employing a multilayer monochromated Cu rotating anode source and point detector. The incident angle of the 8.04 keV X-ray beam was set at 0.6^{o}. The critical angle for In_2O_3 is 0.37° at this energy. The onset of crystallization was determined by the emergence of a crystalline diffraction peak appearing above the amorphous scattering hump. GIXRD scans depicting the onset of crystallization for each film can be seen in the supplemental information. To track the evolution of crystalline fraction (P_{cryst}), a MATLAB script was used to integrate the area under the

crystalline diffraction peaks (I_c) and the area under the background-subtracted, total scattering pattern (I_{total}). Plots of P_{cryst} versus temperature for each sample are in the supplemental information.

$$P_{cryst} = \frac{I_c}{I_{total}} \tag{7.1}$$

We define crystallization temperature as the point at which each film reached 60% crystallization. To gain more detailed insight into the crystallization kinetics a more rigorous study should be performed employing a 2D detector to quickly sample a larger Q-range.

7.4.9 Structural characterization

XRR was performed using the Rigaku Smartlab instrument described above. Films were fit using the Motofit package.[48] XRR fits revealed the thickness, electron density, and interfacial thickness for each film. Ellipsometry (J. A. Woollam M2000U Ellipsometer) confirmed XRR determined thickness and provided a measurement of films whose thickness was beyond the resolution of the multilayer. GIXRD was performed on each film to establish the amorphous nature of the films.

7.4.10 X-ray absorption spectroscopy (XAS)

X-ray absorption spectroscopy was carried out at the bending magnet 5-BM-D beamline of the DuPont-Northwestern-Dow Collaborative Access Team at the Advanced Photon Source (APS)

of Argonne National Laboratory. XAS data were collected in fluorescence mode at the In and Ga K-edges, respectively, using a 4-element Si-drift detector (Vortex-ME4) with DXP-XMAP electronics (XIA LLC).

Data analysis and extended X-ray absorption fine structure (EXAFS) fitting were done using the iXAFS package.[60] Fittings of the first shell structure were carried out in real space in the R-range of 1.0 – 2.15 Å and 1.0-2.36 Å for the Ga and In K-edges, respectively. The amplitude reduction factors, $S0^2$, of 0.98 for the Ga K-edge and 1.04 for the In K-edge were determined from fits of the two crystalline reference samples (In_2O_3 and Ga_2O_3).

CHAPTER 8: **Conclusions and Future Work**

The study of amorphous oxides was approached from a highly fundamental and collaborative angle. Gallium was explored as a modifying cation in the a-IGO system. Despite the lack of long-range order, structure-property relationships were successfully identified and the role of Ga in the thermal and electrical properties of a-IGO was understood. The combined use of multiple element-specific, local-structure X-ray techniques and MD simulations allowed for unprecedented insight into the influence of Ga substitution. Ga was shown to increase the thermal stability of a-IO, doubling the crystallization temperature with only 8 at% substitution. The strong preference of Ga to maintain 4-fold coordination was exposed as the reason for the increased thermal stability. The structure of the IGO films before and after the crystallization transformation revealed that the change in local structure around Ga upon crystallization is much more significant than the change around In.

The influence of Ga on the carrier concentration was probed in great detail. The high Ga-O binding affinity is often cited as the reason why Ga substitution lowers conductivity. [41, 120, 146] This work demonstrated that Ga polyhedra simply act to dilute the source of carriers, cluster of low-coordinate In-O polyhedra. Ga-O polyhedra are much less likely to be under-coordinates and thus they do not act as a source of carriers. Furthermore, Ga-O polyhedra

inhibit the clustering of the low-coordinate In-O polyhedra, further lowering the carrier concentration. The disruption of Ga-O tetrahedra was also tied to the drop in mobility that follows increased Ga substitution. The Ga tetrahedral disrupt the formation of the conduction matrix and act as a source of traps.

The dominant defect mechanism in a-IZO was explored experimentally through the adaptation of Brouwer analysis to amorphous oxide thin films. This work expanded on the foundational study that applied Brouwer analysis to amorphous oxides, by Adler et al., and the initial experimental study of defects in a-IZO, by Lee et al. The application of *in situ* Brouwer analysis to a-IZO confirmed that oxygen vacancies are the dominant point defect mechanism. The success of this work helps adds Brouwer analysis to the limited number of experimental techniques available for studying defects in amorphous oxides.

The materials science paradigm, processing-structure-properties-performance was accomplished for the a-IGO system. The influence of combustion synthesis (CS) (both Spin-CS and Spray-CS) and pulsed laser deposition (PLD) on the properties, structure, and performance of a-IGO was studied. Comparisons made across the In-Ga composition phase space provided confidence in this assessment. The Ga-dependent trends of increased thermal stability, decreased carrier concentration, and decreased mobility with increased Ga substitution were shown to

persist despite the processing method of the films. Combustion processed films showed greater thermal stability over PLD films as a result of the greater densification CS films undergo upon crystallization. PLD demonstrated the best performing mobility, especially at low Ga concentrations. However, the films made through spin combustion processing showed the most consistency between films. Both PLD and Spin-CS films exhibited multiple Ga-tunable properties including TFT mobility and on-voltage. The Spray–CS films demonstrated low level of carrier in all films. EXFAS fits suggest that the low carrier concentrations are likely as a result of increased oxygen coordination and high metal-oxygen coordination.

8.1 Future Work: Amorphous Oxides for Wearable Thermoelectrics

The emergence of flexible electronics is opening the door to highly biocompatible health sensors. However, most wearable devices available today must be charged externally on a daily basis, limiting their applications.[147] Health monitoring of elderly patients, patients in rural areas, or even wild animals is not compatible with the time and readily available electricity it takes to externally charge a battery. Utilizing energy harvesting technology would allow health sensors to be charged during use. For instance, recent studies have begun exploring the use of wearable thermoelectrics that utilize the body's own thermal energy as a source of power.[147-148]

Thermoelectrics are known for their stability. Their ability to create electricity from thermal gradients in the absence of moving parts means that they can run reliably and quietly.[149] To date, most thermoelectrics research has focused on achieving the best possible figure of merit (ZT).[150] However, high performing thermoelectrics are often made of toxic, brittle materials with costly synthesis routes, which are prohibitive for use in wearable health sensors. Instead, polymer thermoelectrics have largely been explored as potential materials for wearable thermoelectrics. In direct contrast to traditional thermoelectrics, organics have low cost materials that are flexible and can be made cost effectively over large areas. Significant success has been seen in creating p-type organic semiconductors for thermoelectrics, but the challenge of creating suitable n-type polymers has limited the field.[147]

Solution processed n-type oxide semiconductors may provide a solution to the realization of wearable thermoelectrics. The field of transparent conducting oxides has already demonstrated solution-based routes to n-type oxides that are suitable for flexible electronics.[6, 129] Recent studies have begun to explore amorphous oxides as potential thermoelectric materials.[148, 151] Thermoelectrics draw their power from the existence of a thermal gradient; therefore thermoelectric materials need to have low thermal conductivity in order to maintain a temperature gradient. Preliminary work has shown that thermal conductivity of n-type oxide thin

films can be modulated by the nano-scale porosity created during combustion processing (a recent development in solution-processing methods).[45, 142] However, the relationship between processing parameters, film morphology, and film performance is not well understood. By developing a strong understanding of combustion processing, film microstructure can be controlled, resulting in the ability to optimized thermoelectric performance of n-type solution processed oxide for use in wearable health sensors.

Thermoelectrics have the unique ability to turn waste heat back into useful electricity. However, they present a significant materials challenge because their performance relies on competing interactions. The basis of thermoelectric power generation is the Seebeck effect: when a thermal gradient exists across a conducting material, hot electrons diffuse to the cold side and create a buildup of charge and therefore, a voltage across the material. The thermoelectric figure of merit, zT, is a function of the Seebeck coefficient (α), absolute temperature (T), electrical resistivity (ρ), and thermal conductivity (κ).

$$zT = \frac{\alpha^2 T}{\rho\kappa} \tag{8.1}$$

To optimize zT, thermoelectric materials must have a large Seebeck coefficient, low electrical resistivity, and low thermal conductivity, properties that are highly interrelated.[150] Recent work in the field has focused on decoupling electrical and thermal conductivity through

the development of multi-scale structuring. Success of this approach has led to record high zT and resurgence in the field.[149-150, 152] However, these record-setting thermoelectrics materials are not designed for biocompatibility.

Proof of concept health sensors using power generated from wearable thermoelectrics have been tested. Demonstration of small devices has shown that the temperature differential between human skin and the surrounding air is enough to power useful technology. However, the wearable thermoelectrics tested to date are thick (~1-2 cm), making them uncomfortable. Optimal wearable thermoelectrics need to have good thermal contact with skin and be light-weight and flexible to optimize both performance and comfort.[147]

Polymers are a common choice when it comes to flexible, lightweight materials. Building from the knowledge developed in the organic solar cell community, conjugated polymers have been explored as possible thermoelectric materials. Highly ordered and doped materials like PEDOT: Tos and PEDOT:PSS have been demonstrated to have good thermoelectric properties, but only as p-type materials.[147] Full thermoelectric devices consist of both n- and p-type legs connected electrically in series and thermally in parallel. Strong n-type thermoelectric polymers have not yet been seen.[147] A solution to the challenge of highly doped n-type polymers in the

other electronics communities has been to integrate p-type polymers with n-type inorganic materials.[153]

Unlike polymers, oxide semiconductors are easily made with high and tunable n-type carrier concentrations. Amorphous n-type, indium-based oxide semiconductors recently gained attention in the transistor sphere when mobilities upwards of 50 cm^2/Vs were demonstrated in sputtered films grown at room temperature.[2, 4] Low temperature synthesis of these materials opens the door to compatibility with organic materials. Several studies have demonstrated that tuning the oxygen content, either during deposition or in post-deposition annealing, can control carrier concentration through several orders of magnitude.[2, 4, 26-27, 92] Recent work by Fujimoto *et al.*[148] analyzed the thermoelectric potential of amorphous In-Ga-Zn-O (a-IGZO) near room temperature. Their work demonstrated that by controlling carrier concentration, an optimized thermoelectric power factor ($\alpha^2\sigma$) is obtained. The power factor demonstrated by Fujimoto in a-IGZO rivals the top organic-based n-type polymer thermoelectrics. Oxides show promise to outperform polymer thermoelectrics if optimization of thermal conductivity is obtained through control of film microstructure. If the gains seen in other thermoelectric materials are an accurate predictor, thermoelectric performance of amorphous oxides could more than double with precise structure control.[149, 152]

A new method of solution processing, known as combustion processing, shows promise as a cost-effect method for growing oxide materials with multi-scale microstructure. [128] Combustion processing has been explored in a number of oxide materials. [129] The key to combustion processing is to combine in solution an oxidizer (metal nitrate salt) and a fuel (acetylacetone) in order to lower the energy barrier of oxide formation. A metal nitrate-acetylacetone solution is deposited onto a substrate through either spin or spray coating. Upon exposure to heat, local exothermic reactions occur, facilitating the formation of a well-connected metal-oxygen lattice while allowing the temperature of the substrate to remain low. Global substrate temperatures remain low enough for compatibility with plastic substrates. The local combustion reactions release solvent gases that result in the formation of nanoscale porosity. The scale of pore size and the level of film porosity change in response to the deposition conditions of the film (temperature, thickness, etc.).[128] Understanding of how film porosity can be controlled to obtain desired structures has not yet been achieved.

Cross-plane thermal conductivity in a-IGZO films made through combustion processing reveal that a porous oxide microstructure does decrease thermal conductivity.[142] Three a-IGZO films were grown under differing conditions to produce a range of porosity. The thermal conductivity of the films ranged between 0.3 and 1 W/mK, with the most porous film having the

lowest value. Though not explored in the work by Grayson[101] *et al.*, film density also affects electrical mobility in amorphous oxide thin films, with denser films having higher mobility.[40] To use combustion synthesis in the growth of thermoelectric oxides, an intimate knowledge of the relationship between microstructure and properties will be necessary in optimizing the competing interactions of thermal conductivity and electrical conductivity.

The success of combustion processing of oxides for thin film transistor applications provides a strong foundation from which to expand their application to the field of wearable thermoelectrics. Initial studies of combustion processing have demonstrated that tunable microstructure and therefore tunable performance of oxide thin films can be achieved. An in-depth study into the processing parameters which govern microstructure formation in combustion processed films will allow for optimization of solution processed oxides as n-type materials for thermoelectric health sensors.

APPENDIX

Appendix A: Thin Film X-ray Fluorescence Manual

A.1 Introduction

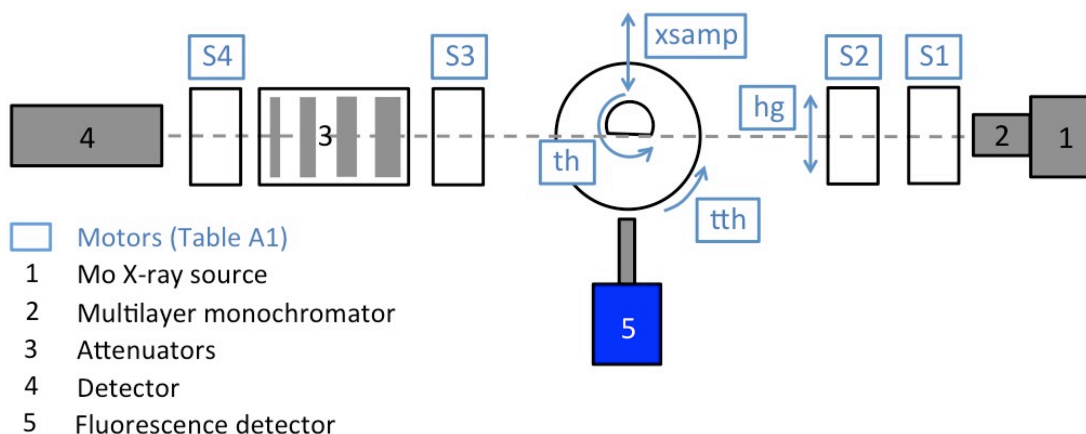

Figure A.1. Diagram of XSW instrument showing the positions of the slit motors (S1, S2, S3, S4), θ/α motor (th), 2θ motor (tth), and z motor (xsamp). The X-ray path is indicated by the grey dashed line.

The XSW two-circle diffractometer in the J. B. Cohen X-ray Diffraction Facility is equipped with a Mo 18-kW rotating anode, collimating multilayer monochromator, and Si drift diode detector making it well suited for performing X-ray fluorescence (XRF) measurements on thin films. This appendix serves as a general guide for setting up the instrument for XRF data acquisition, using the Bedzyk group Matlab script “Sugomat” to fit the data, and applying the necessary data corrections based on sample and measurement geometry. For a more in depth,

step-by-step guide to data acquisition and fitting please see the XSW protocol in the Bedzyk group Google Drive folder.

A.2 Data Acquisition

Table A.1. Basics of SPEC for Mo 18-kW rotating anode 2-circle (XSW) instrument

Two c	Opens SPEC in the terminal
Motor Names	See figure A1 for additional information
xsamp	Moves the sample along the x direction
th	Rotates the sample stage to adjust the theta angle
tth	Rotates the Huber 2-circle axis to adjust the two theta angle
s1hg, s2hg, …	Adjusts the horizontal gap of the indicated slit, slit S1 is closest to X-ray source (units in mm)
s1vg, s2vg, …	Adjusts the vertical gap of the indicated slit (units in mm)
Commands	
cd	Change directory
newfile	Creates a new log file
ct	Count for indicated time (in seconds)
wu	Displays the current positions of all motors
mv	Moves indicated motor to indicated position
umv	Moves indicated motor to indicated position and displays position as it moves
uan	Moves both the tth and th motors in one command
dscan	Scans the indicated motor over the indicated range with the indicated number of steps
set	Resets a motor position to the indicated value
XSW SPEC macro	qdo/home/user18kw/macros/xswdxp_Vortex.mac
setxswdxp	Opens the window for setting up the scan parameters (see Table A2)
xswdxp	Runs the XSW macro

Mount the sample and adjust the straight through beam intensity by employing the pneumatic attenuators (Fig. A1, 3). Perform a half-beam alignment using the xsamp and th motors (See Table A1 and Fig. A1). Move the th motor to the desired incident angle for the XRF measurement. If a reasonable estimate of the sample composition is known, an appropriate incident angle can be determined based on sample thickness and a calculation of the X-ray penetration depth (Eq. 3.5). Otherwise a θ-2θ scan can be performed to determine the critical angle (α_c). For most thin films, 2 or 3 × α_c provides sufficient X-ray penetration. For an optimal beam footprint on thin film samples, the horizontal gap of the slits should be set to 0.05 mm and the vertical gap of the slits should be ~50% the height of the sample.

The fluorescence detector (Vortex-EX Si-drift diode) is positioned orthogonal to the sample plane (Fig. A1) and is mounted on a sliding stage. The sample-to-detector distance is controlled manually and must be optimized. The detector should be close to the sample reduce air absorption however, not so close that the detector deadtime exceeds 10%. The Vortex-EX detector is run through Vortex proprietary software on a Windows XP machine. SPEC communicates with the detector/Windows machine and records fluorescence spectra via the XSW macro. See table A1 for the string to call up the macro. The macro is designed to run X-ray standing wave measurements however, by turning off the unnecessary functionality (Table

A2) it can be used to perform XRF measurements. Data files are recognized by the ".ch0" format.

Table A.2. Parameter settings for using the setxswdxp SPEC macro to perform XRF

a value of 0 turns that parameter off		
Parameter #	**Parameter**	**Example value**
1	Motors that are being scanned	thtth
2	Number of steps	2
3	Turn off this parameter	0
4	Data collection time (s)	60
5	Number of scans	1
6	The value of theta you will collect at (°)	5
7	Step size between scans, set smaller than motor limits for XRF	0.00001
8	Turn off this parameter	0
9	Iterations	1
10	Turn off this parameter	0
11	Turn off this parameter	0
12	Directory where the file will be saved	./ (current directory)
13	File name	SLM94
14	Turn off this parameter	0
15	Title of data	XRF scan of IGO10

A.3 XRF Peak Fitting

The raw data format consists of 3 columns where column 1 is a list of data channels from 1-2048 and columns 2 and 3 both record fluorescence counts. The Si Kα (1.74 keV) and Mo elastic scattering (17.48 keV) peaks can be used as references to convert channel numbers into keV.

After conversion, the X-ray Data Booklet[154] can be used to identify the channel numbers that correspond to the fluorescence lines of interest.

The Bedzyk group Sugomat Matlab script (see Bedzyk group Google Drive folder) can be used to fit XRF data and determine fluorescence net counts for the elements of interest. Table A3 describes the commands that appear in the Matlab GUI. This script is efficient at fitting Gaussian peaks and subtracting background for up to 4 overlapping peaks. Fit quality can be assessed qualitatively through plots of data vs. fit, which appear at the end of the fitting process.

Table A.3. Sugomat Matlab-script commands

Command name	**Description**
nf or Newfile	Starts a new file and prompts for data input scan steps: 2 channels: 2048
ad or SumScans	Combines the data from scan 1 and 2 and begins the fitting process
I2/I1	Intensity ratio between fluorescence peak of interest (1) and a secondary peak (2) which needs to be fit and subtracted
w2/w1	Width ratio between fluorescence peak of interest (1) and a secondary peak (2) which needs to be fit and subtracted
P2-P1	Position of peak of interest (in channel numbers) subtracted from the position of the secondary peak

A.3.1 Photoelectric cross-section and fluorescence yield

The probability of an element undergoing a particular fluorescence emission is determined by the photoelectric cross section and fluorescence yield. The photoelectric cross section is dependent upon the energy of the incident X-ray, the identity of the element, and the origin of the relaxation event (Ch. 3.2.6, Fig. 3.9). The Bedzyk group has complied the necessary constants[54-58] for calculating the photoelectric cross-section and fluorescence yield in the XRF_XSECT Matlab script (Bedzyk group Google Drive folder). Jeffrey Klug wrote the original code in C and Gavin Campbell wrote the MatLab conversion.

A.3.2 Self-absorption

Self-absorption occurs when a fluorescent photon generated in the sample is re-absorbed before reaching the surface. Typically, this correction is unnecessary for thin films. The correction for self-absorption (D) can be calculated for the fluorescence of each element using equation A.1 where μ_{total} is total absorption coefficient and T is the thickness of the thin film sample. μ_l is the portion of the total absorption due to the excitation of the fluorescent level of interest. μ_{total} is the sum of the absorption coefficients for the incident X-rays (μ_i) and the fluorescent X-rays emitted by the element of interest (μ_f). α is the X-ray incident angle (see Fig. 3.4A). The emission angle of fluorescent X-rays is 90° (given the orthogonal position of the fluorescence

detector, Fig. A1) and therefore the *sin* term modifying μ_f is 1. Further details on describing the derivation of self-absorption correction can be seen in work by Pflazer et al.[155]

$$D = \frac{1}{\mu_{total}}(1 - e^{-\mu_{total}T}) \qquad \mu_{total} = (\frac{\mu_i}{\sin\alpha} + \mu_f) \tag{A.1}$$

A.3.3 Air-transmission

One of the benefits of XRF over other composition measurement techniques is that measurements can be performed in air. Though X-rays penetrate air, at long distances and low-energies significant attenuation due to air absorption can occur. Correcting for air transmission is especially important when comparing fluorescence between emission lines far apart in energy. Air-transmission depends on the air pressure, temperature, path length, and fluorescent X-ray energy. Calculations can be done quickly with the use of the CXRO website.[156] For example, transmission of 8 keV X-rays through a path length of 10 cm of air at STP is 100% but at 2 keV it is 78%.

A.3.4 Detector efficiency

As with air-transmission, correcting for detector efficiency is important when comparing fluorescence between emission lines far apart in energy. The efficiency of a Si-drift diode detector varies based on the energy of the fluorescent X-rays. Detector efficiency (F) can be

determined with equation A.2, where T_{Si} is the transmission of X-rays through a Si crystal of thickness equal to the detector crystal (350 µm for Vortex-EX detector) at an energy equal to the fluorescence emission of the element of interest and T_{Be} is transmission factor for Be window (25 µm thick for Vortex-EX). For instance, T_{Si} for In Lα emission (3.3 keV) is negligible (i.e., T≈1) while T_{Si} for Ga Kα emission (9.3 keV) is 0.96. T_{Si} and T_{Be} can be easily calculated using the CXRO website.[156] See CXRO calculation of T_B for a 25 µm thick Be window in Fig. A.2.

$$F = (1 - T_{Si})T_{Be} \quad \text{(A.2)}$$

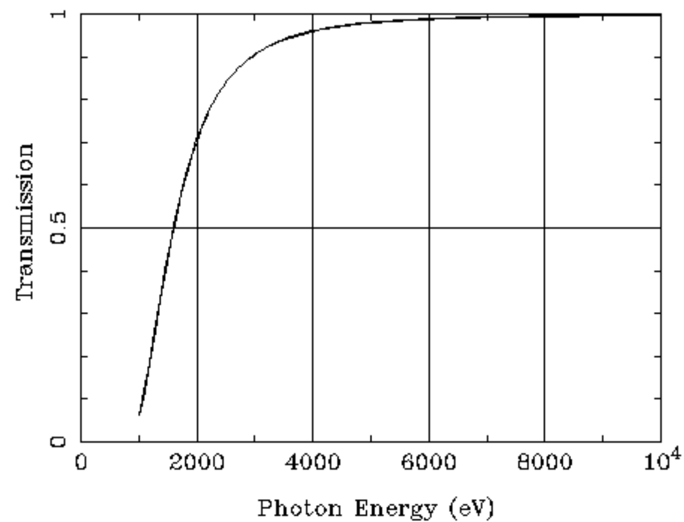

Figure A.2. Calculation of X-ray transmission through a 25 µm Be window (T_{Be}) as a function of X-ray energy. Calculation performed by CXRO website. [156]

A.3.5 Composition from XRF

The following equations combine the above corrections and determine the composition atomic fraction of element A versus B distributed uniformly in a thin film.

$$Y = \frac{B}{C \cdot D \cdot E \cdot F} \qquad G = \frac{Y_A}{Y_A + Y_B} \tag{A.3}$$

Y	Corrected fluorescence yield
B	Measured fluorescence intensity (from Sugomat)
C	Photoelectric cross-section (from XRF_XSECT)
D	Self-absorption
E	Air transmission of fluorescent X-ray
F	Detector efficiency
G	Atomic percent element A

References

1. Hideo Hosono, N. K., Naoyuki Ueda, Hiroshi Kawazoe, Working hypothesis to explore novel wide band gap electrically conducting amorphous oxides and examples. *Journal of Non-Crystalline Solids* **1996,** *198-200*, 165-169.

2. T. Kamiya, K. N., H. Hosono, Present status of amorphous In–Ga–Zn–O thin-film transistors. *Science and Technology of Advanced Materials* **2010,** *11* (4), 044305.

3. Barquinha, P.; Martins, R.; Periera, L.; Fortunato, E., *Transparent Oxide Electronics*. John Wiley & Sons: The Atrium, Southern Gate, Chichester, West Sussex, PO19 8SQ, United Kingdom, 2012; p 295.

4. Kenji Nomura, H. O., Akihiro Takagi, Toshio Kamiya, Masahiro Hirano, and Hideo Hosono, Room-temperature fabrication of transparent flexible thin-film transistors using amorphous oxide semiconductors. *Nature* **2004,** *432*, 488-492.

5. John F. Wager, B. Y., Randy L. Hoffman, Douglas A, Keszler, An amorphous oxide semiconductor thin-film transistor route to oxide electronics. *Current Opinion in Solid State and Materials Science* **2014,** *18*, 53-61.

6. Xinge Yu, T. J. M., Antonio Facchetti, Metal oxides for optoelectronic applications. *Nature Materials* **2016,** *15*, 383.

7. Carsten Schinzer, F. H., Samir F. Matar, Zn3In2O6-crystallographic and electronic structure. *Journal of Materials Chemistry* **1999,** *9*, 1569-1573.

8. Buchholz, D. B.; Zeng, L.; Bedzyk, M. J.; Chang, R. P. H., Differences between amorphous indium oxide thin films. *Progress in Natural Science: Materials International* **2013,** *23*, 475-480.

9. Taylor, M. P.; Readey, D. W.; Teplin, C. W.; Hest, M. F. A. M. v.; Alleman, J. L.; Dabney, M. S.; Gedvilas, L. M.; Keyes, B. M.; To, B.; Perkins, J. D.; Ginley, D. S., The electrical, optical and structural properties of InxZn1−xOy (0 < x < 1) thin films by combinatorial techniques. *Measurement Science and Technology* **2005,** *16* (1), 90-94.

10. Hosono, H., Ionic amorphous oxide semiconductors: Material design, carrier transport, and device application. *Journal of Non-Crystalline Solids* **2006,** *352* (9-20), 851-858.

11. Fortunato, E.; Barquinha, P.; Martins, R., Oxide semiconductor thin-film transistors: a review of recent advances. *Advanced Materials* **2012,** *24* (22), 2945-86.

12. Orcutt, M., Lurking Inside the iPad is the Future of High-Def Displays. *MIT Technology Review* **2013**.

13. Kamiya, T.; Hosono, H., Material characteristics and applications of transparent amorphous oxide semiconductors. *NPG Asia Materials* **2010,** *2* (1), 15-22.

14. Zhu, Q. Physical Properties and Local Structures of Amorphous Zn-Sn-O and Amorphous In-Ga-O FIlms. Northwestern University, Evanston, Illinois, 2013.

15. D. Bruce Buchholz, Q. M., Diego AAlducin, Arturo Ponce, Miguel Jose-Yacaman, Rabi Khanal, Julia E. Medvedeva, Robert P. H. Chang, The Structure and Properties of Amorphous Indium Oxide. *Chemistry of Materials* **2014,** *26*, 5401-5411.

16. Proffit, D. E.; Ma, Q.; Buchholz, D. B.; Chang, R. P. H.; Bedzyk, M. J.; Mason, T. O., Structural and Physical Property Studies of Amorphous Zn-In-Sn-O Thin Films. *Journal of the American Ceramic Society* **2012,** *95* (11), 3657-3664.

17. Adler, A. U. Defect Analysis of the In-Ga-Zn-O System for Transparent Oxide Semiconductor Applications. Northwestern University, Evanston, IL, 2013.

18. Exarhos, G. J.; Zhou, X.-D., Discovery-based design of transparent conducting oxide films. *Thin Solid Films* **2007,** *515* (18), 7025-7052.

19. Luo, J.; Adler, A. U.; Mason, T. O.; Bruce Buchholz, D.; Chang, R. P. H.; Grayson, M., Transient photoresponse in amorphous In-Ga-Zn-O thin films under stretched exponential analysis. *Journal of Applied Physics* **2013,** *113* (15), 153709.

20. Barquinha, P.; Pereira, L.; Gonçalves, G.; Martins, R.; Fortunato, E., Toward High-Performance Amorphous GIZO TFTs. *Journal of The Electrochemical Society* **2009,** *156*, H161.

21. Kim, H.-S.; Park, K.-B.; Son, K. S.; Park, J. S.; Maeng, W.-J.; Kim, T. S.; Lee, K.-H.; Kim, E. S.; Lee, J.; Suh, J.; Seon, J.-B.; Ryu, M. K.; Lee, S. Y.; Lee, K.; Im, S., The influence of sputtering power and O2/Ar flow ratio on the performance and stability of Hf–In–Zn–O thin film transistors under illumination. *Applied Physics Letters* **2010,** *97* (10), 102103.

22. Kamiya, T.; Nomura, K.; Hirano, M.; Hosono, H., Electronic structure of oxygen deficient amorphous oxide semiconductor a-InGaZnO4-x: Optical analyses and first-principle calculations. *Physica Status Solidi (C) Current Topics in Solid State Physics* **2008,** *5* (9), 3098-3100.

23. Leenheer, A.; Perkins, J.; van Hest, M.; Berry, J.; O'Hayre, R.; Ginley, D. S., General mobility and carrier concentration relationship in transparent amorphous indium zinc oxide films. *Physical Review B* **2008,** *77* (11), 115215.

24. Perkins, J. D.; Hest, M. F. a. M. V.; Taylor, M. P.; Ginley, D. S., Conductivity and transparency in amorphous In-Zn-O transparent conductors. *International Journal of Nanotechnology* **2009,** *6* (9), 850.

25. Shigesato, Y.; Paine, D. C., Study of the effect of Sn doping on the electronic transport properties of thin film indium oxide. *Applied Physics Letters* **1993,** *62* (11), 1268-1270.
26. S. Lee, D. C. P., Identification of the native defect doping mechanism in amorphous indium zinc oxide thin films studied using ultra high pressure oxidation. *Applied Physics Letters* **2013,** *102* (5), 052101.
27. Adler, A. U.; Yeh, T. C.; Bruce Buchholz, D.; Chang, R. P. H.; Mason, T. O., Quasi-reversible point defect relaxation in amorphous In-Ga-Zn-O thin films by in situ electrical measurements. *Applied Physics Letters* **2013,** *102* (12), 122103.
28. Brouwer, G., A General Asymptotic Solution of Reaction Equations Common in Solid-State Chemistry. *Philips Reearch. Reports* **1954,** *9*, 366-376.
29. J. H. W. De Wit, G. V. U., and M. Lahey, Electron Concentration and Mobility in In2O3. *Journal of Physics and Chemistry of Solids* **1977,** *38*, 819-824.
30. S. Lany, A. Z., T. O. Mason, J. F. Wager, K. R. Poeppelmeir, J. D. Perkins, J. J. Berry, D. S. Ginley, A. Zunger, Surface Origin of High Conductivities in Undoped In2O3 Thin Films. *Physical Review Letters* **2012,** *108*, 016802.
31. Altynbek Murat, A. U. A., Thomas O. Mason, Julia E. Medvedeva, Carrier Generation in Multicomponent Wide-Bandgap Oxides: InGaZnO4. *Journal of the American Chemical Society* **2013,** *135*, 5685-5692.
32. Y. S. Jung, J. Y. S., D. W. Lee, and D. Y. Jeon, Influence of DC magnetron sputtering parameters on the properties of amorphous indium zinc oxide thin film. *Thin Solid Films* **2003,** *445* (1), 63-71.
33. Taylor, M. P.; Readey, D. W.; van Hest, M. F. A. M.; Teplin, C. W.; Alleman, J. L.; Dabney, M. S.; Gedvilas, L. M.; Keyes, B. M.; To, B.; Perkins, J. D.; Ginley, D. S., The Remarkable Thermal Stability of Amorphous In-Zn-O Transparent Conductors. *Advanced Functional Materials* **2008,** *18* (20), 3169-3178.
34. Diana E. Proffitt, T. P., Jonathon D. Emery, Qing Ma, D. Bruce Buchholz, Peter W. Voorhees, Michael J. Bedzyk, Robert P. H. Chang, Thomas O. Mason, Thermal stability of amorphous Zn-In-Sn-O films. *Journal of Electroceramics* **2015,** *34*, 167-174.
35. Ide, K.; Nomura, K.; Hiramatsu, H.; Kamiya, T.; Hosono, H., Structural relaxation in amorphous oxide semiconductor, a-In-Ga-Zn-O. *Journal of Applied Physics* **2012,** *111* (7), 073513.
36. Moghadam, M. M.; Li, R.; Buchholz, D. B.; Li, Q.; Voorhees, P. W.; Dravid, V. P., In Situ Crystallization and Morphological Evolution in Multicomponent Indium Oxide Thin Films. *Crystal Growth and Design* **2017,** *17*, 1396-1403.

37. Pung Keun Song, H. A., Masayuki Kamei, Yuzo Shigesato, Itaru Yasui, Preparation and Crystallizatoin of Tin-doped and Undoped Amorphous Indium Oxide Films Deposited by Sputtering. *Japanese Journal of Applied Physics* **1999,** *38*, 5224-5226.
38. Yaglioglu, B.; Yeom, H.-Y.; Paine, D. C., Crystallization of amorphous In2O3–10 wt % ZnO thin films annealed in air. *Applied Physics Letters* **2005,** *86* (26), 261908.
39. Qimin Zhu, Q. M., D. Bruce Buchholz, Robert P. H. Chang, Michael J. Bedzyk, Thomas, O. Mason, Structural and physical properties of transparent conducting, amorphous Zn-doped SnO2 films. *Journal of Applied Physics* **2014,** *115*, 033512.
40. Jeremy Smith, L. Z., Rabi Khanal, Katie Stallings, Antonio Facchetti, Julia E, Medvedeva, Michael J. Bedzyk, Tobin J. Marks, Cation size effects on the electronic and structural properties of solution-processed In-X-O thin films. *Advanced Electronic Materials* **2015,** *7*, 1500146.
41. Chiang, H. Q.; Hong, D.; Hung, C. M.; Presley, R. E.; Wager, J. F.; Park, C. H.; Keszler, D. A.; Herman, G. S., Thin-film transistors with amorphous indium gallium oxide channel layers. *Journal of Vacuum Science & Technology B: Microelectronics and Nanometer Structures* **2006,** *24* (6), 2702.
42. Ohring, M., *Materials Science of Thin Films Deposition and Structure*. Academic Press: Hoboken, NJ, USA, 2002.
43. Hennek, J. W.; Kim, M.-G.; Kanatzidis, M. G.; Facchetti, A.; Marks, T. J., Exploratory combustion synthesis: amorphous indium yttrium oxide for thin-film transistors. *Journal of the American Chemical Society* **2012,** *134*, 9593-6.
44. Kim, M.-G.; Kanatzidis, M. G.; Facchetti, A.; Marks, T. J., Low-temperature fabrication of high-performance metal oxide thin-film electronics via combustion processing. *Nature Materials* **2011,** *10* (5), 382-8.
45. Jonathon W. Hennek, J. S., Aiming Yan, Myung-Gil Kim, Wei Zhao, Vinayak P. Dravid, Antonio Facchetti, and Tobin J. Marks, Oxygen "Getter" Effects on Microstructure and Carrier Transport in Low Temperature Conbustion-Processed a-InXZnO (X = Ga, Sc, Y, La) Transistors. *Journal of the American Chemical Society* **2013,** *135*, 10729-10741.
46. McMorrow, D.; Als-Nielson, J., *Elements of Modern X-ray Physics*. 2 ed.; John Wiley & Sons: The Atrium, Southern Gate, Chichester, West Sussex, PO19 8SQ, United Kingdom, 2011; p 419.
47. Que, L., *Physical Methods in Bioinorganic Chemistry Spectrscopy and Magnetism*. University Science Books: Sausalito, CA, USA, 2000.

48. Nelson, A., Co-refinement of multiple-contrast neutron/X-ray reflectivity data using MOTOFIT. *Journal of Applied Crystallography* **2006,** *39* (2), Journal of Applied Crystallography.

49. Parratt, L. G., Surface studies of solids by total reflection of x-rays. *Physical Review* **1954,** *95* (2), 359-369.

50. Ashcroft, D. N.; Mermin, N. W., *Solid State Physics*. Brooks/Cole Cengage Learning: Belmont, CA, USA, 1976; p 826.

51. Parthiban, S.; Kwon, J.-Y., Role of dopants as a carrier suppressor and strong oxygen binder in amorphous indium-oxide-based field effect transistor. *Journal of Materials Research* **2014,** *29* (15), 1585-1596.

52. Aiming Yan, T. S., Konstantin B. Borisenko, D. Bruce Buchholz, Robert P. H. Chang, Angus I. Kirkland, and Vinayak P. Dravid, Multi-scale order in amorphous transparent oxide thin films. *Journal of Applied Physics* **2012,** *112*, 054907.

53. Sunho Jeong, Y.-G. H., Jooho Moon, Antonio Facchetti, Tobin J. Marks, The Role of Gallium Doping in Dramatically Lowering Amorphous-Oxide Procedding Termperatures for Solution-Derived Indium Zinc Oxide Thin-Film Transistors. *Advanced Materials* **2010,** *22*, 1346-1350.

54. Scofield, J. H., Exchange corrections of K X-ray emission rates. *Physical Review A* **1974,** *9*, 1041.

55. D. A. Close, R. C. B., J. J Malanify, and C. J. Umbarger, Yield Ratios, Kalpha/Kbeta, Lalpha/Lbeta, Lalpha/Lgamma, and Lalpha/Ll, for X Rays Produced by Protons of 1.0 to 3.7 MeV. *Physical Review A* **1973,** *8*, 1973.

56. S. Puri, D. M., B. Chand, Nirmal Singh, J. H. Hubbell, P. N. Trehan, Production of L_i subshell and M shell vacancies following inner-shell vacancy production. *Nuclear Instruments and Methods in Physics Research Section B: Beam Interactions with Materials and Atoms* **1993,** *83* (1-2), 21-30.

57. J. L. Campbell, J.-X. W., Interpolated Dirac-Fock values of L-subshell x-ray emission rates including overlap and exchange effects. *Atomic Data and Nuclear Data Tables* **1989,** *43* (2), 281-291.

58. S. Puri, D. M., B. Chand, Nirmal Singh, P. N. Trehan, L shell fluorescence yields and coster—kronig transition probabilities for the elements with $25 < Z < 96$. *X-ray Spectrometry* **1993,** *22* (5), 358-361.

59. P. H Fuoss, P. E., W. K. Warburton, A. Bienenstock, Application of Differential Anomalous X-Ray Scattering to Structure Studies of Amorphous Materials. *Physical Review Letters* **1981,** *46* (23), 1537.

60. B. Ravel, M. N., ATHENA, ARTEMIS, HEPHAESTUS: data analysis for X-ray absorption spectroscopy using IFEFFIT. *Journal of Synchrotron Research* **2005,** *12*, 537-541.

61. H. Klug, L. A., *X-ray Diffraction Procedures: For Polycrystalline and Amorphous Materials*. John Wiley: New York, NY, USA, 1974.

62. D. Waasmaier, A. K., New Analytical Scattering-Factor for Free Atoms and Ions. *Acta Crystallographica* **1994,** *A51*, 416-431.

63. Alexandropolos, N. G.; Cooper, M. J.; Suortti, P.; Willis, B. T. M., International Tables for Crystallography. John Wiley & Sons: Hoboken, New Jersey, 2006.

64. G Kresse, J. F., Efficiency of ab-initio total energy calculations for metals and semiconductors using a plane-wave basis set. *Computational Materials Science* **1996,** *6*, 15-50.

65. G Kresse, J. F., Efficient iterative schemes for ab initio total-energy calculations using plane-wave basis set. *Physical Review B* **1996,** *54* (16), 11169.

66. G. Kresse, J. H., Ab initio molecular dynamics for liquid metals. *Physical Review B* **1993,** *47* (1), 558.

67. G. Kresse, J. H., Ab initio molecular-dynamics simulations of the liquid-metal-amorphous-semmiconductor transition in germanium. *Physical Review B* **1994,** *49* (20), 14251.

68. Hohenberg, P.; Kohn, W., Inhomogeneous Electron Gas. *Physical Review* **1964,** *136* (3B), B864.

69. W. Khon, L. J. S., Self-Consistant Equations Including Exchange and Correlation Effects. *Physical Review B* **1965,** *140* (4A), A1133.

70. John P. Perdew, K. B., Matthias Ernzerhof, Generalized Gradient Approximation Made Simple. *Physical Review Letters* **1996,** *77* (18), 3865.

71. John P. Perdew, K. B., Matthias Ernzerhof, Errata: Generalized Gradient Approximation Made Simple. *Physical Review Letters* **1996,** *78* (7), 1396.

72. Blochl, P. E., Projector augmented-wave method. *Physical Review B* **1994,** *50* (24), 17953.

73. G. Kresse, D. J., From ultrasoft pseudipotentials to the projector augmented-wave method. *Physical Review B* **1999,** *59* (3), 1758.

74. Hoppe, R., The Coordination Number - an Inorganic Chameleon. *Angewandte Chemie International Edition* **1970,** *9* (1), 25.

75. Rudolf Hoppe, S. V., Holger Glaum, Jurgen Kissel, Hans Peter Muller, Kirsten Bernet, A new route to charge distributions in ionic solids. *Journal of the Less-Common Metals* **1989,** *156*, 105-122.

76. Rabi Khanal, D. B. B., Robert P. H. Chang, Julia E. Medvedeva, Composition-deoendent structural and transport properties of amorphous transparent conducting oxides. *Physical Review B* **2015,** *91*, 205203.

77. Koichi Momma, F. I., VESTA 3 for three-dimensional visualiztion of crystal, volumetric and morphology data. *Journal Applied Cryst.* **2011,** *44*, 1272-1276.

78. Heyd, J.; Scuseria, G. E.; Ernzerhof, M., Hybrid functionals based on a screened Coulomb potential. *The Journal of Chemical Physics* **2003,** *118* (18), 8207-8215.

79. Heyd, J.; Peralta, J. E.; Scuseria, G. E.; Martin, R. L., Energy band gaps and lattice parameters evaluated with the Heyd-Scuseria-Ernzerhof screened hybrid functional. *The Journal of Chemical Physics* **2005,** *123* (17), 174101.

80. Ramzan, M.; Kaewmaraya, T.; Ahuja, R., Molecular dynamics study of amorphous Ga-doped In2O3: A promising material for phase change memory devices. *Applied Physics Letters* **2013,** *103* (7), 072113.

81. Marezio, M., Refinement of the Crystal Structure of In2O3 at two Wavelengths. *Acat Crystallographica* **1965,** *20*, 723.

82. Geller, S., Crystal Structure of β-Ga2O3. *The Journal of Chemical Physics* **1960,** *33* (3), 676-684.

83. Pauling, L., The Principles Determining the Structure of Complex Ionic Crystals. *Journal of the American Chemical Society* **1929,** *51*, 1010-1026.

84. Utsuno, F.; Inoue, H.; Shimane, Y.; Shibuya, T.; Yano, K.; Inoue, K.; Hirosawa, I.; Sato, M.; Honma, T., A structural study of amorphous In2O3–ZnO films by grazing incidence X-ray scattering (GIXS) with synchrotron radiation. *Thin Solid Films* **2008,** *516* (17), 5818-5821.

85. Hoel, Cathleen A.; Xie, S.; Benmore, C.; Malliakas, Christos D.; Gaillard, J.-F.; Poeppelmeier, Kenneth R., Evidence for Tetrahedral Zinc in Amorphous In2-2xZnxSnxO3 (a-ZITO). *Zeitschrift für anorganische und allgemeine Chemie* **2011,** *637* (7-8), 885-894.

86. Doreen D. Edwards, P. E. F., Thomas O., Phase Equilibria in the Ga2O3-In2O3 System. *Journal of the American Ceramics Society* **1997,** *80*, 253-7.

87. Medvedeva, J. E.; Khanal, R., Long-range structural correlations in amorphous ternary In-based oxides. *Vacuum* **2015,** *114*, 142-149.

88. A. Takagi, K. N., H. Ohta, H. Yanagi, T. Kamiya, M. Hirano, Carrier transport and electronic structure in amorphous oxide semiconductor, a-InGaZnO4. *Thin Solid Films* **2005,** *486*, 38-41.
89. Divya, R. P., Deepak, Recurring polyhedral motifs in the amorphous indium gallium zinc oxide network. *physica status solidi (a)* **2017,** (1600471), 1-10.
90. Simon J. L. Billinnge, M. G. K., Beyond crystallography: the study of disorder, nanocrystllinity, and crsytallographically challenged materials with pair-distrubution functions. *Chemical Communications* **2004**, 749-760.
91. Kamiya, T.; Nomura, K.; Hosono, H., Subgap states, doping and defect formation energies in amorphous oxide semiconductor a-InGaZnO4 studied by density functional theory. *physica status solidi (a)* **2010,** *207* (7), 1698-1703.
92. Stephanie L. Moffitt, A. U. A., Thomas Gennett, David S. Ginley, John D. Perkins, and Thomas O. Mason, Confirmation of the Dominant Defect Mechanism in Amorphous In-Zn-O Through the Application of In Situ Brouwer Analysis. *Journal of the American Ceramics Society* **2015,** *98*, 2099.
93. Hye-Ri Kim, J. P., Sung-Hun Lee, Gun-Hwan Lee, Pung-Geun Song, Yong-Cheol Kang, Dong-Ho Kim, Effects of Ga Concentration on ELectrical and Physical Properties of Amorphous Ga-Zn-Sn-O Semiconductor Thin Films. *Electrochemical and Solid-State Letters* **2011,** *14* (10), H411-H414.
94. Kim, M.-H.; Choi, M.-J.; Kimura, K.; Kobayashi, H.; Choi, D.-K., Improvement of the positive bias stability of a-IGZO TFTs by the HCN treatment. *Solid-State Electronics* **2016,** *126*, 87-91.
95. Kim, Y. G.; Kim, T.; Avis, C.; Lee, S.-H.; Jang, J., Stable and High-Performance Indium Oxide Thin-Film Transistor by Ga Doping. *IEEE Transactions on Electron Devices* **2016,** *63* (3), 1078-1084.
96. Kamiya, T.; Nomura, K.; Hosono, H., Origin of definite Hall voltage and positive slope in mobility-donor density relation in disordered oxide semiconductors. *Applied Physics Letters* **2010,** *96* (12), 122103.
97. W. Chr. Germs, W. H. A., A. K. Tripathi, W. S. C. Roelofs, B. Cobb, R. A. J. Janssen, G. H. Gelinck, M. Kemerink, Charge transport in amorphous InGaZnO thin-film transistors. *Physical Review B* **2012,** *86*, 155319.
98. Bubel, S.; Chabinyc, M. L., Model for determination of mid-gap states in amorphous metal oxides from thin film transistors. *Journal of Applied Physics* **2013,** *113* (23), 234507.

99. Po-Yung Liao, T.-C. C., Tien-Yu Hsieh, Ming-Yen Tsai, Bo-Wei Chen, Yi-Hsien Tu, Ann-Kuo Chu, Cheng-Hsu Chou, Jung-Fang Chang, Investigation of carrier transport behavior in amorphous indium-gallium-zinc oxide thin film transistors. *Japanese Journal of Applied Physics* **2015,** *54*, 094101.

100. Bhoolokam, A.; Nag, M.; Steudel, S.; Genoe, J.; Gelinck, G.; Kadashcuk, A.; Groeseneken, G.; Heremans, P., Conduction mechanism in amorphous InGaZnO thin film transistors. *Japanese Journal of Applied Physics* **2016,** *55*, 014301.

101. I. I. Fishchuk, A. K., A. Bhooklam, A. de Jamblinne de Meux, G. Pourtois, M. M. Gavrilyuk, A. Kohler, H. Bassler, P. Heremans, J. Genoe, Interplay between hopping and band transport in high-mobility disordered semiconductors at large carrier concentrations: The case of the amorphous oxide InGaZnO. *Physical Review B* **2016,** *93*, 195204.

102. Toshio Kamiya, K. N., Hideo Hosono, Electronic structure of the amorphous oxide semiconductor a-InGaZnO4-x: Tauc-Lorentz optical model and origins of subgap states. *physica status solidi (a)* **2009,** *206* (5), 860-867.

103. P. Charton, P. A., X-ray absorption and Raman characterizations of TeO2-Ga2O3 glasses. *Journal of Non-Crystalline Solids* **2004,** *333*, 307-15.

104. B. Ryu, H. K. Noh, E. A. Choi, K. J. Chang, O-vacancy as the origin of negative bias illumination stress instability in amorphous In-Ga-Zn-O thin film transistors. *Applied Physics Letters* **2010,** *97*, 1-4.

105. L. Nagarajan, R. A. De Souza, D. Samuels, I. Valov, A. Borger, J. Janek, K.-D. Becker, P. C. Schmidt, M. Martin, A chemically driven insulator-metal transition in non-stoichiometric and amorphous gallium oxide. *Nature Materials* **2008,** *7*, 391-398.

106. B. G. Streetman, S. B., *Solid State Electronic Devices*. 5 ed.; Prentice Hall Inc. : Upper Saddle River, NJ, USA, 2000.

107. M. Orita, H. O., M. Hirano, S. Narushima, H, Hosono, Amorphous transparent conductive oxide InGaO3(ZnO)m (M<4): a Zn 4s conductor. *Philiosophical Magazine B* **2001,** *81* (5), 501-515.

108. Park, J. S.; Maeng, W.-J.; Kim, H.-S.; Park, J.-S., Review of recent developments in amorphous oxide semiconductor thin-film transistor devices. *Thin Solid Films* **2012,** *520* (6), 1679-1693.

109. S. Lee, D. C. Paine, On the efect of Ti on the stability of amrophous indium zinc oxide used in thin film transistor applications. *Applied Physics Letters* **2011,** *98*, 262108.

110. Yamazoe, N.; Shimanoe, K., Theory of power laws for semiconductor gas sensors. *Sensors and Actuators B: Chemical* **2008,** *128* (2), 566-573.

111. M. J. Madou, S. R. M., *Chemical Sensing with Solid State Devices*. Academic Press: San Diego, CA, USA, 1989.

112. Singh, N.; Ponzoni, A.; Comini, E.; Lee, P. S., Chemical sensing investigations on Zn–In2O3 nanowires. *Sensors and Actuators B: Chemical* **2012,** *171-172*, 244-248.

113. Yang, D. J.; Whitfield, G. C.; Cho, N. G.; Cho, P.-S.; Kim, I.-D.; Saltsburg, H. M.; Tuller, H. L., Amorphous InGaZnO4 films: Gas sensor response and stability. *Sensors and Actuators B: Chemical* **2012,** *171-172*, 1166-1171.

114.Yang, S.; Bak, J. Y.; Yoon, S.-m.; Ryu, M. K.; Oh, H.; Hwang, C.-s.; Kim, G. H.; Park, S.-h. K.; Jang, J., Low-Temperature Processed Flexible In-Ga-Zn-O Thin-Film Transistors Exhibiting High Electrical Performance. *IEEE Electron Device Letters* **2011,** *32* (12), 1692-1694.

115. Kim, Y.-H.; Heo, J.-S.; Kim, T.-H.; Park, S.; Yoon, M.-H.; Kim, J.; Oh, M. S.; Yi, G.-R.; Noh, Y.-Y.; Park, S. K., Flexible metal-oxide devices made by room-temperature photochemical activation of sol–gel films. *Nature* **2012,** *489* (7414), 128-132.

116. Bao, Z.; Chen, X., Flexible and Stretchable Devices. *Advanced Materials* **2016,** *28*, 4177-7179.

117. Trung, T. Q.; Lee, N. E., Flexible and Stretchable Physical Sensor Integrated Platforms for Wearable Human-Activity Monitoringand Personal Healthcare. *Advanced Materials* **2016,** *28*, 4338-4372.

118. Petti, L.; Munzenrieder, N.; Vogt, C.; Faber, H.; Buthe, L.; Cantarella, G.; Bottacchi, F.; Anthopoulos, T. D.; Troster, G., Metal oxide semiconductor thin-film transistors for flexible electronics. *Applied Physics Reviews* **2016,** *3*, 021303.

119. Ahn, B. D.; Jeon, H.-J.; Sheng, J.; Park, J.; Park, J.-S., A review on the recent developments of solution processes for oxide thin film transistors. *Semiconductor Science and Technology* **2015,** *30*, 064001.

120. Choi, C.-H.; Su, Y.-W.; Lin, L.-Y.; Cheng, C.-C.; Chang, C.-h., The effects of gallium on solution-derived indium oxide-based thin film transistors manufactured on display glass. *RSC Advances* **2015,** *5*, 93779-93785.

121. Park, J. H.; Yoo, Y. B.; Lee, K. H.; Han, S. W.; Choi, W. J.; Baik, H. K., Effect of acetic acid on the performance of solution-processed gallium doped indium oxide thin film transistors. *Journal of Sol-Gel Science and Technology* **2013,** *67*, 130-134.

122. Kim, H. S.; Byrne, P. D.; Facchetti, A.; Marks, T. J., High Performance Solution-Processed Indium Oxide Thin-Film Transistors. *Journal of the American Chemical Society* **2008,** *130* (38), 12580-12581.

123. Jeong, S.; Lee, J.-Y.; Lee, S. S.; Seo, Y.-H.; Kim, S.-Y.; Park, J.-U.; Ryu, B.-H.; Yang, W.; Moon, J.; Choi, Y., Metal salt-derived In–Ga–Zn–O semiconductors incorporating formamide as a novel co-solvent for producing solution-processed, electrohydrodynamic-jet printed, high performance oxide transistors. *Journal of Materials Chemistry C* **2013,** *1*, 4236.

124. Leppaniemi, J.; Ojanpera, K.; Kololuoma, T.; Huttunen, O. H.; Dahl, J.; Tuominen, M.; Laukkanen, P.; Majumdar, H.; Alastalo, A., Rapid low-temperature processing of metal-oxide thin film transistors with combined far ultraviolet and thermal annealing. *Applied Physics Letters* **2014,** *105*, 113514.

125. Su, B. Y.; Chu, S. Y.; Juang, Y. D.; Chen, H. C., High-performance low-temperature solution-processed InGaZnO thin-film transistors via ultraviolet-ozone photo-annealing. *Applied Physics Letters* **2013,** *102*, 192101.

126. Wang, B.; Zeng, L.; Huang, W.; Melkonyan, F. S.; Sheets, W. C.; Chi, L.; Bedzyk, M. J.; Marks, T. J.; Facchetti, A., Carbohydrate-assisted combustion synthesis to realize high-performance oxide transistors. *Journal of the American Chemistry Society* **2016,** *138*, 7067-7074.

127. Kang, Y. H.; Jeong, S.; Ko, J. M.; Lee, J.-Y.; Choi, Y.; Lee, C.; Cho, S. Y., Two-component solution processing of oxide semiconductors for thin-film transistors via self-combustion reaction. *Journal of Materials Chemistry C* **2014,** *2*, 4247.

128. Xinge Yu, J. S., Nanjia Zhou, Li Zeng, Peijun Guo, Yu Xia, Ana Alvarez, Stefano Aghion, Hui Lin, Junsheng Yu, XingeYu, Robert P. H. Chang, Michael J. Bedzyk,Rafael Ferragut, Tobin J, Marks, Antonio Facchetti, Spray-combustion synthesis: Efficient solution route to high-performance oxide transistors. *Proceedings of the National Academy of Sciences* **2015,** *112* (11), 3217-3222.

129. Wang, B.; Yu, X.; Guo, P.; Huang, W.; Zeng, L.; Zhou, N.; Chi, L.; Bedzyk, M. J.; Chang, R. P. H.; Marks, T. J.; Facchetti, A., Solution-Processed All-Oxide Transparent High-Performance Transistors Fabricated by Spray-Combustion Synthesis. *Advanced Electronic Materials* **2016,** *2* (4), 1500427.

130. Moffitt, S.: Zhu, Q.; Ma, Q.; Buchholz, D. B.; Chang, R. P. H.; Mason, T. O.; Marks, T. J.; Bedzyk, M. J. In *Probing the role of Ga in amorphous conducting oxides through local structure studies*, APS March Meeting, San Antonio, Texas, U.S.A, San Antonio, Texas, U.S.A, 2015.

131. Chiang, H. Q.; Wager, J. F.; Hoffman, R. L.; Jeong, J.; Keszler, D. A., High mobility transparent thin-film transistors with amorphous zinc tin oxide channel layer. *Applied Physics Letters* **2005,** *86*, 22-24.

132. Yu, X.; Zhou, N.; Smith, J.; Lin, H.; Stallings, K.; Yu, J.; Marks, T. J.; Facchetti, A., Synergistic approach to high-performance oxide thin film transistors using a bilayer channel architecture. *ACS Applied Materials and Interfaces* **2013,** *5* (16), 7983-7988.

133. Gonçalves, G.; Barquinha, P.; Pereira, L.; Franco, N.; Alves, E.; Martins, R.; Fortunato, E., High Mobility a-IGO Films Produced at Room Temperature and Their Application in TFTs. *Electrochemical and Solid-State Letters* **2010,** *13* (1), H20.

134. Chiang, H. Q.; Hong, D.; Hung, C. M.; Presley, R. E.; Wager, J. F.; Park, C.-H.; Keszler, D. A.; Herman, G. S., Thin-film transistors with amorphous indium gallium oxide channel layers. *Journal of Vacuum Science & Technology B: Microelectronics and Nanometer Structures* **2006,** *24* (6), 2702.

135. Han, S. Y.; Chang, C. H.; Lee, D. H.; Herman, G. S., Inkjet-printed high mobility transparent-oxide semiconductors. *IEEE/OSA Journal of Display Technology* **2009,** *5*, 520-524.

136. Jeong, S.; Lee, J. Y.; Lee, S. S.; Choi, Y.; Ryu, B. H., Impact of metal salt precursor on low-temperature annealed solution-derived Ga-doped In2O3 semiconductor for thin-film transistors. *Journal of Physical Chemistry C* **2011,** *115*, 11773-11780.

137. Hwang, Y. H.; Bae, B.-S., Effect of Aluminum and Gallium Doping on the Performance of Solution-Processed Indium Oxide Thin-Film Transistors. *Journal of Display Technology* **2013,** *9*, 704-709.

138. Park, J. H.; Choi, W. J.; Chae, S. S.; Oh, J. Y.; Lee, S. J.; Song, K. M.; Baik, H. K., Structural and electrical properties of solution-processed gallium-doped indium oxide thin-film transistors. *Japanese Journal of Applied Physics* **2011,** *50*, 080202.

139. Park, J. H.; Yoo, Y. B.; Oh, J. Y.; Lee, J. H.; Lee, T. I.; Baik, H. K., Enhanced performance of solution-processed amorphous gallium-doped indium oxide thin-film transistors after hydrogen peroxide vapor treatment. *Applied Physics Express* **2014,** *7*, 051101.

140. Minami, T.; Takeda, Y.; Kakumu, T.; Takata, S.; Fukuda, I., Preparation of highly transparent and conducting Ga2O3–In2O3 films by direct current magnetron sputtering. *Journal of Vacuum Science & Technology A: Vacuum, Surfaces, and Films* **1997,** *15*, 958.

141. Lee, S.; Park, H.; Paine, D. C., A study of the specific contact resistance and channel resistivity of amorphous IZO thin film transistors with IZO source–drain metallization. *Journal of Applied Physics* **2011,** *109*, 063702.

142. Boya Cui, L. Z., Denis Keane, Michael J. Bedzyk, D. Bruce Buchholz, Robert P. H. Chang, Xinge Yu, Jeremy Smith, Tobin J. Marks, Yu Xia, AntonioF. Facchetti, Julia E. Medvedeva, M. Grayson, Thermal Conductivity Comparison of Indium Gallium Zinc Oxide Thin Films:

Dependence on Temperature, Crystallinity, and Porosity. *The Journal of Physical Chemistry C* **2016,** *120*, 7467-7475.

143. Huang, W.; Zeng, L.; Yu, X.; Guo, P.; Wang, B.; Ma, Q.; Chang, R. P. H.; Yu, J.; Bedzyk, M. J.; Marks, T. J.; Facchetti, A., Metal Oxide Transistors via Polyethylenimine Doping of the Channel Layer : Interplay of Doping , Microstructure , and Charge Transport. *Advanced Functional Materials* **2016,** *26*, 6179-6187.

144. Labram, J. G.; Treat, N. D.; Lin, Y. H.; Burgess, C. H.; McLachlan, M. A.; Anthopoulos, T. D., Energy Quantization in Solution-Processed Layers of Indium Oxide and Their Application in Resonant Tunneling Diodes. *Advanced Functional Materials* **2016,** *26*, 1656-1663.

145. Moghadam, M. M.; Voorhees, P. W., Thin film phase transformation kinetics: From theory to experiment. *Scripta Materialia* **2016,** *124*, 164-168.

146. de Jamblinne de Meux, A.; Pourtois, G.; Genoe, J.; Heremans, P., Comparison of the electronic structure of amorphous versus crystalline indium gallium zinc oxide semiconductor: structure, tail states and strain effects. *Journal of Physics D: Applied Physics* **2015,** *48* (43), 435104.

147. Je-Hyeong Bahk, H., Kazuaki Yazawa, Ali Shakouri, Flexible thermoelectric materials and device optimization for wearable energy harvesting. *Journal of Materials Chemistry C* **2016,** *3*, 10362.

148. Fujimoto, Y.; Uenuma, M.; Ishikawa, Y.; Uraoka, Y., Analysis of thermoelectric properties of amorphous InGaZnO thin film by controlling carrier concentration. *AIP Advances* **2015,** *5* (9), 097209.

149. Mildred S. Dresselhaus, G. C., Ming Y. Tang, Ronggui Yang. Hohyun Lee, Dezhi Wang, Zhifeng Ren, Jean-Pierre Fleurial, Pawan Gogna, New Directions for Low-Dimensional Thermoelectric Materials. *Advanced Materials* **2007,** *19*, 1043-1053.

150. G. Jeffrey Snyder, E. S. T., Complex thermoelectric materials. *Nature Materials* **2008,** *7*, 105-114.

151. Music, D.; Geyer, R. W.; Hans, M., High-throughput exploration of thermoelectric and mechanical properties of amorphous NbO2 with transition metal additions. *Journal of Applied Physics* **2016,** *120* (4), 045104.

152. Kanishka Biswas, J. H., Ivan D. Blum, Chun-I Wu, Timonthy P. Hogan, David N. Seidman, Vinayak P. Dravid, Mercouri G. Kanatzidis, High-performance bulk thermoelectrics with all-scale hierarchical architectures. *Nature* **2012,** *489*, 414-418.

153. L. Wang, M.-H. Yoon, G. Lu, Y. Yang, A. Facchetti, T. J. Marks, High-performance transparent inorganic-organic hybrid thin-film n-type transistors. *Nature Materials* **2006,** *5*, 893.

154. Thompson, A.; Attwood, D.; Gullikson, E.; Howells, M.; Kim, K.-J.; Janos; Kirz; Kortright, J.; Lindau, I.; Liu, Y.; Pianetta, P.; Robinson, A.; Scofield, J.; Underwood, J.; Williams, G.; Winick, H., *X-ray Data Booklet*. 3 ed.; Lawrence Berkeley National Laboratory, University of CA: Berkely, CA 94720, 2009.
155. Pfalzer, P.; Urbach, J.-P.; Klamm, M.; Horn, S.; denBoer, M. L.; Frenkel, A. I.; Kirkland, J. P., Elimination of self-absorption in fluorescence hard-x-ray absorption spectra. *Physical Review B* **1999,** *60* (13), 9335.
156. Gullikson, E. Center for X-ray Optics.